TECHNISCHE UNIVERSITÄT WIEN

ATOMINSTITUT

MASTER THESIS

The Giant Inverse Magnetocaloric Effect in Ni-Mn-Sn Alloys

to obtain the the degree

Master of Science (MSc)

as part of my studies

Technical Physics

submitted by

Klaus Frischauf

Mat.Nr.: 0527619

carried out at the Department of Low Temperature Physics
at the Atominstitut of the TU WIEN
Stadionallee 2, 1020 Vienna
in cooperation with Urals Branch of the Russian Academy of Sciences

Supervisor: Dr. Franz Sauerzopf

Vienna, 11.03.2019

signature student

Abstract

The giant inverse magnetocaloric effect was measured for four different NiMnSn alloys. Their content of elements was varied by only 1-2% respectively, but showed big changes to the phase transition temperatures and magnetic entropy change. It was expected that an increase in valence electrons per atom (e/a) and a decrease in the size of the unit cell (Vcell) would increase their phase transition temperatures respectively.

Increasing the amount of Ni by 1 % at cost of Mn, increased the transition temperatures but also slightly reduced the magnetic entropy change (ΔS_M) and refrigerant capacity (RC).

Introducing 2% of Si or Ge on cost of Sn reduced Vcell, as confirmed with XRD measurements. This is supposed to hold e/a constant, but is not yet confirmed experimentally.

Si and Ge doping strongly decreased the RC and significantly shifted the transition temperatures down and up, respectively.

This thesis contains information about their lattice constants, martensitic and austenitic phase transition temperatures, Curie temperatures, isothermal magnetization measurements, critical exponents, magnetic entropy change and resulting refrigerant capacities.

Contents

1 Introduction

The magnetocaloric effect (short: MCE) describes the temperature increase of a material by applying an external magnetic field, due to a change of it's magnetic entropy. While such an effect may be noticeable in all magnetic materials, it is usually small.

When talking about magnetocaloric materials, it refers to those that show a strong MCE, which is observed when the material undergoes a phase transition. Such materials are of particular interest for application in refrigerant cycles, where they could replace cooling liquids.

For that, a phase transition near the working temperature is needed. This transition should not only feature a large adiabatic temperature change, but should also happen over a temperature range as wide as possible. Here we study 4 ferromagnetic NiMnSn(X) based Heusler alloys on how doping affects their MCE. Their chemical formulas and masses are presented in table 1.1.

Table 1.1: The samples and their mass. Cubic shape with a side length of 3 mm.

Sample	Mass (mg)
$Ni_{43}Mn_{46}Sn_{11}$	125.4
$Ni_{44}Mn_{45}Sn_{11}$	111.7
$Ni_{43}Mn_{46}Sn_{9}Ge_{2}$	112.7
$Ni_{43}Mn_{46}Sn_{9}Si_{2}$	107.8

Those materials show a so called *giant inverse magnetocaloric effect* (GIMCE), where a phase transition between a tetragonal martensitic phase at low temperatures and a cubic austenitic phase at high temperatures happens (sec. 4.8).

The consequences are very big changes in magnetization. An important characteristic to describe this effect is the magnetic entropy change ΔS_{M} (chp. 4).

Table 1.2: The elements of the used alloys.

Element	Symbol	Atomic Number	Element Category
Nickel	Ni	28	transition metal
Manganese	Mn	25	transition metal
Tin	Sn	50	post-transition metal
Germanium	Ge	32	metalloid
Silicon	Si	14	metalloid

The term *inverse* corresponds to the sign of ΔS_M and means that it is positive during the phase transition and negative outside of it. In *normal* MCE materials, ΔS_{M} is always negative and just increases in magnitude during phase transition.

As a consequence, the giant inverse MCE leads to an adiabatic temperature decrease, while the *normal* one would lead to an increase.

Doping the samples affects their giant inverse MCE (GIMCE) in both magnitude, temperature width and start/end temperatures of the phase transition.

The samples where provided by Dr. Vyacheslav Viktorovich Marchenkov and are property of his research group.[1] They focus on unraveling what exactly influences the MCE, so that hopefully some day it becomes possible to design materials specifically for defined working temperatures.

2 Magnetic Refrigeration

The basic principle of magnet refrigeration is similar to conventional refrigeration with liquids.[2] In figure 2.1 this method is visualized. We start at (1) where the material sits without an external magnet field. The magnetic moments in the solid are randomly aligned and the resulting macroscopic magnetic moment is zero. We now apply an external magnetic field $|\vec{\mathbf{B}}| > 0$. This results in an interaction with the magnetic moments of the solid and they begin to align, as is illustrated in point (2). Adiabatic means we have no interaction with an external heat source and thus the total entropy remains constant, as long as the process is reversible. For a constant total entropy, the 1st law of thermodynamics simplifies, with external magnetic field B and magnetic moment M.

$$\mathrm{d}E = T \underbrace{\mathrm{d}S}_{0} + B\,\mathrm{d}M = B\,\mathrm{d}M \tag{2.1}$$

We now see that the internal energy only depends on the change of magnetic moment. This means, if the magnetic moments align, then magnetization increases and thus the internal energy E increases. While the total entropy stays constant, the magnetic entropy contribution obviously decreases with magnetization, since the disorder of the magnetic moments decreases. This all results in the sample in (2) heating up due to an adiabatic temperature increase, which is dependant on a change in the magnetic contribution of the entropy.

This energy can be transported off by some process, cooling the material down to the temperature of its surroundings. The magnetic field remains applied and thus the sample stays magnetized, as illustrated in (3).

In another adiabatic process, the magnetic field now is turned off. Thermal fluctuations in the material now will distort the orientation of the magnetic moments again, ultimately getting rid of the magnetization completely. This increase of magnetic entropy results in the sample cooling down, to a temperature lower than its surroundings. It can now act as a heat sink, absorbing enough heat energy until it is

at equilibrium with its surroundings again. We now have completed a whole cycle, and in theory this can be repeated as many time as desired. While in general all magnetic substances show such a behaviour, it is normally way to small for practical application.

In order to make use of this process, one requires a very big entropy change around the desired working temperature. We will later see that the adiabatic temperature change and magnetic entropy change in first approximation are only connected by the specific heat capacity at constant magnetic fields. This means also low heat capacities are needed, so that the material experiences a maximal adiabatic temperature change due to magnetization.

This search leads to Heusler alloys, which show the *giant inverse magnetocaloric effect*, which will be discussed in chapter 4.

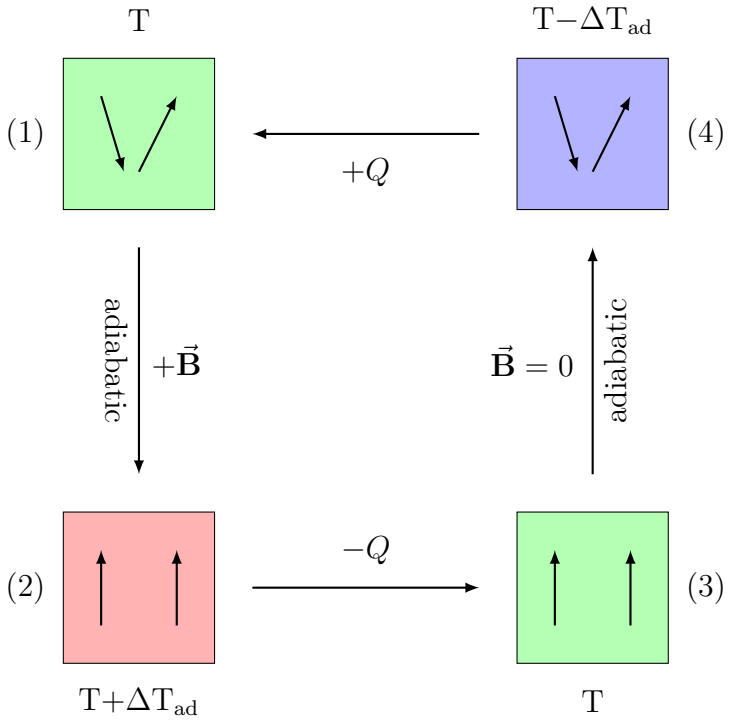

Figure 2.1: The basic magnetic refrigeration cycle for a *normal* MCE. Graphic inspired by Wikipedia article *Magnetic refrigeration.*[2]

3 Superconducting Quantum Interference Device

(a) Both SQUIDs. **(b)** Airlock.

Figure 3.1: A look at the SQUIDs.

The measurements were performed with 2 RF-SQUID machines, manufactured by Quantum Design. SQUID is short for **S**uperconducting **Qu**antum **I**nterference **D**evice, where *RF* stands for radio frequency. They consist of a superconducting loop that contains a single Josephson junction.

SQUIDs allow for very sensitive measurements, but need to be cooled with liquid ^{4}He, which is also used to set different surrounding temperatures in the sample chamber. The one on the left side in figure 3.1a is limited to fields of 1 T and a maximum temperature of 330 K. The right hand SQUID Quantum Design MPMS* reaches $B_{\max} = 7$ T and $T_{\max}$ of over 360 K.

The sample chamber is deep inside the He-bath surrounded by a vacuum. Thus the sample needs to pass through the airlock shown in figure 3.1b. Samples get attached to an individually prepared sample holder which is then attached to the bottom end of a metallic rod. The manual[3] explicitly shows the use of a simple

* **M**agnetic **P**roperty **M**easurement **S**ystem

straw as a holder, but it is not unusual to build one from hard aluminium foils which display a more reproducible background signal. A special tape, that can withstand very cold temperatures without loosing its adhesion, can be used to fixate the sample so that it doesn't fall out.

This chapter will provide a short overview about the basic principles of how a SQUID works, and how measurements are performed. For details, a look at the literature is recommended.[4]

3.1 A Superconducting Loop

We first look at how a superconducting loop responds to a an external magnetic field. The inner volume of a superconductor is field free and is shielded against external fields. However the hole inside the ring is a non superconducting area and magnetic flux lines can become "trapped" in it.

For our calculation we start with the 2nd Ginzburg-Landau Equation of superconducting, which gives a relation between the supra current density $\vec{\mathbf{j}}_s(\vec{\mathbf{r}})$, the vector potential $\vec{\mathbf{A}}(\vec{\mathbf{r}})$ of a magnetic field $\vec{\mathbf{B}}(\vec{\mathbf{r}})$ and the wave function of the cooper pairs $\Psi(\vec{\mathbf{r}})$.[5, p. 170]

$$\vec{\mathbf{j}}_s(\vec{\mathbf{r}}) = -\frac{ie\hbar}{m}\left(\Psi^*\vec{\nabla}\Psi - \Psi\vec{\nabla}\Psi^*\right) - \frac{4e^2}{m}|\Psi(\vec{\mathbf{r}})|^2\vec{\mathbf{A}}(\vec{\mathbf{r}}) \tag{3.1}$$

In semi classical approximation we assume that the wave function consists of a constant amplitude Ψ_0 and a local phase $\Phi(\vec{\mathbf{r}})$. This is also called the macroscopic wave function of the superconducting state.

$$\Psi \sim \Psi_0\, e^{i\Phi(\vec{\mathbf{r}})} = \sqrt{n_p}\, e^{i\Phi(\vec{\mathbf{r}})} \tag{3.2}$$

With this the first term on the right side of 3.1 can be simplified. The amplitude is not affected by the nabla operator and we obtain the gradient of the local phase and the cooper pair density $|\Psi_0|^2 = n_p$.

$$\Psi^*\vec{\nabla}\Psi - \Psi\vec{\nabla}\Psi^* = 2i|\Psi_0|^2\vec{\nabla}\Phi \tag{3.3}$$

We now rearrange equation 3.1 to obtain an expression for the gradient of the local phase.

$$\vec{\nabla}\Phi = \frac{1}{\hbar}\left[\frac{m}{2e|\Psi_0|^2}\vec{\mathbf{j}}(\vec{\mathbf{r}}) + 2e\vec{\mathbf{A}}(\vec{\mathbf{r}})\right] \tag{3.4}$$

Equation 3.4 can now be solved by integration over a selected path. For this, we choose a path deep inside the superconductor. The current of a superconductor flows on its surface and its inner volume is field free. So if we integrate over a closed circle inside of the conductor, we have no supra current, hence $\vec{\mathbf{j}}(\vec{\mathbf{r}}) = 0$. For the gradient of the phase we have another condition. This term describes the change of the local phase inside the material. The wave function has to "connect to itself" after a full run through the loop, to not interact destructive with itself. This means that the change in phase can only be an integer multiple of 2π.

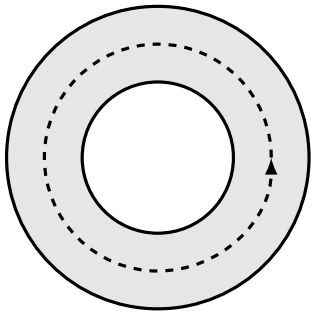

Figure 3.2: Choosing the integration path. They grey area is our superconductor, the dashed line represents the chosen path.

$$\oint \vec{\nabla}\Phi \cdot \mathrm{d}\vec{\mathbf{s}} = \oint \frac{2e}{\hbar}\vec{\mathbf{A}}(\vec{\mathbf{r}}) \cdot \mathrm{d}\vec{\mathbf{s}} = n \cdot 2\pi \tag{3.5}$$

The integral over the vector potential can be rewritten by using Stokes' theorem. This is especially helpful, because per definition the magnetic field $\vec{\mathbf{B}}$ is the curl of the vector potential.

$$\oint \vec{\mathbf{A}}(\vec{\mathbf{r}}) \cdot \mathrm{d}\vec{\mathbf{s}} = \int \vec{\nabla} \times \vec{\mathbf{A}}(\vec{\mathbf{r}}) \cdot \mathrm{d}\vec{\mathbf{F}} = \int \vec{\mathbf{B}} \cdot \mathrm{d}\vec{\mathbf{F}} \tag{3.6}$$

Equation 3.7 now has the form a flux integral, which describe the flow of a vector field through a chosen surface. For our integration path, we chose a closed circle inside of the superconducting loop. This means this equation gives the total magnetic field trapped inside the hole of the loop. By putting all together, we see that only a whole numbered multiple of the so called fluxon Φ_0 can exist inside of a superconducting loop.[5, p. 170]

$$\int \vec{\mathbf{B}} \cdot \mathrm{d}\vec{\mathbf{F}} = \Phi = n \underbrace{\frac{h}{2e}}_{\Phi_0} \approx n \cdot 2.07 \cdot 10^{-15}\ \mathrm{Wb} \tag{3.7}$$

If an external magnetic field is applied, a *shielding current* will start to flow inside the loop, shielding against the external field. If the field increases, this shielding current also increases. The superconducting state is stable as long as the critical current I_c of the superconductor is not exceeded. If the current exceeds I_c, then the superconductor returns to a normal conducting state.

By introducing a Josephson junction (sec. 3.2), it serves as a weak link in the conductor and lowers I_c. When the ring returns to normal conducting state, magnetic field lines can enter or leave the loop. Without a Josephson junction, the barrier between individual fluxon states would be too high to allow for transition.

This effect plays a major part for performing measurements with the Josephson Junctions.

3.2 Josephson junctions and RF SQUID

To construct an RF SQUID, this superconducting ring now is cut open at one spot. There, a non superconducting layer is introduced and the ring closed up again. This is a so called *Josephson contact*, which usually has a width of nano meters. Since the wavelength of the Cooper pairs is longer than this non superconducting layer, the pairs can tunnel through it due to quantum mechanical effects. This tunnel effect also leads to a phase difference for the wave functions, before and after the Josephson contact. It can be shown, that current which flows through the contact is directly dependant on this phase difference. This is the *1st Josephson equation* (eq. 3.8).[6]

$$I_s = I_c \sin(\phi) \tag{3.8}$$

Where ϕ is the gauge invariant phase, depending on the phases Φ_i before and after the contact. The integration borders denote the path between superconducting areas 1 and 2, which are separated by the Josephson junction. Φ_0 is the fluxon from equation 3.7.[6]

$$\phi = \Phi_1 - \Phi_2 - \frac{2\pi}{\Phi_0} \int_1^2 \vec{\mathbf{A}} \cdot \mathrm{d}\vec{\mathbf{s}} \tag{3.9}$$

After some calculation, one can obtain a relation between the gauge invariant phase and the electric field in the junction. Equation 3.10 is called the *2nd Josephson equation.*[6][7]

$$\frac{\partial \phi}{\partial t} = \frac{2\pi}{\Phi_0} \int_1^2 \vec{\mathbf{E}} \cdot \mathrm{d}\vec{\mathbf{s}} \tag{3.10}$$

We see that the integral on the right side is just the definition of the voltage. If we apply a constant voltage V_0, we get the following phase.

$$\phi(t) = \phi(0) + \frac{2\pi}{\Phi_0} V_0 t \tag{3.11}$$

Inserting this into equation 3.8, it shows that the resulting current in the junction is an alternating current.

$$i(t) = I_c \sin\left(\phi(0) + \frac{2e}{\hbar} V_0 t\right) = I_c \sin\left(\phi(0) + \frac{2\pi}{\Phi_0} V_0 t\right) \tag{3.12}$$

Further more, if we apply an AC with $v(t) = V_0 + V_s \cos(\omega t)$, this expression gets an addition term in the sinus.

$$i(t) = I_c \sin\left(\phi(0) + \frac{2\pi}{\Phi_0} V_0 t + \frac{2\pi V_s}{\Phi_0 \omega} \sin(\omega t)\right) \tag{3.13}$$

The SQUID uses a flux locked loop, where the flux through the SQUID is held constant. A resonance tank is coupled to the SQUID through "rf-coils". When the flux from the input coils changes, this results in an output of a phase sensitive detector. A feedback current runs through the rf-coils and compensates the flux change, keeping the total flux through the SQUID constant.[8]

3.3 Measuring the magnetic moment

The SQUID control software operates with cgs-units. We can either perform the calculation in cgs units and convert afterwards, or convert first and use SI all the way. Table 3.1 provides a list of how to convert between those units.

When applying a magnetic field, the software asks for a value specified in Oersted. Here it is important to understand the mechanism before converting. In cgs-units the correlation between $\vec{\mathbf{B}}$ and $\vec{\mathbf{H}}$ simplifies by setting $\mu_0 = 1$.

$$\vec{\mathbf{B}}(\mathrm{G}) = \mu_r \, \vec{\mathbf{H}}(\mathrm{Oe}) \tag{3.14}$$

Table 3.1: converting CGS to SI units.

Quantity	Symbol	**CGS**	**SI**
Magnetic field	$\vec{\mathbf{B}}$	1 G	10^{-4} T
Magnetic field strength	$\vec{\mathbf{H}}$	1 Oe	10^{-4} A/m
Magnetic moment	$\vec{\mathbf{m}}$	1 emu	10^{-3} Am^2
Energy	E	1 erg	10^{-7} J
Entropy	S	1 erg/K	10^{-7} J/K

In Vacuum μ_r becomes 1 and therefore $\vec{\mathbf{B}}$ and $\vec{\mathbf{H}}$ are of the same numerical value. By charging the magnet to create a field of a certain magnitude in Oersted, we apply an *external* magnetic field $\vec{\mathbf{B}}$ of the unit Gauss in the sample chamber. This field now can be converted easily to SI units by using table 3.1. For example, a field of 10 000 Oe equals 1 T in the sample chamber.

To measure the longitudinal magnet moment of the sample, the SQUID uses a gradiometer of second order. It consists of 3 consecutive pickup coils. The 2 outer coils consist of a single loop, while the middle one has 2 loops and is orientated in the opposite direction. The sample is moved up and down in these pickup coils.

During this process it produces a voltage as show in figure 3.3. The different orientation of the loops results in the change of sign from the voltage and provides a sharper contrast than a coil with just a single loop. A coil with two loops would be called a gradiometer of first order. The measurement then gives us the magnetic moment of the sample in emu, which can be converted to Am^2 by multiplying with 10^{-3}. Gradiometers are used to strongly reduce environmental noise.

The external magnetic field $\vec{\mathbf{B}}$ produced by a magnetic dipole moment is given by equation 3.15.

$$\vec{\mathbf{B}}(\vec{\mathbf{r}}, \vec{\mathbf{m}}) = \frac{\mu_0}{4\pi}\left[\frac{3\vec{\mathbf{r}}(\vec{\mathbf{r}} \cdot \vec{\mathbf{m}})}{r^5} - \frac{\vec{\mathbf{m}}}{r^3}\right] \tag{3.15}$$

Here, $\vec{\mathbf{m}} = m\,\hat{\mathbf{z}}$ is the longitudinal magnetic moment along the z-axis. Only the z-component of $\vec{\mathbf{B}}$ couples into the pickup coils.[9] This can be easily understood because in an ideal setup, the surface vector of the loops is parallel to the moving direction of the sample. Then no horizontal components of the magnetic field would change its flux through the coils.

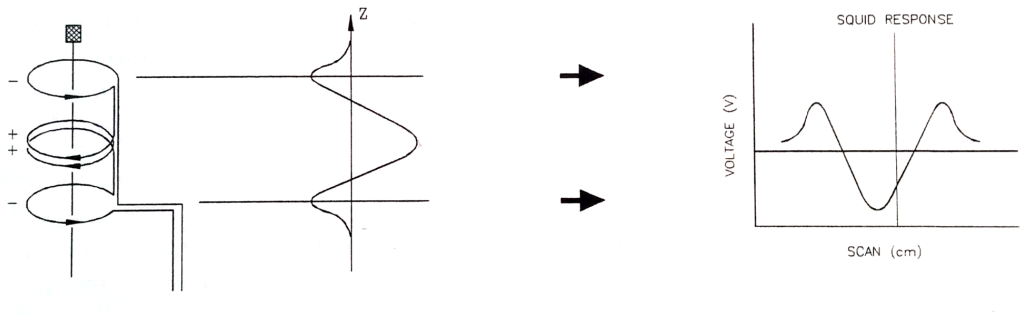

Figure 3.3: Gradiometer of 2nd order and response voltage. Illustration taken from the SQUID manual.[3]

$$B_z = \frac{\mu_0}{4\pi}\left[\frac{3z^2 m}{(x^2+y^2+z^2)^{5/2}} - \frac{m}{(x^2+y^2+z^2)^{3/2}}\right] \tag{3.16}$$

The magnetic flux through a single pickup coil "X" is given by equation 3.17.

$$\Phi_{\mathrm{X}} = \int B_z \,\mathrm{d}A \tag{3.17}$$

For a Gradiometer of 2nd order, the total flux Φ is the sum of fluxes through all loops.

$$\Phi_{\mathrm{total}} = \Phi_1 - 2\Phi_2 + \Phi_3 \tag{3.18}$$

The minus sign for the double loop in the middle comes from its different orientation of this coil. We now have a correlation between the magnetic moment and the voltage of the gradiometer.

$$U \propto \Phi_{\mathrm{total}} \propto B_z \propto m \tag{3.19}$$

Comparing equations 3.16 and 3.18 shows that the magnetic flux depends linear on the magnetic moment.

The detection coil is a single piece of superconducting wire, formed to a gradiometer of 2nd order (fig. 3.3).[10] As the sample moves up and down in the sample chamber, the flux through the gradiometer coils changes, which is proportional to the magnetic moment.

It is adjustable how many times the SQUID moves the sample through the pickup coils for one measurement. In our experiments three measurements each with 48

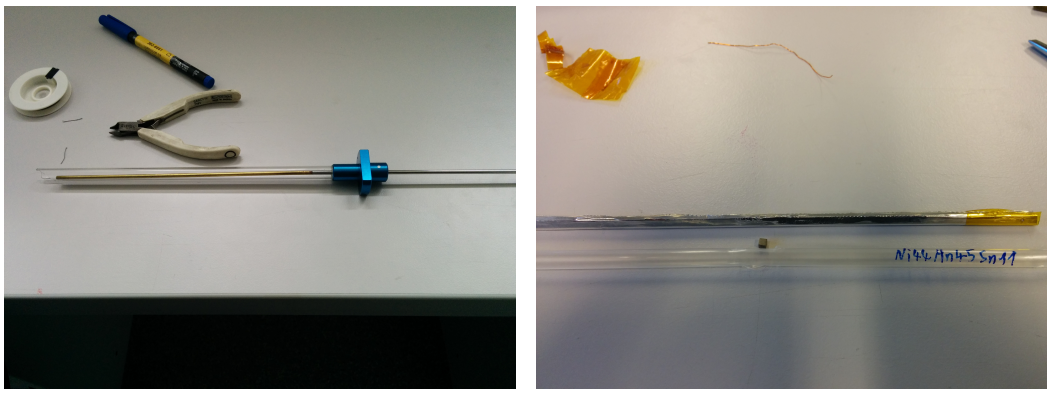

(a) Bottom end of the rod. **(b)** A sample and its holders.

Figure 3.4: Utensils to measure the sample.

points were performed.

This could be set to higher values, but the signal of the analysed Heusler alloys is big enough to obtain good results with those settings. When performing multiple measurements, i.e. repeating the movement through the pickup coils, the SQUID software calculates a mean value and the standard deviation.

In order for the software to properly calculate the magnetic moment from the measured voltage, the sample needs to be centered in the middle of the pickup coils before starting the measurement. This sets the 0 point for the z-axis, from where the dipol signal is being expected. Since the pickup signal has a clear form, one could actually correct it for small deviations. Only if the sample becomes too off-centered a significant part of the signal can get cut off. It is not advisable to test how much margin of error the software allows here.

Figure 3.4b shows two different sample holders. The one below is a simple straw as used in the SQUID manual. Its advantage is that the sample can be quickly attached inside of them, are sturdy enough to not deform easily and can just be disposed afterwards without causing additional work.

Above is a self prepared sample holder made of aluminium. The used aluminium foil is thick enough to hold itself into form, but can still easily get deformed by careless handling. Cutting and folding these sample holders takes a bit of more time and effort than just using a new straw. They usually are necessary if you want to make measurements of weak signals and to be sure that there are as few disturbing effects as possible.

For the Heusler alloys, the choice of sample holder didn't make any difference, because their signal was very strong. Between the sample holders is one of our

samples, showing the same cubic form that all 4 others also have.

After the sample is inside one of those holders, it gets attached to the lower end of the rod from figure 3.4a. The glass cylinder is needed for the airlock in figure 3.1b to slide the sample in. After purging the airlock, the glass remains in the airlock while the sample is lowered into the chamber.

4 The Magnetocaloric Effect

The nature of the MCE comes from the different contributions to the total entropy in a solid. It consists of the magnetic order, as well as electronic and lattice contributions. If a magnetic field is applied adiabatically, the magnetic entropy will decrease as the magnetic order increases.

In an adiabatic process, the total entropy remains constant. So the loss of magnetic entropy is compensated by an increase of lattice entropy. This results in the solid heating up. When the field is turned off adiabatically, then thermal fluctuations will lead to a decrease in magnetic order. The increase in magnetic entropy then is compensated by a decrease of lattice entropy. This means the energy provided for magnetic disordering is provided by the lattice and results in an adiabatic temperature decrease. Thus the nature of the MCE is a reversible process of entropy transfer between the magnetic subsystem and the lattice.

Conventional magnetocaloric materials show a $\Delta S_{\mathrm{M}} < 0$ and $\Delta T_{\mathrm{ad}} > 0$ when a magnetic field is applied, while inverse materials show $\Delta S_{\mathrm{M}} > 0$ and $\Delta T_{\mathrm{ad}} < 0$.[11, Box 1] For inverse materials, the magnetization increases at higher temperatures, while the magnetization decreases for conventional materials.

Our Heusler alloys undergo a first order phase transition between a tightly packed martensitic phase at low temperatures and a cubic austenitic phase at high temperatures (section 4.8, lattice space groups in table 4.5). This is accompanied by big changes in magnetization between both phases. The consequences are big changes of ΔS_{M} and ΔT_{ad}. Because of this, it is also called the *giant* effect. All 4 samples in this thesis show both, *inverse* and *giant* behaviour, over their phase transition. When both behaviours occur simultaneously, it is called the *giant inverse magnetocaloric effect*.

In this chapter we will derive basic thermodynamic equations to describe the magnetocaloric effect. They provide a rough description of it and are enough for our usage. The contents of sections 4.4, 4.5 and 4.6 are based on the cited sources.[1][12–15][16, chp. 1]

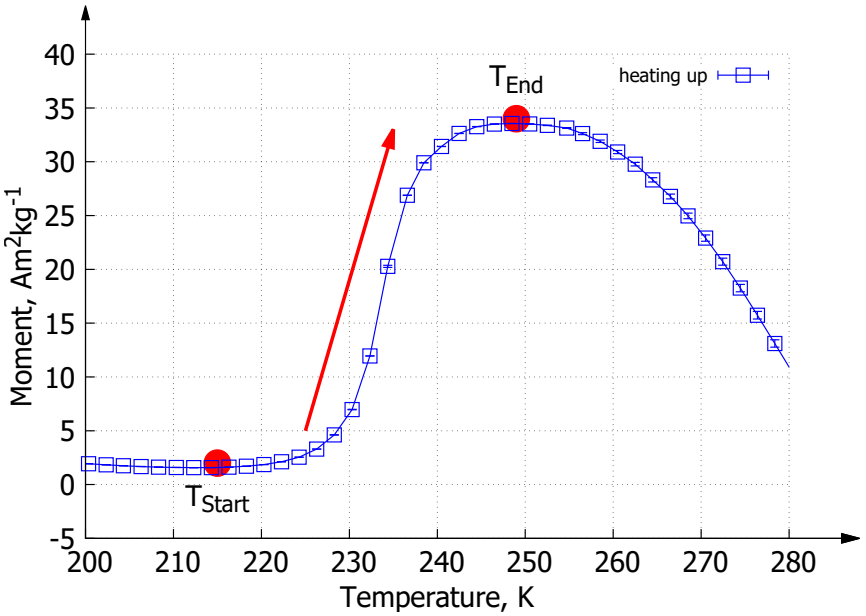

Figure 4.1: Example of how to find T_{Start} and T_{End} of the austenitic phase transition. $Ni_{44}Mn_{45}Sn_{11}$ in a field of 0.1 T.

4.1 Phase Transition

The measured Heusler alloys undergo a first order phase transition between a closely packed tetragonal martensitic phase at low temperatures and a cubic austenitic phase at high temperatures. Figure 4.1 demonstrates how to identify the start and end temperatures of the transition from the martensitic to the austenitic phase.

Those are called the austenitic start and end temperatures. The martensitic start and end temperatures are just the inverse process of this, but they are not identical. They are obtained with field cooling measurements where the start temperature is higher than the end temperature.

As seen in figure 4.1 it's not always easy to tell where exactly the transitions start and end, because it could be somewhere between two measured points. This phase transition then results in a big change of magnetization.

Those temperatures are dependant on the external magnetic field and the "direction" of the phase transition. T_{Start} and T_{End} are different for martensitic $\rightarrow$ austenitic and austenitic $\rightarrow$ martensitic. The martensitic transition temperatures are usually lower than the austenitic ones. So while cooling down the phase transition happens at slightly lower temperatures.

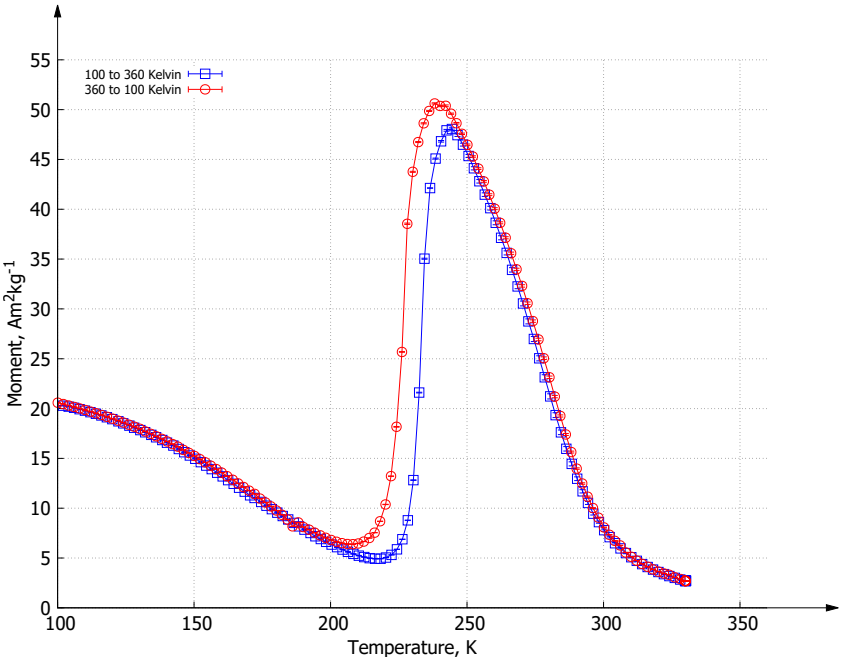

Figure 4.2: Thermal hysteresis shown for $Ni_{44}Mn_{45}Sn_{11}$ in a field of 0.5 T. The magnetization during the phase transition is clearly shifted. This gives the different start end end temperatures for the martensitic and austenitic transitions.

To find the transition temperatures we need to run temperature cycles. $T_{\text{Start/End}}$ also are affected by the strength of the external magnetic field. Because of that we need to run these cycles for multiple different constant fields.[1]

4.2 1st Law of Thermodynamics

The first law of thermodynamics is the principle of conservation of energy.

$$\mathrm{d}E = \delta W + \delta Q \tag{4.1}$$

Here, $\mathrm{d}E$ stands for the change in internal energy, δW the work performed and δQ is the change in heat. $\mathrm{d}E$ denotes an exact differential*, while δQ and δW are generally inexact ones. For reversible processes, we can write δQ and δW as the following 2 expressions.

* $\oint \mathrm{d}E = 0$ for every path.

$$\mathrm{d}W = \sum_i X_i \,\mathrm{d}\zeta_i \qquad (4.2) \qquad\qquad \delta Q_{\mathrm{rev}} = T\,\mathrm{d}S \qquad (4.3)$$

As seen in equation 4.2, $\mathrm{d}W$ can now be written as an exact differential. Here X_i denotes intensive variables, that don't change with the size of the system, while $\mathrm{d}\zeta_i$ stands for a change of extensive variables, which depend on the size of the system. The change of heat δQ_{rev} can be rewritten as a differential for the entropy $\mathrm{d}S$.

Under influence of an external magnetic field $\vec{\mathbf{B}}$, and when changes in volume and pressure are negligible, the first law of thermodynamics now takes the form of equation 4.4.†[17]

$$\mathrm{d}E = T\,\mathrm{d}S + B\,\mathrm{d}m \qquad (4.4)$$

Here $\vec{\mathbf{m}}$ denotes the magnetic moment of the system. Since $\vec{\mathbf{B}}$ and $\vec{\mathbf{m}}$ are usually parallel, their vector characteristics can be ignored.‡ In literature it is very common to find the magnetic field and magnetic moment as $\vec{\mathbf{H}}$ and $\vec{\mathbf{M}}$, where $\vec{\mathbf{M}}$ is called magnetization. This is due to different unit systems i.e. CGS, where $\vec{\mathbf{B}}$ and $\vec{\mathbf{H}}$ are the same in vacuum and only differ in a solid. Also magnetization and magnetic moment are connected by a volume integral.

$$\vec{\mathbf{m}} = \iiint \vec{\mathbf{M}}\,\mathrm{d}V \qquad (4.5)$$

In this thesis we will often talk about magnetization and magnetic moment as if they where the same. The reason is that we are actually measuring the magnetic moment, but analyse it divided by the mass of the sample. The magnetic moment then can also be interpreted as the moment of a unit volume, where $\vec{\mathbf{M}}$ and $\vec{\mathbf{m}}$ then are basically the same and normalized to kg. It is also simple to convince yourself that for SI units $\vec{\mathbf{B}}$ and $\vec{\mathbf{m}}$ are the correct choices. $\vec{\mathbf{B}} \cdot \vec{\mathbf{m}}$ has to be in the dimension of an energy, here J. In SI the magnetic moment has units Am^2 and the magnetic field T. T can also be written as $\mathrm{J/Am}^2$. So the product of the $\vec{\mathbf{B}}$ and $\vec{\mathbf{m}}$ will be of units J, which is the required dimension of energy. In section 4.3, we will norm the extensive variables to mass m_0 and handle them like "densities". The magnetic moment will then be written as M with units $\mathrm{Am}^2\mathrm{kg}^{-1}$.

† Sometimes $\mathrm{d}E = T\,\mathrm{d}S - m\,\mathrm{d}B$ is used instead.[17]

‡ $\vec{\mathbf{B}} \cdot \vec{\mathbf{m}} = Bm\cos(\theta)\big|_{\theta=0} = Bm$

4.3 Thermodynamic Potentials

The internal energy E from equation 4.4 is one of the so called thermodynamic potentials. It describes how energy can be exchanged in isolated systems, depending on its natural variables S and M. There are several different types of thermodynamic systems, which then also depend on different natural variables. By performing Legendre transformations, we can obtain different thermodynamic potentials, to describe a different type of system.

The state of a thermodynamic system is completely determined by the natural variables of it's corresponding potential. A system is in thermodynamic equilibrium, if its thermodynamic potential shows a minimum or maximum. To describe the magnetocaloric effect, we need the internal energy E, the free energy F, the enthalpy H and the Gibbs potential G. The correlations between those thermodynamic potentials, and their natural variables, are shown in table 4.1.[17]

Table 4.1: The thermodynamic potentials.

$E(S, M) = TS + BM$
$F(T, M) = E - TS$
$H(S, B) = E - BM$
$G(T, B) = H - TS$

There also exist several thermodynamic "response functions". They describe how the system reacts to an external stimulus. One of them is the specific heat capacity under a certain condition. The general definition, where a variable X is held constant, is given by equation 4.6.

$$C_X = \left(\frac{\delta Q}{\partial T}\right)_X \tag{4.6}$$

For MCE materials, the heat capacity at constant magnetic fields for a reversible process, is of particular interest. For constant magnetic fields, it can be expressed with the enthalpy, as shown in equation 4.7.

$$C_B = \left(\frac{\partial H}{\partial T}\right)_B = T\left(\frac{\partial S}{\partial T}\right)_B = -T\left(\frac{\partial^2 G}{\partial T^2}\right)_B \tag{4.7}$$

In the last step we used $(\partial G/\partial T)_B = -S$, which will be derived in section 4.4, or can be read from a Guggenheim square (fig. 4.3).

Per definition, the entropy S is an extensive variable (J/K) and depends on the size of the system. For a comparison between multiple samples, we are looking at an intensive entropy instead.

$$S \to \frac{S}{m_0} \tag{4.8}$$

This is simply the entropy divided by the mass m_0 of the sample. In SI units S now becomes $\mathrm{JK^{-1}kg^{-1}}$. We will do the same for the magnetic moment m, resulting in M with $\mathrm{Am^2kg^{-1}}$. Those no longer depend on the size of the system and allow for comparison between samples of different mass.

As a consequence, the potentials E, F, H and G also change units from J to J/kg, while the intensive properties, T and B, remain unchanged.

Since the extensive properties appear only linear in the definitions of the thermodynamic potentials (tab. 4.1), we can use either form. We can derive our formulas for basic SI units, and perform calculation with "densities" (normalized to mass).

Performing operations within the Guggenheim square (fig. 4.3), proofs that table 4.2 are the correct SI units to use, if we norm by mass.

Table 4.2: SI units for the Guggenheim square.

property	S	B	T	M	E	F	H	G
units	J/(K kg)	T, $\mathrm{J/Am^2}$	K	$\mathrm{Am^2/kg}$	J/kg			

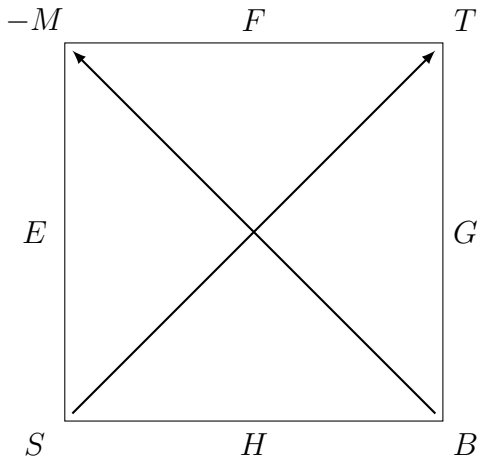

Figure 4.3: The Guggenheim square with a magnetic field. Magnetic moment M and magnetic field B are replacing pressure and volume.

4.4 Magnetic Entropy change

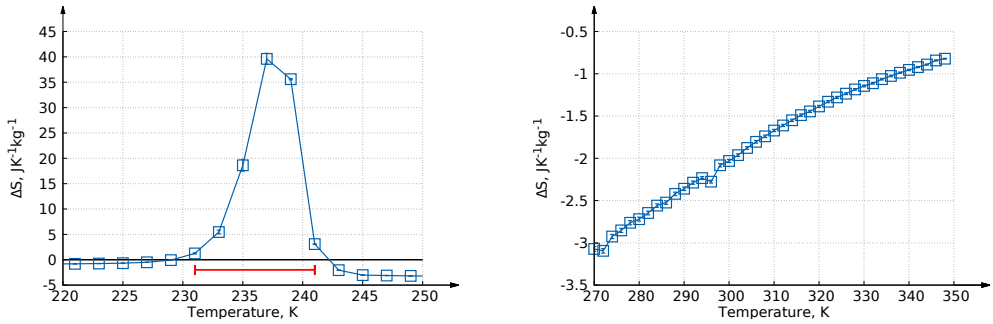

(a) At the phase transition. **(b)** At room temperatures.

Figure 4.4: The magnetic entropy change in $Ni_{43}Mn_{46}Sn_9Ge_2$. 4.4a shows the giant inverse magnetocaloric effect.

The entropy of a solid can be defined as the sum of 3 contributions.[16, chp. 1]

$$S(B,T) = S_{\mathrm{M}}(B,T) + S_{\mathrm{lattice}}(T) + S_{\mathrm{el}}(T) \tag{4.9}$$

Here $S_{\mathrm{M}}(B,T)$ and $S_{\mathrm{el}}(T)$ denote the magnetic and electric contributions, while $S_{\mathrm{lattice}}(T)$ comes from the atomic lattice. Since only S_{M} depends on an external magnetic field, we can directly calculate its change between 2 different field strengths.[16]

$$\Delta S_{\mathrm{M}}(T_0, \Delta B) = S(T_0, B_1) - S(T_0, B_0) \tag{4.10}$$

Equation 4.10 means that ΔS_M is negative if an increasing field leads to increased order of the magnetic moments.

By using the definition of the specific heat from equation 4.6, it is possible to derive equation 4.11 for the magnetic entropy change ΔS_{M}.

$$\Delta S_{\mathrm{M}}(T, \Delta B) = \int_0^T \frac{C(B,T') - C(0,T')}{T'}\,\mathrm{d}T' \tag{4.11}$$

In order to only evaluate the magnetic component, we need the difference of the specific heat with and without a magnetic field.[16]

A different method, without measurements of C, can be derived from the Gibbs free energy. It gives us a correlation between entropy and magnetic moment, when we compare the coefficients of its total differential with its Legendre transformation.

$$\mathrm{d}G = \mathrm{d}H - S\,\mathrm{d}T - T\,\mathrm{d}S = -S\,\mathrm{d}T - M\,\mathrm{d}B \tag{4.12}$$

$$\mathrm{d}G = \underbrace{\left(\frac{\partial G}{\partial T}\right)_B}_{-S} \mathrm{d}T + \underbrace{\left(\frac{\partial G}{\partial B}\right)_T}_{-M} \mathrm{d}B \tag{4.13}$$

We now have identified expressions for the entropy and magnetic moment as derivatives of the Gibbs energy. Next we individually perform partial derivatives of S and M. By allowing the partial derivatives to commute, it is possible to obtain a direct relation between different differential quotients. There are many of such expressions and they are called Maxwell relations. An easy way to obtain those relations is to simply read them from the so called Guggenheim scheme, also called Born square. We will spare us this part, but want to show where this particular Maxwell relation comes from in the first place.

$$-\left(\frac{\partial S}{\partial B}\right)_T = \frac{\partial}{\partial B}\left(\frac{\partial G}{\partial T}\right)_B = \frac{\partial}{\partial T}\left(\frac{\partial G}{\partial B}\right)_T = -\left(\frac{\partial M}{\partial T}\right)_B \tag{4.14}$$

The Maxwell relation from equation 4.15 now provides a link between Entropy S, an external magnet field B, temperature T and the magnetic moment M.

$$\left(\frac{\partial S}{\partial B}\right)_T = \left(\frac{\partial M}{\partial T}\right)_B \tag{4.15}$$

After performing integration, we obtain an equation that allows us to calculate the entropy difference $\Delta S_\mathrm{M} \coloneqq S(B,T) - S(0,T)$ by solely using parameters that we can measure.

Strictly speaking this relation could not be used for first order transition, because $(\partial G/\partial T)_B = -S$ would not be continuous. It has however been suggested that it can be used to calculate ΔS_M, because the transition is not truly discontinuous.[18][19]

$$\Delta S_\mathrm{M}(T, \Delta B) = \int_0^{B_\mathrm{max}} \left(\frac{\partial M}{\partial T}\right)_B \mathrm{d}B \tag{4.16}$$

The partial differential can be approximated by using numerical differentiation.

$$\frac{\partial M}{\partial T} \approx \frac{M(T+\Delta T) - M(T)}{\Delta T} + \mathcal{O}\left(\Delta T^2\right) \tag{4.17}$$

With that, we obtain an equation that is suited for numerical integration. If we restrict to a constant ΔT, we can further simplify.

$$\Delta S_{\mathrm{M}}(T, \Delta B) \approx \frac{1}{\Delta T}\left[\int_0^{B_{\max}} M(T+\Delta T, B)\,\mathrm{d}B - \int_0^{B_{\max}} M(T, B)\,\mathrm{d}B\right] \tag{4.18}$$

In words, $\Delta S_{\mathrm{M}}(T, \Delta B)$ describes the change of magnetic entropy at a specific temperature T when an external field B is increased.

Equation 4.18 now also gives us a blueprint for our measurement procedure. We measure the magnetic moment at a fixed temperature in an increasing magnetic field, up to a maximum field of $B_{\max}$. For that we ramp the field up in multiple steps and measure at each point, until we reach the chosen $B_{\max}$. It is important to add more points at low fields, since the change of magnetization is bigger in this region. For higher fields the changes (normally) become smaller as the sample reaches saturation. If we have done enough data points, the integral can be evaluated by applying the trapezoid rule from equation 4.20 between the different field steps.

$$\int_a^b f(x)\,\mathrm{d}x \approx \frac{f(a)+f(b)}{2}(b-a) \tag{4.19}$$

$$\sum_i \int_{B_i}^{B_{i+1}} M(T, B)\,\mathrm{d}B \approx \sum_i \frac{M(T, B_i) + M(T, B_{i+1})}{2}(B_{i+1} - B_i) \tag{4.20}$$

The sum of those trapezoid integrals then gives us the complete integral at a fixed temperature, which is needed for equation 4.18. So basically the calculation of ΔS simplifies to evaluating the difference of the areas under two magnetization curves. If the steps of the magnetic field are identical across the measurements from diferent temperatures, ΔS can be written as equation 4.21. For simplicity, we use the notation $M(T+\Delta T, B_i) = M_i$ and $M(T, B_i) = m_i$.

$$\Delta S_{\mathrm{M}}(T) = \frac{1}{2\Delta T}\sum_i (B_{i+1} + B_i)[(M_{i+1} + M_i) - (m_{i+1} + m_i)] \tag{4.21}$$

Since all the magnetic moments only appear in linear form, propagation of uncertainty can be easily applied to get equation 4.23 for the error of ΔS_{M}.

$$\sigma^2_{\Delta S_{\mathrm{M}}} = \sum_i \left(\frac{\partial \Delta S_{\mathrm{M}}}{\partial M_i}\right)^2 \sigma^2_{M_i} \tag{4.22}$$

Inserting our approximation for the entropy change results in our full expression of the propagated error.

$$\sigma^2_{\Delta S_\mathrm{M}}(T) = \left(\frac{1}{2\Delta T}\right)^2 \sum_i (B_{i+1} + B_i)^2 \left[\left(\sigma^2_{M_{i+1}} + \sigma^2_{M_i}\right) - \left(\sigma^2_{m_{i+1}} + \sigma_{m_i}\right)^2\right] \tag{4.23}$$

Given the strong signal and precise measurement of SQUIDs, the standard deviation usually gets ignored in publications. The results in chapter 7 will show that this is justified.

4.5 Adiabatic Temperature change

To find an expression for the adiabatic temperature change ΔT_ad, we look at the enthalpy H.

$$\mathrm{d}H = \mathrm{d}E - M\,\mathrm{d}B - B\,\mathrm{d}M = T\,\mathrm{d}S - M\,\mathrm{d}B \tag{4.24}$$

Comparing coefficients leads to expressions for T and M as partial derivatives of the enthalpy.

$$\mathrm{d}H = \underbrace{\left(\frac{\partial H}{\partial S}\right)_B}_{T} \mathrm{d}S + \underbrace{\left(\frac{\partial H}{\partial B}\right)_S}_{-M} \mathrm{d}B \tag{4.25}$$

By requiring that the partial derivatives permute, we obtain the Maxwell relation from equation 4.26. This gives a connection between temperature, magnetic field, magnetic moment and entropy.

$$\left(\frac{\partial T}{\partial B}\right)_S = \left(\frac{\partial}{\partial B}\left(\frac{\partial H}{\partial S}\right)_B\right)_S = \left(\frac{\partial}{\partial S}\left(\frac{\partial H}{\partial B}\right)_S\right)_B = -\left(\frac{\partial M}{\partial S}\right)_B \tag{4.26}$$

From said Maxwell relation, it is now possible to calculate an expression for the adiabatic temperature change ΔT_ad.

$$\Delta T_\mathrm{ad} = -\int_0^{B_\mathrm{max}} \left(\frac{\partial M}{\partial S}\right)_B \mathrm{d}B \tag{4.27}$$

We want to simplify this expression. This is possible by using the specific heat at constant magnetic fields, so we can rewrite the partial derivative. For that we first look at the definition of the enthalpy when applying a constant magnetic field. In equation 4.28 we see that the 2nd term becomes zero and the total differential of

the enthalpy only consist of $T\,\mathrm{d}S$.

$$\mathrm{d}H = T\,\mathrm{d}S - M\underbrace{\mathrm{d}B}_{=0} = T\,\mathrm{d}S \tag{4.28}$$

This can be used to write the specific heat at constant magnetic field in a simple form.

$$C_B(T) = \left(\frac{\delta Q}{\partial T}\right)_B = \left(\frac{\partial H}{\partial T}\right)_B = T\left(\frac{\partial S}{\partial T}\right)_B \tag{4.29}$$

We again require that partial derivatives permute and manipulate the quotient of expression 4.27. Expanding by T und ∂S lets us obtain a form that now directly includes the specific heat capacity. Also the partial derivative now describes a change of magnetic moment by temperature in a constant field. This information can be easily obtained from experiments.

$$\frac{\partial M}{\partial S} = \frac{T}{\frac{T\partial S}{\partial T}}\frac{\partial M}{\partial T} = \frac{T}{C_B}\left(\frac{\partial M}{\partial T}\right)_B \tag{4.30}$$

By inserting this into equation 4.27 we obtain expression 4.31.

$$\Delta T_{\mathrm{ad}}(T, \Delta B) = -\int_0^{B_{\max}} \left(\frac{T}{C_B(T,B)}\right)_B \left(\frac{\partial M}{\partial T}\right)_B \mathrm{d}B \tag{4.31}$$

If we now compare equations 4.16 and 4.31, we notice that they both depend on $(\partial M/\partial T)_B$. So we have obtained a direct correlation between ΔS_{M} and ΔT_{ad}, although information about $C_B(T, B)$ is still needed to get the actual adiabatic temperature change.

Unfortunately we have no data about the specific heat of the analysed materials. However a publication about $Ni_{43}Mn_{46}Sn_{11}$ has shown that its heat capacity is always positive and increases sharply during the phase transition.[15]

We will focus on the magnetic entropy change and the resulting refrigerant capacity, which will be introduced in section 4.6. Even though we can not evaluate the adiabatic temperature change, we have derived that it is closely related to the magnetic entropy change. This establishes ΔS_{M} as an important parameter for the magnetocaloric effect, with a direct mathematical formulation. We also now have derived equations to describe the magnetic refrigeration cycle from chapter 2.

4.6 Refrigerant Capacity

There are at least 2 different definitions of the refrigerant capacity (RC). The one used in this thesis is shown in the equation 4.32.[16, chp. 1]

It defines how much energy can be transferred between the cold and hot sinks in an ideal refrigerant cycle.[16, chp. 1] It is the integral of ΔS_{M} over temperature. RC still depends on the applied magnetic fields and has the dimension of an energy.

Here everything that was measured was directly converted into SI units and normalized by mass, so the refrigerant capacity is calculated in J/kg.

$$\mathrm{RC}(\Delta B) = \int_{T_{\mathrm{cold}}}^{T_{\mathrm{hot}}} \Delta S_{\mathrm{M}}(T, \Delta B)\,\mathrm{d}T \ \ [\mathrm{J/kg}] \tag{4.32}$$

$$\mathrm{RC}(\Delta B) \approx \sum_i \frac{\Delta T_i}{2}[\Delta S_{\mathrm{M}}(T_i + \Delta T_i) + \Delta S_{\mathrm{M}}(T_i)] \tag{4.33}$$

$$\sigma^2_{\mathrm{RC}} \approx \sum_i \left(\frac{\Delta T_i}{2}\right)^2 \left[\sigma^2_{\Delta S_{\mathrm{M}}}(T_i + \Delta T_i) + \sigma^2_{\Delta S_{\mathrm{M}}}(T_i)\right] \tag{4.34}$$

An alternative definition is given by approximating the integral as

$$\mathrm{RC}_{\mathrm{FWHM}} = \Delta S_{\mathrm{M}}^{\mathrm{peak}} \delta T_{\mathrm{FWHM}} \tag{4.35}$$

where $\Delta S_{\mathrm{M}}^{\mathrm{peak}}$ is the peak value of ΔS_{M} and δT_{FWHM} is the temperature range of full width at half maximum of the peak. This definition is due to the usually very sharp and tight peak form, but here we use the definition from equation 4.32.

Thinking about the refrigerant capacity can be a bit misleading. As mentioned it is an energy flow between the hot and cold region in a magnetic refrigeration cycle. The refrigerant capacity however does not take the specific heat capacity of the material into account. This can be easily understood by remembering the definition of the heat capacity. It is defined as the amount of energy a body needs to absorb, in order to raise its temperature.

The refrigerant capacity only defines how much energy flows between the hot and cold temperature regions. It does not tell us anything about how much a body warms up from this energy flow. Materials with a big specific heat will absorb a big amount of energy and experience a lower adiabatic temperature change than materials with low heat capacities. To obtain a big refrigerant capacity, we want a big magnetic entropy change over a temperature range as wide as possible.

4.7 The Giant Inverse Magnetocaloric Effect

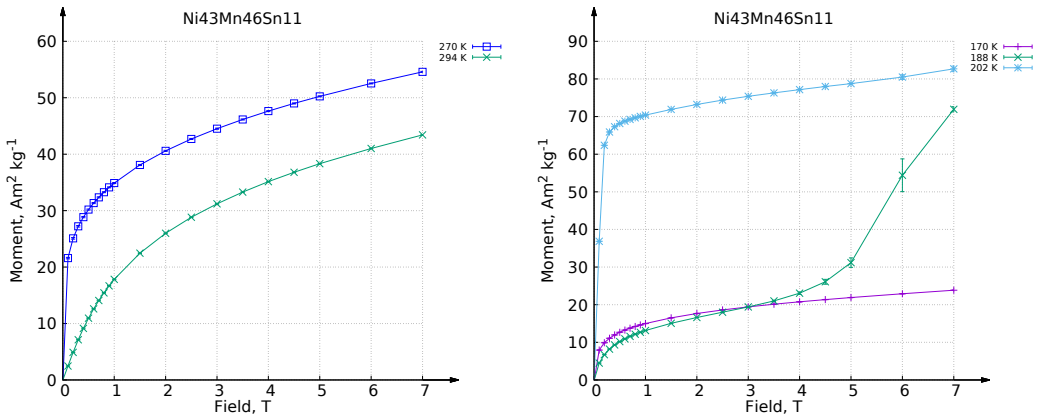

(a) At high temperatures without a phase transition

(b) Over the phase transition

Figure 4.5: Examples for isothermal magnetization measurements.

We now have equations to analyse the magnetic entropy change and adiabatic temperature change. However these equations alone describe a general change of entropy and temperature, and not the giant magnetocaloric effect itself. So far we only mentioned the giant MCE in section 4.1 and did show a corresponding entropy change in figure 4.4.

In section 4.4 we mentioned that the calculation of ΔS_{M} is done with isothermal magnetization curves. If the measurements of two different temperatures are similar to each other, the entropy change will be small. The phase transition of the giant MCE materials however leads to big changes in magnetization over a short temperature range. As derived in equation 4.18, the magnetic entropy change simplifies to the difference of two isothermal magnetization curves. If the magnetization shows big changes, it will result in a big entropy change. This is the reason why it is called the *giant* effect.

Figure 4.5 gives two examples for this. In figure 4.5a we have two measurements at different temperatures without a phase transition. As expected the magnetic moment is higher for lower temperatures because of less thermal fluctuations. Figure 4.5b now shows how the magnetic moment changed over the phase transition with the giant inverse MCE. We see that the magnetization is stronger for 202 K than it is for 170 K.

The austenitic phase shows a larger magnetic order at higher temperatures than

the martensitic phase at low temperatures. Transitions between a low-temperature state, which zero-field order parameter is small or zero, and a high-temperature state, whose zero-field parameter is large, lead to an inverse magnetocaloric effect.[11, Box 1]

The measurement for 188 K shows the behaviour during the phase transition. For low fields it still behaves like in figure 4.5a, but as the magnetic field gets stronger the magnetic moment suddenly increases. The reason is that an applied magnetic field decreases the phase transition temperatures. We will see this effect in practice in section 6.1, when searching for the phase transition temperatures.

With a change as strong as this, it was questionable if few ramp up steps for high fields were enough. A measurement with more steps at high fields was performed to check this. The results are shown in figure 4.6. It shows no odd behaviour at higher fields. The discrepancy for 224 K at 4 T results from a double measurement of this point. It is the effect of the magnetic properties of the sample changing over time. This effect will be further discussed in section 4.9.

Not having to measure a lot of high field points is important for practical reasons. The performed isothermal measurements take a long time to finish (3 to 4 days). During this time the magnetic field repeatedly is ramped up to 7 T. With smaller field intervals, the He level of the SQUID would fall too low to safely allow that. Measurements then could only be performed over short temperature ranges.

This increase in magnetization is why it is called the *inverse* MCE. In the *regular* MCE, the magnetic moment would strongly decrease instead and result in a negative entropy peak. This also leads to a sign change of ΔT_{ad}. Instead of heating up, the material now cools down when getting magnetized. That means that in this case the magnetic order becomes more disturbed by an applied field during the phase transition.

4.8 Unit cell volume and valence electrons

The austenitic and martensitic phase transition temperatures are closely related to the structural state of the alloy. This also determines its magnetic properties. It was suspected that two main parameters affect the phase transition temperatures. Those are the size of the unit cell (Vcell) and the number of valence electrons per atom (e/a).[1]

The choice of elements for $Ni_{43}Mn_{46}Sn_{11}$ and $Ni_{44}Mn_{45}Sn_{11}$ was dictated by attempts to change the transition temperatures. Since Ni and Mn have a different

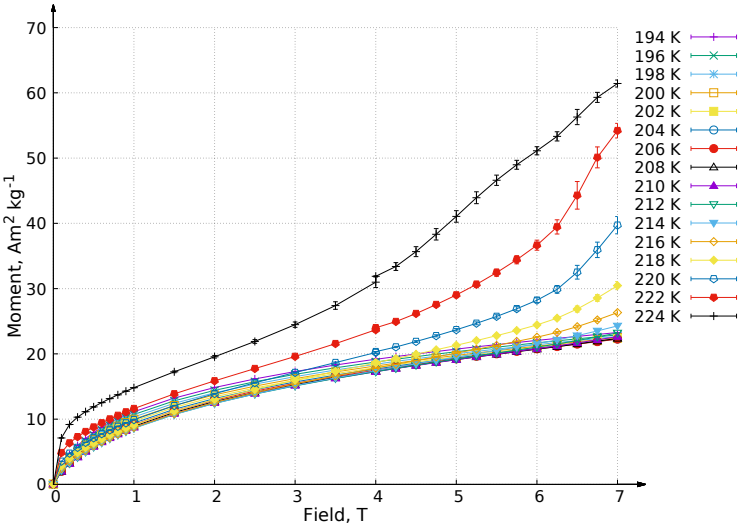

Figure 4.6: Isothermal magnetization of $Ni_{44}Mn_{45}Sn_{11}$ with more field intervals than usually.

amount of valence electrons (tab. 4.3), e/a should change. Increasing e/a was suspected to also increase the transition temperatures. It can be calculated with equation 4.36.

$$\mathrm{e/a} = \frac{1}{N}\sum_i q_i N_i \tag{4.36}$$

Here q_i are the valence electrons per element, N_i the number of atoms from the element and N the total number of atoms. N amounts to 100 because it stands for the atomic percent at%.§

This is only a theoretical approach. Publications have shown that the actual at% of elements can be noticeable different from their chemical formula.[20]

Finding the actual at% of elements in those alloys is an upcoming task of Dr. Marchenkov's group. They will also take a closer look at how the elements arrange in the lattice and if the expected ion radii of the elements are correct.

Table 4.3 shows that Ni and Mn both have an unfilled 3d subshell with a different amount of valence electrons. Since Ni has 3 more valence electrons, e/a should slightly increase. For samples $Ni_{43}Mn_{46}Sn_9Ge_2$ and $Ni_{43}Mn_{46}Sn_9Si_2$, Sn atoms were replaced with elements from the same group. These contain the same amount of valence electrons and should not change e/a.

§ Atomic percent. The relative representation of different elements in an alloy.

Table 4.3: Valence electron configuration[21, tab. 6.6] of used elements.

Element	Period	Group	electron configuration	valence electrons
Ni	4	10	[Ar] $3d^8 4s^2$	10
Mn	4	7	[Ar] $3d^5 4s^2$	7
Sn	5	14	[Kr] $5s^2 p^2$	4
Ge	4	14	[Ar] $4s^2 p^2$	4
Si	3	14	[Ne] $3s^2 p^2$	4

Table 4.4: Calculated valence electrons per atom.

Sample	e/a
$Ni_{43}Mn_{46}Sn_{11}$	7.96
$Ni_{44}Mn_{45}Sn_{11}$	7.99
$Ni_{43}Mn_{46}Sn_9Ge_2$	7.96
$Ni_{43}Mn_{46}Sn_9Si_2$	7.96

Calculated e/a for all samples in table 4.4 show a tiny increase for $Ni_{44}Mn_{45}Sn_{11}$ compared to the other 3.

The intention for samples $Ni_{43}Mn_{46}Sn_9Ge_2$ and $Ni_{43}Mn_{46}Sn_9Si_2$ was to change Vcell while not changing e/a. It was expected that a decrease of Vcell would increase the transition temperatures. However this turned out to not be true, as can be seen in chapter 6.1 and subsequent chapters.

Atomic radii in compounds are different from free atoms, depending on how the atoms affect each other. To better understand this an example image is given in figure 4.7, where the distance between ions can become bigger than their atomic/ionic radii. It is necessary to perform x-ray diffraction (XRD) in order to find the actual lattice constants.

Measurements where performed and provided by Dr. Marchenkov's group. They are shown in figure 4.8 for room temperatures. All samples show the same space group in the respective phases. For their space group in table 4.5, F stands for face centered while I means body centered.¶[22–24]

¶ I coming from the german *Innenzentriert*.

Table 4.5: Space groups for all samples in martensitic and austenitic phase. Provided by Dr. Marchenkov via private communication.

Phase	Shape	Space Group	Space Group #
Austenitic	cubic	$F\overline{m}3m$	225
Martensitic	tetragonal	I4/mmm	139

Table 4.6: Expected ions and radii for elements in the alloys, provided by Dr. Marchenkov via private communication.

Element	Ion Charge	Ion Radius
	e_0	pm
Ge	+2	73
Sn	+2	93
Si	−4	271

Expected ion radii for Heusler compounds can be seen in table 4.6. If an atom becomes negatively charged, its ion radius increases because the repulsion between the electrons increases. On the contrary for a positive ion the ion radius decreases, since there is less repulsion.[21, p. 103]

Introducing elements with different radii also leads to a change of *chemical pressure*. While *external pressure* gets applied externally to change a volume, chemical pressure comes internally from the elements in an alloy. Them occupying more are less space in the lattice, due to their ion radii, either decreases or increases the chemical pressure.

Table 4.6 shows that the expected ion radius for Si drastically increases for Si doping, while decreasing slightly for Ge doping. This means the chemical pressure from Si and Ge doping will be very different in sign and magnitude.

Lattice constants and Vcell for austenite and martensite phases are listed in tables 4.7 and 4.8 respectively. The martensite phase features a tetragonal ($a = b \neq c$) unit cell while the austenite phase is of cubic ($a = b = c$) shape.‖ The absolute errors are written in bracket notation where 1.01(20) corresponds to 1.01 ± 0.2.

‖ XRD patterns, lattice constants and lattice space groups for both phases where provided by Dr. Marchenkov via private communication.

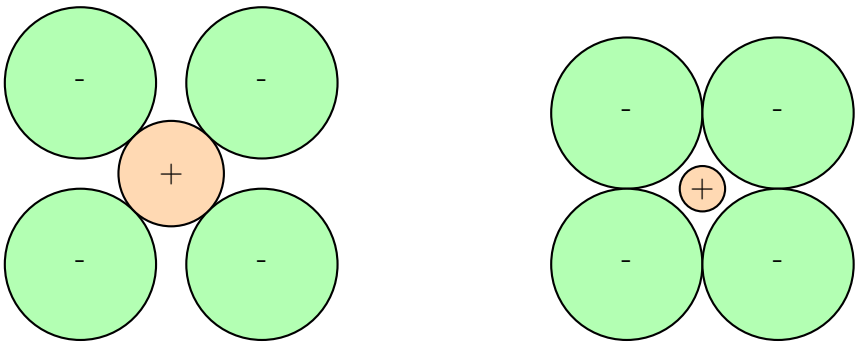

(a) Negative ions don't touch. **(b)** Positive ion too small to touch.

Figure 4.7: How different atomic radii affect the distance between ions. Pictures inspired by *Mortimer - Basiswissen der Chemie.*[21, section 7.7]

Values of Vcell are compared in table 4.9. It shows that the volume of the martensite phase is about half of the austenite one for all samples. As desired, Vcell decreases in both phases when doping with Ge and Si, with Vcell of $Ni_{43}Mn_{46}Sn_9Si_2$ being smaller than of $Ni_{43}Mn_{46}Sn_9Ge_2$.

However, the ratio of Vcell between both phases increases for doping with Si. The ratios for most samples are rather similar if you consider their standard deviations, but for Si doping the difference to Ge doping is bigger than one σ.

Uncertainties in table 4.9 were calculated with equation 4.38.

$$\sigma = \sqrt{\sigma_a^2\left(\frac{\partial f}{\partial a}\right)^2 + \sigma_b^2\left(\frac{\partial f}{\partial b}\right)^2}\Bigg|_{f=\frac{a}{b}} = \sqrt{\sigma_a^2\left(\frac{1}{b}\right)^2 + \sigma_b^2\left(-\frac{a}{b^2}\right)^2} \tag{4.37}$$

$$\sigma = \frac{a}{b}\sqrt{\left(\frac{\sigma_a}{a}\right)^2 + \left(\frac{\sigma_b}{b}\right)^2} \tag{4.38}$$

Table 4.7: Cubic lattice constants for austenitic phase. Results provided by Dr. Marchenkov via private communication.

Sample	$a = b = c$	Vcell
	Å	Å^3
$Ni_{43}Mn_{46}Sn_{11}$	5.9981(7)	215.79(4)
$Ni_{44}Mn_{45}Sn_{11}$	5.997(1)	215.66(8)
$Ni_{43}Mn_{46}Sn_9Ge_2$	5.9784(6)	213.68(4)
$Ni_{43}Mn_{46}Sn_9Si_2$	5.9702(4)	212.79(3)

Table 4.8: Tetragonal lattice constants for martensitic phase. Results provided by Dr. Marchenkov via via communication.

Sample	$a = b$	c	Vcell
	Å	Å	Å^3
$Ni_{43}Mn_{46}Sn_{11}$	4.162(2)	6.326(5)	109.6(1)
$Ni_{44}Mn_{45}Sn_{11}$	4.147(2)	6.374(5)	109.6(1)
$Ni_{43}Mn_{46}Sn_9Ge_2$	4.125(2)	6.370(5)	108.4(1)
$Ni_{43}Mn_{46}Sn_9Si_2$	4.135(2)	6.329(3)	108.20(8)

Table 4.9: Unit cell volume for the austenitic ($Vcell_A$) and martensitic ($Vcell_M$) phase. Comparison between tables 4.7 and 4.8. Uncertainties calculated with equation 4.38.

Sample	$Vcell_A$	$Vcell_M$	$Vcell_M/Vcell_A$
	Å^3	Å^3	
$Ni_{43}Mn_{46}Sn_{11}$	215.79(4)	109.6(1)	0.5079(5)
$Ni_{44}Mn_{45}Sn_{11}$	215.66(8)	109.6(1)	0.5082(5)
$Ni_{43}Mn_{46}Sn_9Ge_2$	213.68(4)	108.4(1)	0.5073(5)
$Ni_{43}Mn_{46}Sn_9Si_2$	212.79(3)	108.20(8)	0.5084(4)

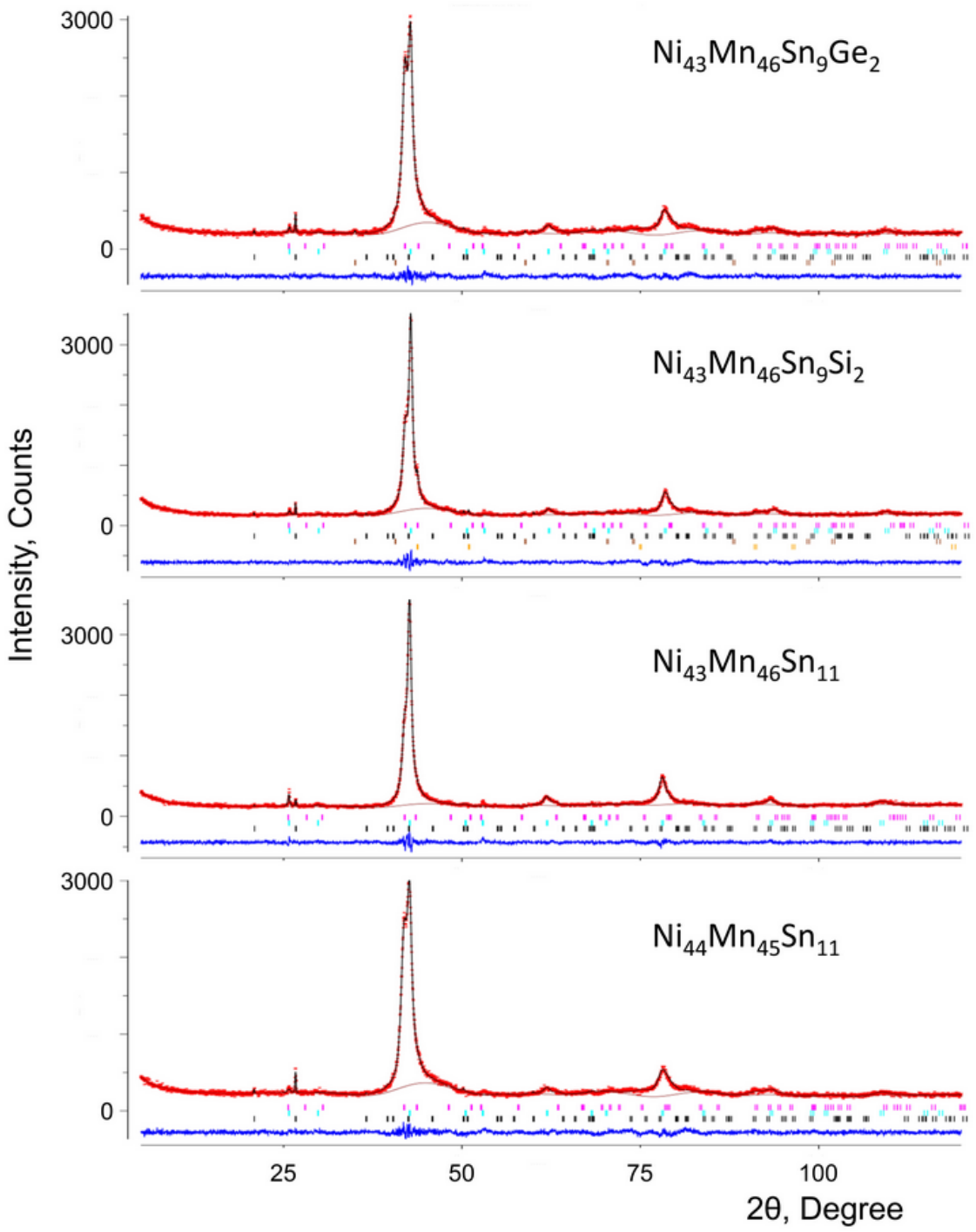

Figure 4.8: X-ray powder diffraction patterns of Heusler phases. The red crosses are experimental points, the solid black line is the calculated profile, and the vertical marks correspond to the positions of the Bragg reflections. The difference curve is plotted at the bottom of the figure. Graphs provided by Dr. Marchenkov via private communication.

4.9 Magnetic Ageing

(a) Before any field. **(b)** Aligned domain grows with field.

Figure 4.9: The size of magnetic domains in a ferromagnet changes with an applied magnetic field.

Magnetic ageing describes the change of magnetic properties in ferromagnetic materials over time. It can be caused by change in the magnetic domains (reversible) or its crystal structure (irreversible). The reversible effect is caused by external influences like magnetization, temperature changes or mechanical manipulation (e.g. vibration). Repeated magnetization can restore the original magnetization of the sample.

This change in magnetic properties over time dictates some restrictions on how we can process the measured data. For the magnetic entropy change we need isothermal magnetization measurements.

The magnetic field is ramped up in multiple steps, up to a total of 7 T. If there is no phase transition, we should get results like they were previously shown in figure 4.5a.

This remains true if there is no disturbance in the measurement procedure. The SQUID mechanics are usually reliable enough to guarantee nearly equal waiting times between heating, charging and measurement.

It is however not possible to directly compare two individually performed magnetization measurements, because the absolute magnetic moment has changed. Figure 4.10 shows an example for this. In figure 4.10b a result like in figure 4.5a was expected. However the magnetic moment measurements cross over and at 7 T, the magnetization is even stronger for the higher temperature.

Unlike discussed in section 4.7, this is not due to a phase transition. It is the result of a change in magnetic properties. Since calculation of the magnetic entropy

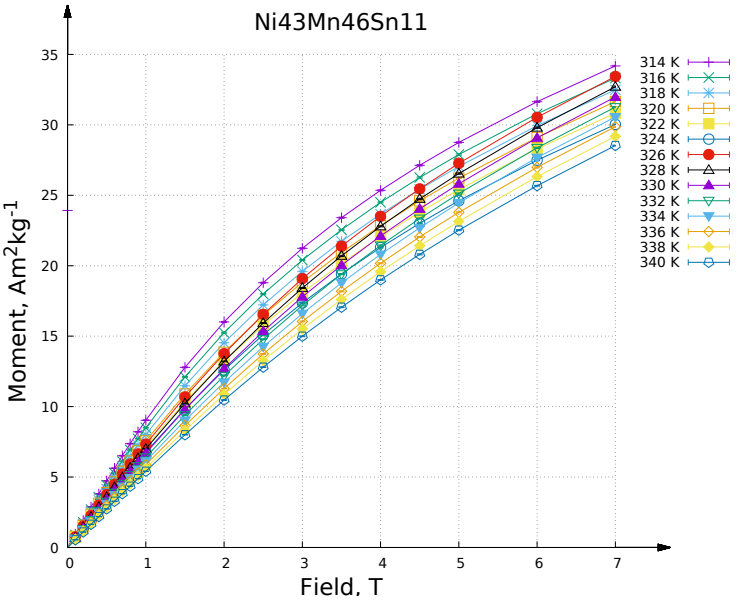

(a) What such an effect will produce.

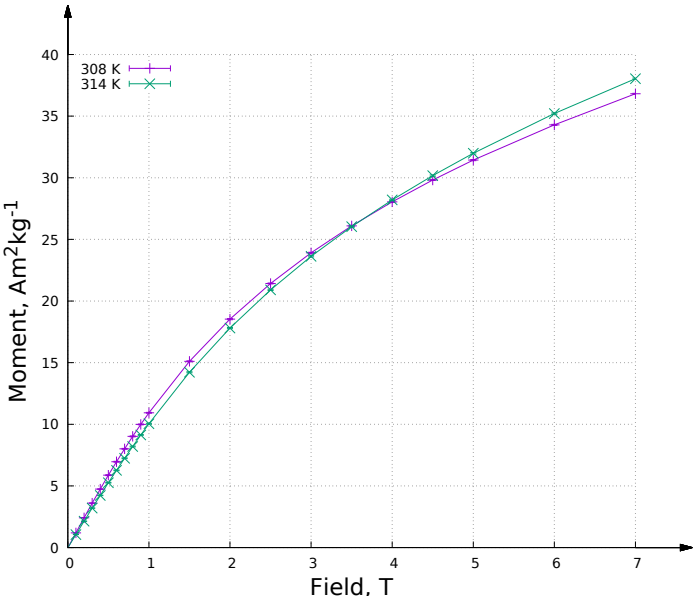

(b) Two example temperatures.

Figure 4.10: Figure 4.10a: Magnetic ageing produces a change in magnetization. Figure 4.10b: After measuring isothermal magnetization for 308 K, the sample was stored at room temperature in an envelope at the laboratory for 3 days, while the SQUID was used for other experiments. This leads to magnetization curves overlapping when they shouldn't. With $T_c = 274$ K those measurements are about 40 K above T_c. Both graphs are from $Ni_{43}Mn_{46}Sn_{11}$, which was measured 3 times at high temperatures. Figure 4.10a compares the 2nd and 3rd, figure 4.10b the 1st and 2nd measurements.

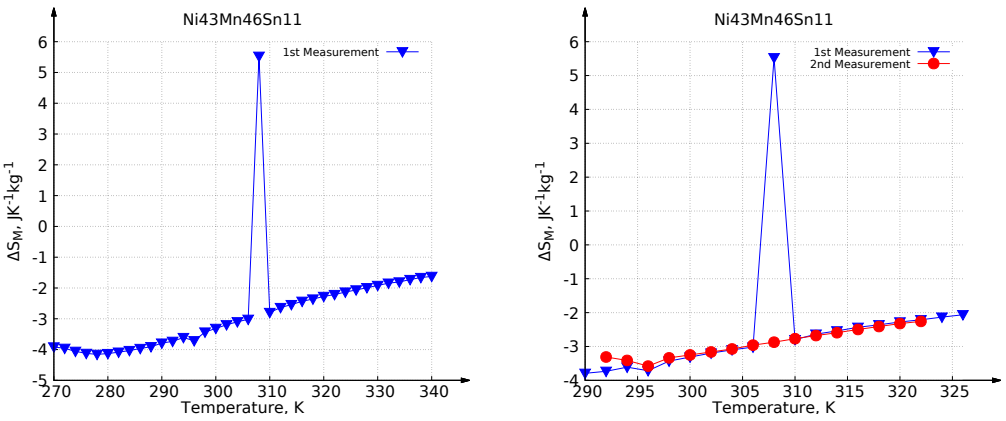

(a) Combining different measurements produces errors.

(b) Red dotted line is the actual ΔS_{M}.

Figure 4.11: Entropy of $Ni_{43}Mn_{46}Sn_{11}$ calculated from isothermal magnetization measurements. Figure 4.11a shows errors due to the change of magnetic properties when measurements from 2 different sessions are combined. A spike appears at the temperature where the data are combined. Figure 4.11b shows results of a third measurement and the correctly measured entropy change.

change requires isothermal measurements between two temperatures, this would lead to erroneous results.

Consequences can be seen in figure 4.11a. Isothermal magnetization measurements were performed with a break in between. The measurement procedure was paused after 308 K and continued a few days later.

During the pause, the sample was stored at room temperature. The magnetization at 310 K then was stronger than it would have been in an uninterrupted procedure. This resulted in the spike at 308 K in figure 4.11a.

However calculation of the magnetic entropy change can still be done with individually measured data, if there is an overlap in measured temperatures. Figure 4.11b shows results from a third measurement which examined the error at 308 K.

Apart from 308 K the results are in good agreement with each other. The discrepancies near 294 K are again from different magnetic properties of the sample. It wasn't heated up from lower temperatures before the measurement was started.

This shows that magnetic entropy changes from different measurements can be compared, as long as they are calculated individually.

Figure 4.12 shows magnetic ageing for subsequent temperature cycles. The magnetic moment becomes weaker with each cycle performed. For these cycles the sample is cooled down at zero field first. Then the magnetic field is charged and

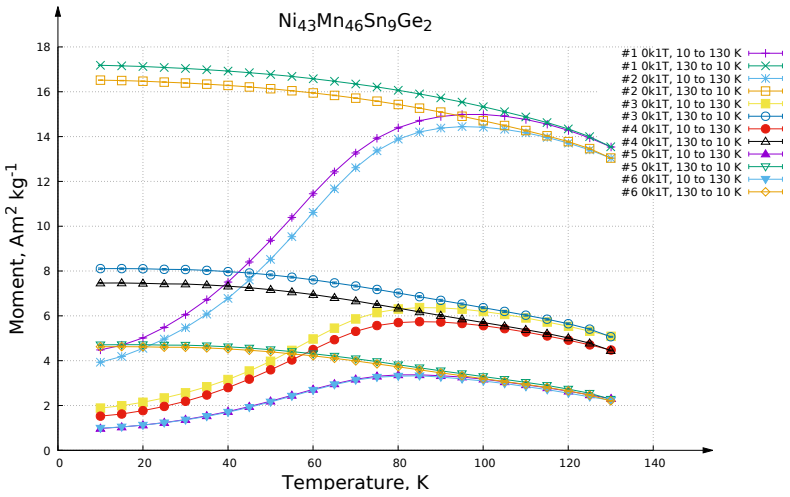

Figure 4.12: The magnetic moment gets weaker with each performed temperature cycle.

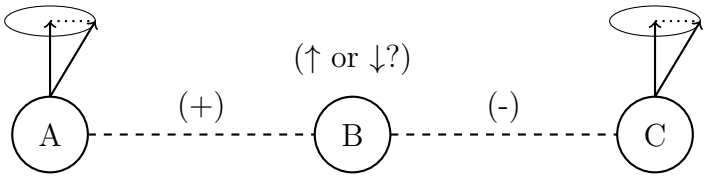

Figure 4.13: Ferromagnetic and Antiferromagnetic coupling between spins. B is *frustrated* because it can't decide if it wants to become an up or down spin.

afterwards the sample is heated up. After reaching the highest temperature it is cooled down again with the field remaining applied (also called field cooling, FC).

We see that the magnetic moment actually increases during the heating process until about 100 K. When cooled down with field the magnetization keeps increasing with decreasing temperature. This means that below 100 K the ferromagnet shows irreversible behaviour.[10, p. 23]

Similar measurements are usually observed for superparamagnetism of nanoparticles.[25][26]

For Ni-Mn alloys there have been publications to describe this effect as a combination of superparamagnetism and spin glass freezing.[20, fig. 2][27–29]

For Ni-Mn-Sn alloys, coexistence of ferromagnetic and antiferromagnetic order has been observed.[30]

Spin glasses originate from competition between ferromagnetic and antiferromagnetic couplings of the spins. At low temperatures they are frozen in an arbitrary state with disordered spins. Figure 4.13 illustrates the problem. Spins A and B have

ferromagnetic coupling (+), B and C antiferromagnetic (-).

When reaching low temperatures, the system wants to minimize its energy by aligning the spins according to their coupling. If A and C are both up spins, then B can't decide if it wants to be an up or down spin. This phenomenon is called *frustration.*[27]

Answers to this effect are beyond the limits of this thesis. Here we only handle the giant inverse MCE and calculate the corresponding magnetic entropy change and refrigerant capacity for the phase transition and at high temperatures.

5 Curie Temperature

In ferromagnetic materials, the magnetic moments are coupled by long range interactions, which leads to formation of magnetic domains. If the ferromagnet is heated above a certain temperature, the thermal energy becomes bigger than this interaction. This leads to disorder of the magnetic moments in the individual magnetic domains. Above this temperature, a ferromagnet shows paramagnetic behaviour. This temperature is called the Curie temperature T_c.[31]

5.1 Magnetic Susceptibility

The relation between magnetic flux density $\vec{\mathbf{B}}$, magnetic field strength $\vec{\mathbf{H}}$ and magnetization $\vec{\mathbf{M}}$ is given by equation 5.1.*

$$\vec{\mathbf{B}} = \mu_o\Big(\vec{\mathbf{H}}_{\text{vac.}} + \vec{\mathbf{M}}\Big) \tag{5.1}$$

The magnetic response function, called *magnetic susceptibility*, is defined as the change of magnetization by magnetic field.

$$\chi_{ij} = \frac{\partial M_i}{\partial H_j} \tag{5.2}$$

If the magnetization is a linear function of the applied magnetic field $M(H)$, this relation simplifies.

$$\chi = \frac{M}{H} = \frac{\mu_0 M}{B} \tag{5.3}$$

This is normally the case if the material is para- or diamagnetic and for weak magnetic fields.

By using $\vec{\mathbf{M}} \approx \chi\vec{\mathbf{H}}_{\text{vac.}}$, we can transform equation 5.1.[31, sec. 3.5.2]

∗ Spoken names of $\vec{\mathbf{B}}$ and $\vec{\mathbf{H}}$ vary in literature. We just refer to them as $\vec{\mathbf{B}}$ and $\vec{\mathbf{H}}$.

Table 5.1: Comparison of χ and μ_r for different forms of magnetism. For ferro- and antiferromagnetism, both depend on the applied field.[5][31]

magnetism	χ	$\lvert\chi\rvert$	μ_r
paramagnetic	> 0	$\ll 1$	> 1
diamagnetic	< 0	$\ll 1$	< 1
	$\chi(H)$	$\lvert\chi(H)\rvert$	$\mu_r(H)$
ferromagnetic	> 0	$\gg 1$	$\gg 1$
antiferromagnetic	< 0	$\gg 1$	$\ll 1$

$$\vec{\mathbf{B}}_{\text{mat.}} = \underbrace{(1+\chi)}_{\mu_r}\mu_0\vec{\mathbf{H}}_{\text{vac.}} = \mu_r \underbrace{\mu_0\vec{\mathbf{H}}_{\text{vac.}}}_{\vec{\mathbf{B}}_{\text{vac.}}} = \mu_r\vec{\mathbf{B}}_{\text{vac.}} \tag{5.4}$$

μ_r is called the *relative permeability* and is a material specific parameter.† Values for χ and μ_r differ for different forms of magnetism, as can be seen in table 5.1.

For a pure antiferromagnet, the magnetization vanishes completely below its Neel temperature. The more general form is called ferrimagnetism, where sublattices with different magnetizations show antiparallel coupling. This results in a hyperbolic M-T (magnetization vs temperature) curve.[5]

By looking at χ, the *response* of the magnetic system, we can determine its type of magnetism. This can be done by performing M-$\mu_0 H$ (magnetization vs external magnetic field) measurements, usually done in hysteresis loops.

A different approach is possible by using the Curie-Weiss law, shown in section 5.2.

5.2 Curie-Weiss Law

Curie's law describes χ for ideal paramagnetism, depending on temperature T, with the Curie constant C.

$$\chi = \frac{C}{T} \tag{5.5}$$

† Compared to cgs system: $\vec{\mathbf{B}} = \vec{\mathbf{H}} + 4\pi\vec{\mathbf{M}}$ and $\vec{\mathbf{B}} = \mu\vec{\mathbf{H}}$ with μ as material specific parameter. In vacuum, where $\mu = 1$, this becomes $\vec{\mathbf{B}} = \vec{\mathbf{H}}$.

This means the inverse susceptibility, $1/\chi = T/C$ is linear in temperature and passes through the origin at $T = 0$.

A ferromagnet shows paramagnetic behaviour above its Curie temperature T_c. Equation 5.5 can be modified by introducing the temperature offset T_c and a critical exponent γ. This exponent has typical values between 1 and 1.5.[31]

$$\chi = \frac{C}{(T - T_c)^\gamma} \tag{5.6}$$

For $T \gg T_c$ and small γ, χ can be approximated by the Curie-Weiss law. There, T_c is replaced with the Weiss constant Θ_c. This again describes a linear $1/\chi$ behaviour in temperature for the paramagnetic phase, but with $\Theta_c > T_c$.

$$\widetilde{\chi} = \frac{C}{T - \Theta_c} \tag{5.7}$$

If we measure in a constant magnetic field, equation 5.3 simplifies.

$$\frac{1}{\chi} = \frac{H}{M}\Big|_{H=\text{const.}} = \frac{\text{const.}}{M} \propto \frac{1}{M} \tag{5.8}$$

With the high temperature behaviour for ferromagnetism, we obtain equation 5.9.

$$\frac{1}{\chi} = \frac{(T - T_c)^\gamma}{C} = \frac{H}{M}\Big|_{H=\text{const.}} \propto \frac{1}{M} \quad \forall\, T > T_c \tag{5.9}$$

Therefore, in M-T measurements $1/\chi$ is proportional to $1/M$, with the magnetic field acting as a scaling factor. This only works as long as $M = \chi H$ remains true, since it is only an approximation.

For ferromagnetism the behaviour above T_c is not exactly linear, but is affected by the critical exponent γ. Equation 5.10 describes temperature dependence of $1/\chi$ in constant magnetic fields for paramagnetism, 5.11 for ferromagnetism with $T > T_c$.

$$\frac{1}{\chi} \propto \frac{1}{M} \propto T \quad \text{(paramagnetism)} \tag{5.10}$$

$$\frac{1}{\chi} \propto \frac{1}{M} \propto (T - T_c)^\gamma \quad \text{(ferromagnetism } T > T_c\text{)} \tag{5.11}$$

Figure 5.1a shows typical behaviour for a ferromagnet. The critical exponent is small enough for an almost linear $1/M$ for $T \gg T_c$, but shows clear curvature near T_c. Performing a linear fit from high temperatures to $1/M = 0$ would yield a positive Θ_c with $\Theta_c > T_c$. A $\Theta_c > 0$ indicates ferromagnetic interaction, while $\Theta_c < 0$ would

correspond to antiferromagnetism.[10, p. 20, fig. 8]

We can see that the magnetization doesn't actually reach $M = 0$ at T_c. The theoretically sharp magnetic phase transition is usually smoothed out due to inhomogeneities and interactions in the material.[32, fig. 1][33, p. 77]

The difference between T_c and Θ_c will increase if you fit from higher temperatures, because the critical exponent γ is not exactly one.‡

The M-T curve in figure 5.1a (green curve) shows a clear change in curvature at T_c. From a mathematical perspective, this defines an inflection point of the curve. An inflection point is defined by $\mathrm{d}^2 f(x)/\mathrm{d}x^2 = 0$ and thus a maxima or minima in $\mathrm{d}f(x)/\mathrm{d}x$. This way we can obtain T_c by looking at $\mathrm{d}M/\mathrm{d}T$.[32][34]

We use numerical differentiation to calculate $\mathrm{d}M/\mathrm{d}T$.

$$\frac{\mathrm{d}M}{\mathrm{d}T} \approx \frac{M(T + \Delta T) - M(T)}{\Delta T} \tag{5.12}$$

We then can find T_c by looking at the minima in figure 5.1b. It shows T_c at 278 K.

There are also other methods to find T_c. In section 5.3 we will discuss the Arrott plots, introduced by Anthony Arrott, for ferromagnetic to paramagnetic transitions.[35]

‡ Landau theory predicts $\gamma = 1$. This is not observed experimentally.

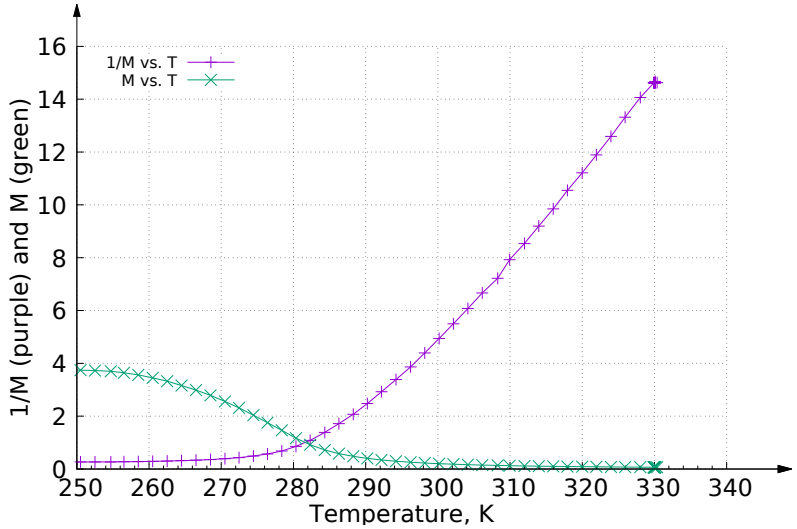

(a) M and $1/M$ plotted over temperature with $T_c = 278$ K and $\Theta_c \approx 286$ K. Measurement in $B = 0.1$ T. M in units of $\mathrm{Am^2\,kg^{-1}}$.

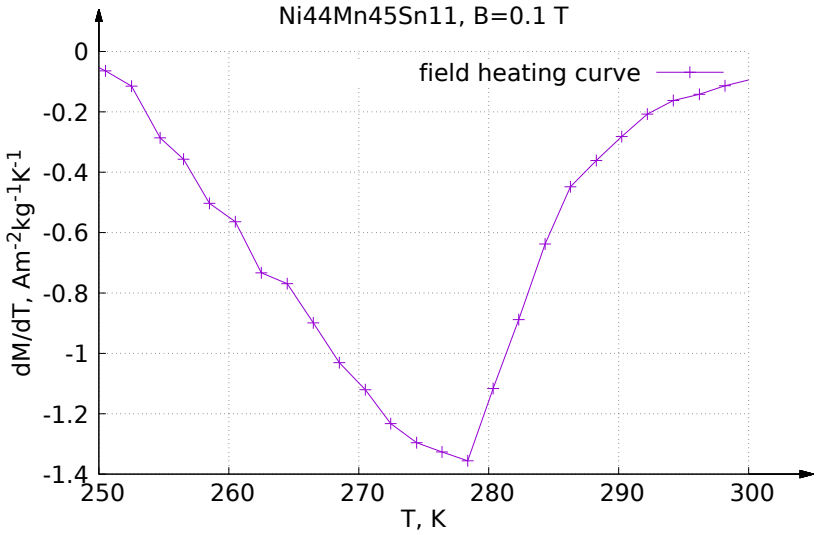

(b) $\mathrm{d}M/\mathrm{d}T$ shows a minimum at 278 K, which is the Curie temperature T_c.

Figure 5.1: Obtaining T_c by M-T measurements in constant magnetic fields for $Ni_{44}Mn_{45}Sn_{11}$.

5.3 Arrott Plots

The method of Arrott plots uses M-$\mu_0 H$ measurements to determine T_c. Anthony Arrott showed 2 proofs in his publication. One featured the the Weiss-Brillouin molecular field treatment, the other was for a generalized molecular field. Here we will only discuss the general proof. For more information, a look at the publication is recommended.[35]

This proof depends of the existence of an effective field $H_{\text{eff.}}$. In his own words:

> The more general proof of this relationship depends on the existence of something mathematically equivalent to an effective field, $H_{\text{eff.}}$. As long as the magnetization reverses without change in magnitude when $H_{\text{eff.}}$ is reversed, the magnetization is an odd function of $H_{\text{eff.}}$ and vice versa.[35]

Arrott used the alternative definition for the internal energy (see page 17, footnote). We will derive it in a form that is consistent with chapter 4.

The fields inside matter can be vastly different than the applied vacuum fields. This is due to the geometry of the sample and can be described with a demagnetization factor $\mathcal{N}$. The $\vec{\mathbf{H}}$ field transforms as shown in equation 5.13.[5, appendix][35]

$$\vec{\mathbf{H}}_{\text{i}} = \vec{\mathbf{H}}_{\text{vac.}} - \mathcal{N}\vec{\mathbf{M}} \tag{5.13}$$

The $\vec{\mathbf{B}}$ field transforms accordingly.

$$\vec{\mathbf{B}}_{\text{i}} = \mu_0\left(\vec{\mathbf{H}}_{\text{i}} + \vec{\mathbf{M}}\right) = \vec{\mathbf{B}}_{\text{vac.}} + \mu_0(1-\mathcal{N})\vec{\mathbf{M}} \tag{5.14}$$

Arrott's method is valid for fields that can be represented as a power series.

$$H_i = \frac{1}{\chi}M + \beta M^3 + \gamma M^5 + ... \tag{5.15}$$

$1/\chi$ vanishes at T_c, eliminating the linear term.

$$H_i = \beta M^3 + \gamma M^5 + ... \quad \forall \ T = T_c \tag{5.16}$$

For small magnetic moments M, we write the effective field $B_{\text{eff.}}$ as a power series in terms of M.

$$\frac{\mu B_{\text{eff.}}}{k_B T} = \alpha\, M + \beta\, M^3 + \gamma\, M^5 + ... \tag{5.17}$$

Here μ is the moment per atom, with units J/T. The quotient is dimensionless and the coefficients α, β, γ, ... have dimensions to the inverse power of the corresponding magnetization.§

There is a defined correlation between $B_{\text{eff.}}$ and the total energy E of the material. It can be obtained from the Guggenheim square in figure 4.3.

$$B_{\text{eff.}} = \frac{\partial E}{\partial M} \tag{5.18}$$

The energy E can be written as the following equation.¶

$$E = E_0 + B\,M + f(M) = E_0 + \mu_0 H\,M + f(M) \tag{5.19}$$

E_0 is the none magnetic contribution to the energy, $B\,M$ is the energy of the material in the external field B and $f(M)$ is the internal energy due to magnetization.

$f(M)$ is an even function, when the internal energy doesn't change upon reversal of magnetization. This means the contribution of $f'(M)$ to $B_{\text{eff.}}$ is an odd function.

$$B_{\text{eff.}} = \left(\frac{\partial E}{\partial M}\right)_S = B + f'(M) \tag{5.20}$$

$f'(M)$ can also be written as a power series and has units T.

$$f'(M) = a\,M + b\,M^3 + c\,M^5 + ... \tag{5.21}$$

We now express B in terms of $B_{\text{eff.}}$ and $f'(M)$.

$$B = B_{\text{eff.}} - f'(M) = \Big(\alpha\,M + \beta\,M^3 + ...\Big)\frac{k_B T}{\mu} - a\,M - b\,M^3 - .... \tag{5.22}$$

Rearrange by powers of M.

$$B = \left[\frac{\alpha k_B}{\mu a}T - 1\right] a\,M + ... \tag{5.23}$$

With $T_c = \mu a / k_B \alpha$, we end up for B near T_c with equation 5.24, where $\widetilde{A}$ and $\widetilde{B}$ are constants.

$$B = \mu_0 H = \epsilon\,M + \widetilde{A}\,M^3 + \widetilde{B}\,M^5 + ... \tag{5.24}$$

§ With M as $\mathrm{Am^2/kg}$, α as $\mathrm{kg/(Am^2)}$, β as $(\mathrm{kg/(Am^2)})^3$, ...

¶ For $E_0 = TS$ and $f(M) = 0$ this is the internal energy from table 4.1.

The important parameter for the Arrott plot is ϵ.

$$\epsilon = \left[\frac{T}{T_c} - 1\right] a \tag{5.25}$$

ϵ vanishes at T_c, leaving M^3 as the biggest contribution to the power series. If we plot $\mu_0 H$-M^3, we should see a straight line that passes through the origin, for an isothermal M-$\mu_0 H$ measurement at T_c. At other temperatures, the leading term ϵM will result in curvature, since we are plotting for M^3 instead of M. The sign of ϵ changes at T_c, and so will the curvature of the Arrott plot. Convex curves are below T_c and concave ones above it.

Arrott's original result (in Gaussian units) was equation 5.26, with magnetic field H and magnetization M.[35]

$$H = \epsilon M + \widetilde{A}\, M^3 + \widetilde{B}\, M^5 + ... \tag{5.26}$$

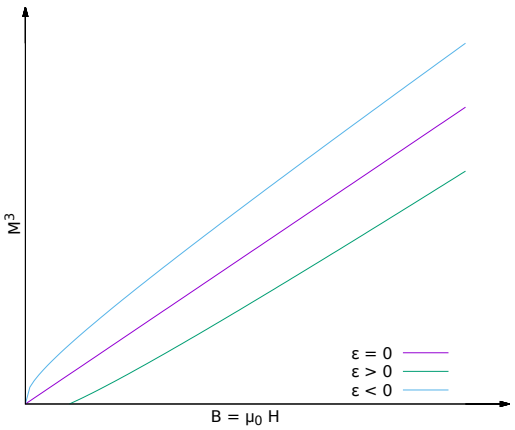

Figure 5.2: Example for an $\mu_0 H$-M^3 Arrott plot. $\epsilon < 0$ is ferromagnetic and shows convex curvature. $\epsilon = 0$ is linear and passes through the origin at $T = T_c$. $\epsilon > 0$ is paramagnetic end shows concave curvature.[35, fig. 1]

For SI units, the fields are proportional in vacuum $B_{\text{vac.}} = \mu_0 H_{\text{vac.}}$.

In practice, plots of M^2-H/M are often used, since $1/\chi = H/M$. Linear fits toward the origin are performed (from high fields to low fields) and T_c is determined by which fit passes through the origin.

In more recent history, there were also ideas to introduce critical exponents in this method, but we will not discuss those further.[36]

The $H \sim M^3$ behaviour is also predicted by the Landau theory of critical exponents.[37]

The field H is the applied external magnetic field, which in cgs system would be identical to B. In SI units we will plot M-H with $B = \mu_0 H$.

5.4 Critical Exponent

In section 5.2 we introduced the critical exponent γ for a ferromagnet above its Curie temperature. Since γ represents a (small) deviation from linear behaviour, it also has an influence on M-H measurements.

The magnetization of a paramagnetic system can be described by the Brillouin function.[5]

$$M(T, B) = M_0 \mathcal{B}_J(x) \tag{5.27}$$

$$x = \frac{g_J J \mu_B B}{k_B T} \tag{5.28}$$

$$\mathcal{B}_J(x) = \left(1 + \frac{1}{2J}\right) \coth\left[\left(1 + \frac{1}{2J}\right)x\right] - \frac{1}{2J} \coth\left(\frac{x}{2J}\right) \tag{5.29}$$

In this equations M_0 is the saturation magnetization ($\mathrm{Am}^2/\mathrm{kg}$), J the total angular momentum (dimensionless), g_J the g-factor (dimensionless), μ_B the Bohr magneton (J/T) and B the magnetic field (T).

For the classical approximation $J \to \infty$, $\mathcal{B}_J$ transforms into the Langevin function.

$$\mathcal{L}(x) = \mathcal{B}_\infty(x) = \coth x - \frac{1}{x} \tag{5.30}$$

Therefore, for a classical system we can describe the magnetization with the Langevin function.

$$M(T, B) = M_0 \mathcal{L}(x) \tag{5.31}$$

In table 5.2 we show the different limits of $\mathcal{B}_J$ for B and T variations.

For now, we are only interested for the behaviour in M-H measurements with constant temperatures. Typical results are demonstrated in figure 5.3. It can be seen that the maximum magnetization decreases with increasing temperature.

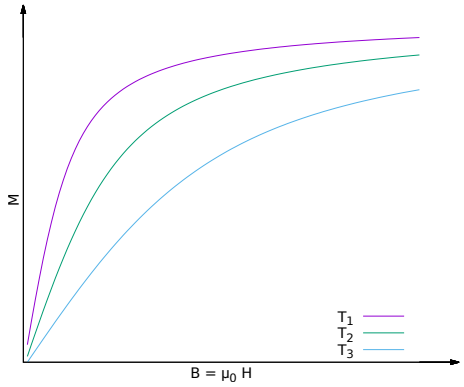

Figure 5.3: Typical Langevin functions for constant temperatures $T_1 < T_2 < T_3$ with varying magnetic field.

Table 5.2: Limits of the Brillouin function for variations of T and B.

B	T	x	$\mathcal{B}_J(x)$
$\to 0$	const.	$\to 0$	0
const.	$\to \infty$	$\to 0$	0
$\to \infty$	const.	$\to 1$	1
const.	$\to 0$	$\to 1$	1

For paramagnetism, when there is no interaction between the magnetic moments, the magnetization scales with temperature (eq. 5.32). So the isothermal curves in figure 5.3 would collapse into a single curve, if you plot M-H/T.[5]

$$\frac{1}{\chi} = \frac{H}{M} = \frac{T}{C} \propto T \quad \text{(paramagnetism)} \tag{5.32}$$

If we want to use this approach for a ferromagnet, we have to consider its Curie temperature and critical exponent.

$$\frac{1}{\chi} = \frac{H}{M} = \frac{(T - T_c)^\gamma}{C} \propto (T - T_c)^\gamma \quad \text{(ferromagnetism } T > T_c\text{)} \tag{5.33}$$

The correct plot would be M-$H/(T - T_c)^\gamma$. By this, the measurements should at least converge for weak magnetic fields.

Like mentioned at the end of section 5.3, for SI units we will plot M-$H/(T - T_c)^\gamma$.

6 Measurements

In this chapter we discuss the performed measurements. Section 6.1 shows the search for the phase transition temperatures, 6.2 isothermal magnetization measurements for ΔS_{M} calculation (see equations 4.18 and 4.21) and 6.3 the numerically calculated ΔS_{M}.

The resulting refrigerant capacities are discussed in chapter 7.

6.1 Temperature Cycles

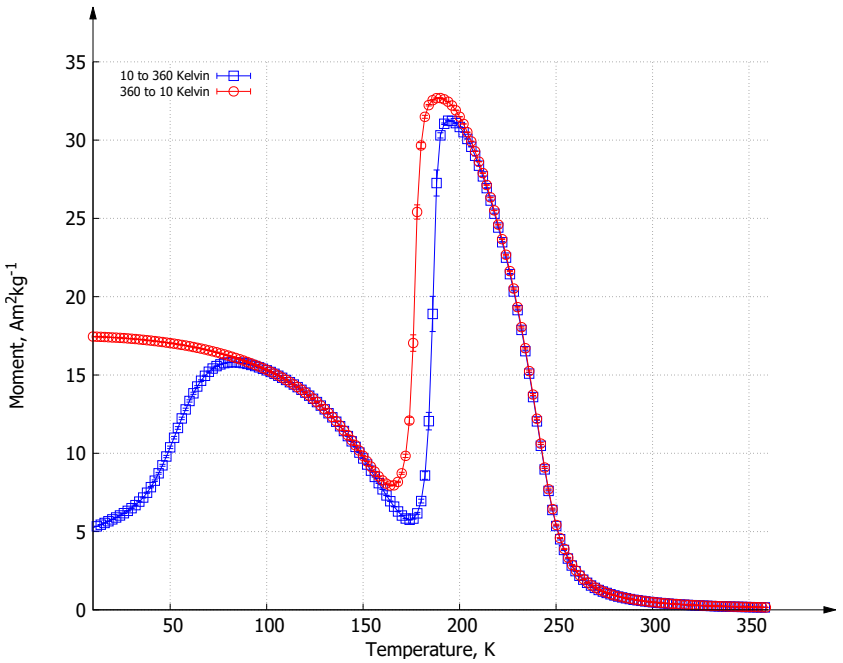

Figure 6.1: Temperature cylce of $Ni_{43}Mn_{46}Sn_9Si_2$ in a field of 0.1 T.

We start with temperature cycles in constant magnetic field. From these, we can obtain the start and end temperatures of the phase transition, as discussed in section 4.1. Figure 6.1 is an example of these measurement. In this figure we are interested in the behaviour between 150 and 200 K.

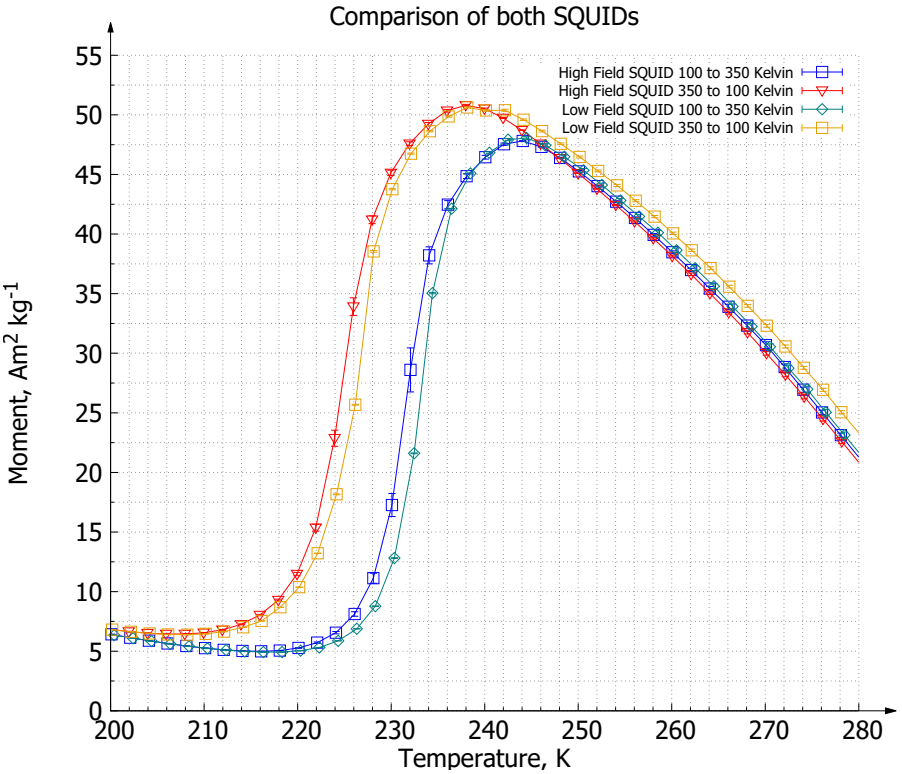

Figure 6.2: Comparison of $Ni_{44}Mn_{45}Sn_{11}$temperature cycles at 0.5 T in the 2 different SQUIDs.

The sudden change of magnetization is due to the phase transition. It happens at different temperatures depending, whether the sample is heated up or cooled down. This behaviour is called thermal hysteresis. Outside of the phase transition the magnetization is mostly the same, apart from very low values of temperatures, which are not considered here.

For these temperature cycles, the sample is inserted into the SQUID at low temperatures and zero field. This temperature is chosen a few K lower than the first measurement. The sample then is heated to the first temperature in the sequence at zero field. Then the magnetic field is charged and the magnetic moment is measured in increasing temperature intervals of 2 K.

Measurements are performed in fields of 0.1, 0.5, 1, 5 and 7 T. At the highest temperature in the sequence, the field remains charged and the measurements are repeated in decreasing temperature. These are also called field cooling measurements. Between cycles at different fields, the sample is heated up and cooled down in zero field.

The samples are very sensitive regarding to their thermal and magnetic history. Therefore, the temperature regulation in the SQUIDs posed a potential problem. The 1 T SQUID has shown a few problems with over heating while settling for a target temperature. If this effect were too big it could affect the observed transition temperatures.

A comparison measurement between the 1 T and 7 T SQUID with the same sequence was performed. The magnetic moment is shown in figure 6.2. Small differences can be observed in total magnetization but the transition temperatures are not affected.

6.1.1 Martensitic aus Austenitic phase transition

We define the thermal hysteresis as $\Delta T = \mathrm{A_{Start}} - \mathrm{M_{End}}$. This is the difference between the start of the austenitic and end of the martensitic transition. Sometimes it is difficult to decide which temperatures are the right choice for the transition temperatures. This is because it is usually somewhere between measured points. For our analysis this does not provide any problems, because we always approach from outside of the phase transition.

While the uncertainty in the temperatures may look quite large, its contribution to the magnetization changes becomes insignificant, because the contributions from the end point are very small.

In the following, we show a figure and a table for each sample, respectively. The transition temperatures are determined from the figures. Thermal hysteresis is calculated and put in the table, together with the transition temperatures. A general pattern for all samples is, that the phase transition temperatures shift to lower temperatures for higher magnetic fields. Thermal hysteresis doesn't change noteworthy for a each sample.

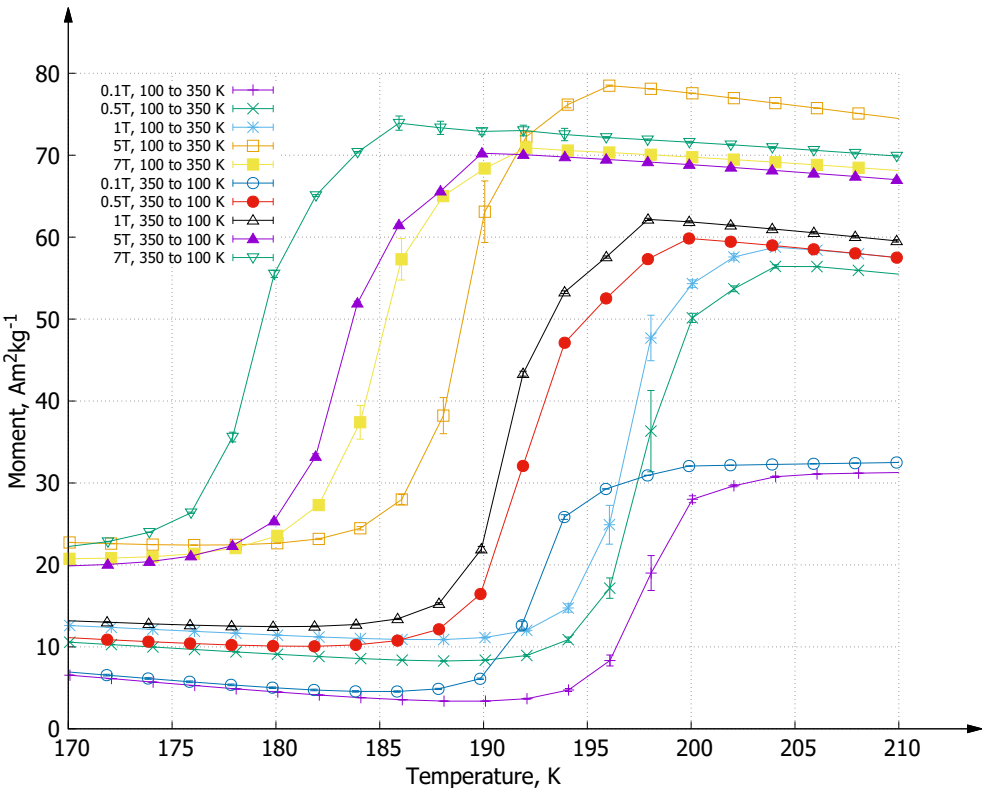

Figure 6.3: Temperature cycles of $Ni_{43}Mn_{46}Sn_{11}$.

Table 6.1: $M_{Start/End}$ and $A_{Start/End}$ of $Ni_{43}Mn_{46}Sn_{11}$.

	Temperature (K)				
Field (T)	M_{Start}	M_{End}	A_{Start}	A_{End}	$\Delta T(A_{Start} - M_{End})$
0.1	200	186	190	205	4
0.5	200	184	190	204	6
1.0	198	183	190	204	7
5.0	190	175	180	196	5
7.0	186	170	176	191	6

Measurements and transition temperatures of $Ni_{43}Mn_{46}Sn_{11}$ shown in figure 6.3 and table 6.1. We can see the transition shifting between 170 and 205 K in fields from 0.1 T to 7 T. Thermal hysteresis is around 6 K. The full transition decreases above 0.5 T.

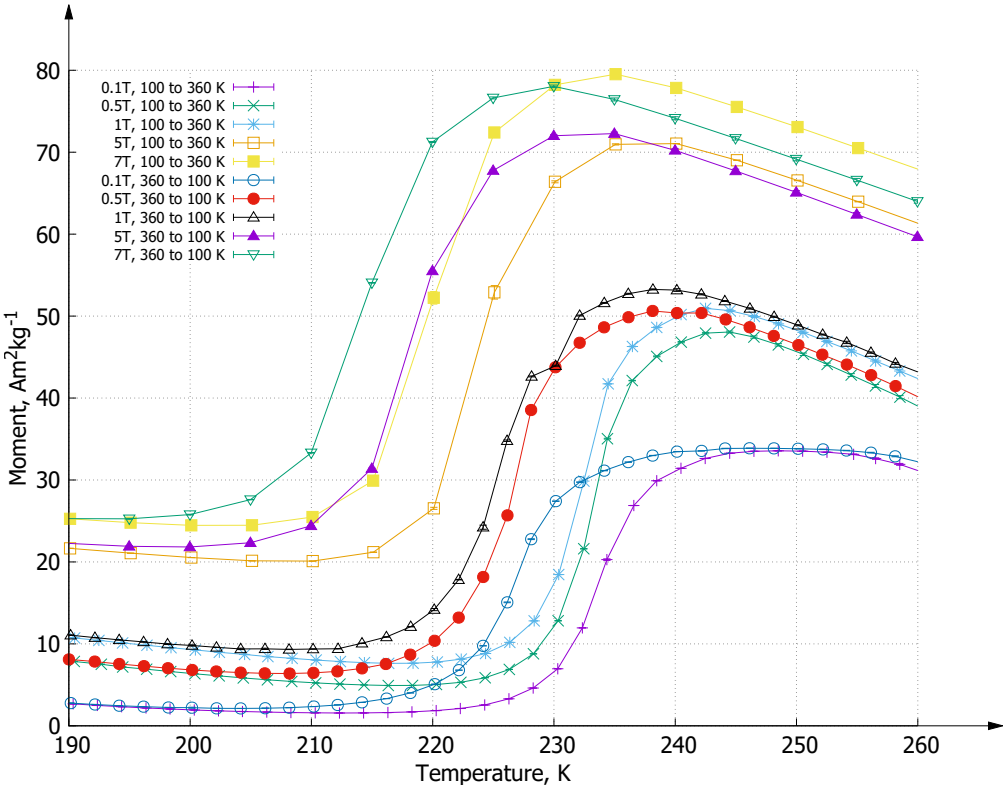

Figure 6.4: Temperature cycles of $Ni_{44}Mn_{45}Sn_{11}$.

Table 6.2: $M_{Start/End}$ and $A_{Start/End}$ of $Ni_{44}Mn_{45}Sn_{11}$.

	Temperature (K)				
Field (T)	M_{Start}	M_{End}	A_{Start}	A_{End}	$\Delta T(A_{Start} - M_{End})$
0.1	242	208	220	248	12
0.5	238	210	220	244	10
1.0	239	212	220	241	8
5.0	230	200	210	243	10
7.0	230	195	205	244	10

Temperatures of $Ni_{44}Mn_{45}Sn_{11}$ are shown in figure 6.4 and table 6.2. Replacing 1 % Mn with Ni has shifted the transition temperatures to a range between 195 and 240 K. This is a clear shift toward higher temperatures compared to $Ni_{43}Mn_{46}Sn_{11}$. Thermal hysteresis also has increased to 10 K.

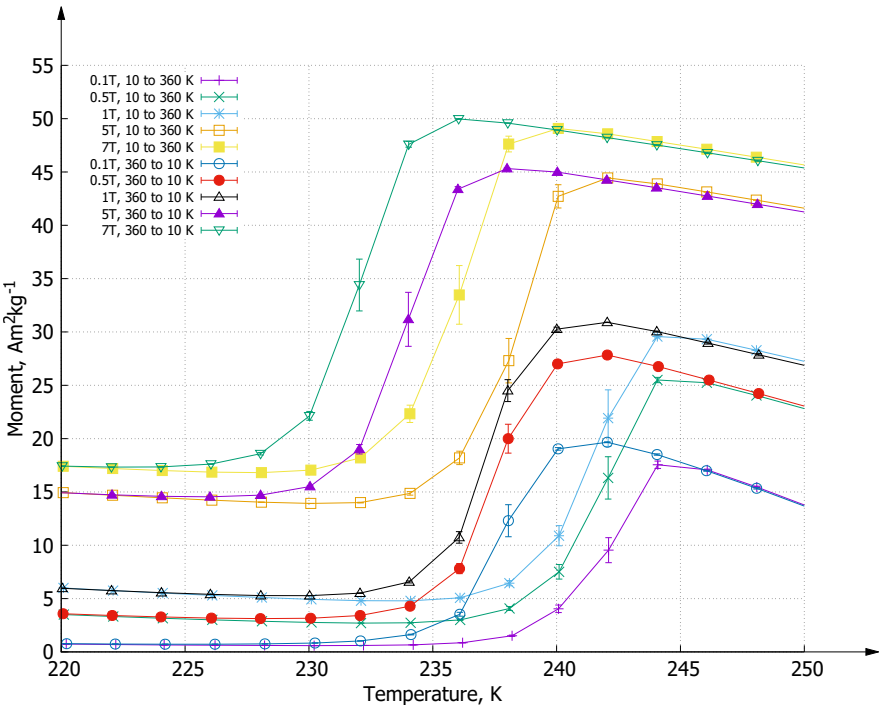

Figure 6.5: Temperature cycles of $Ni_{43}Mn_{46}Sn_9Ge_2$.

Table 6.3: $M_{Start/End}$ and $A_{Start/End}$ of $Ni_{43}Mn_{46}Sn_9Ge_2$.

	Temperature (K)				
Field (T)	M_{Start}	M_{End}	A_{Start}	A_{End}	$\Delta T(A_{Start} - M_{End})$
0.1	242	230	235	245	5
0.5	242	230	236	245	6
1.0	242	230	235	245	6
5.0	238	226	232	242	6
7.0	236	224	230	240	6

Figure 6.5 and table 6.3 present the results for $Ni_{43}Mn_{46}Sn_9Ge_2$. Doping with Ge_2 shifts the phase transition to temperature ranges between 230 and 245 K. This is even higher than $Ni_{44}Mn_{45}Sn_{11}$. Thermal hysteresis remains about 6 K.

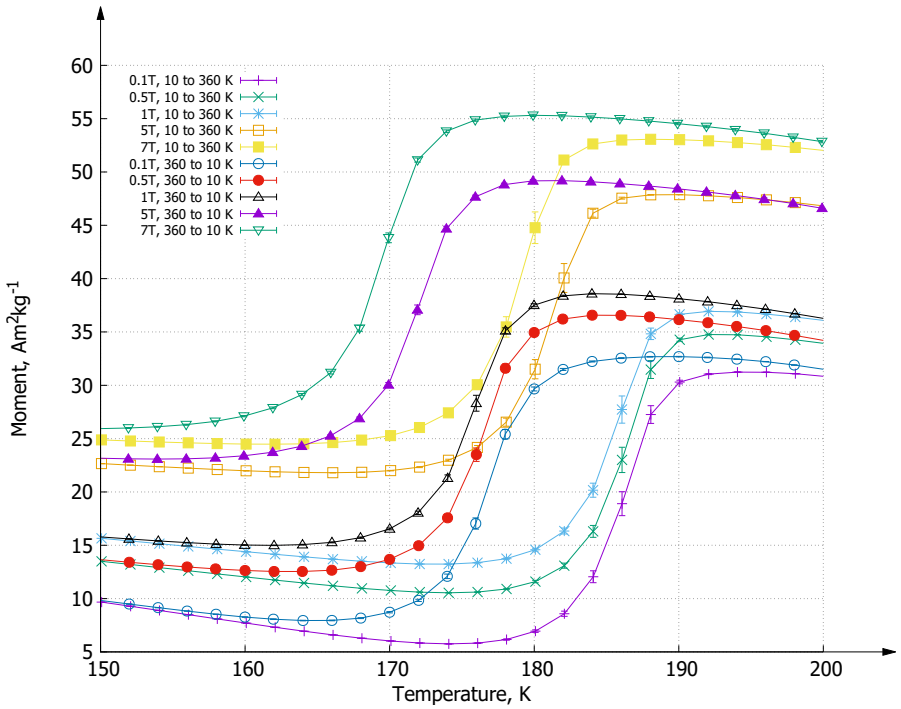

Figure 6.6: Temperature cycles of $Ni_{43}Mn_{46}Sn_9Si_2$.

Table 6.4: $M_{Start/End}$ and $A_{Start/End}$ of $Ni_{43}Mn_{46}Sn_9Si_2$.

	Temperature (K)				
Field (T)	M_{Start}	M_{End}	A_{Start}	A_{End}	$\Delta T(A_{Start} - M_{End})$
0.1	186	166	176	194	10
0.5	184	164	178	192	12
1.0	186	164	176	192	12
5.0	180	156	168	188	12
7.0	178	152	168	186	14

Measurements and transition temperatures of $Ni_{43}Mn_{46}Sn_9Si_2$ shown in figure 6.6 and table 6.4. The phase transition has shifted to lower temperatures than $Ni_{43}Mn_{46}Sn_{11}$. Thermal hysteresis is around 12 K.

The full temperature cycles of all samples are shown in figure 6.7. It was mentioned before that the martensitic transition temperatures are always lower than the austenitic ones. This mean the cooling down measurement for one sample is always the left curve when looking at the thermal hysteresis.

It is interesting that in figure 6.7a the magnetization of $Ni_{43}Mn_{46}Sn_{11}$ does barely change above 200 K for a field of 0.1 T. This is above the phase transition and the magnetic moment does even slightly increase for rising temperatures. At 250 K this behaviour ends and a strong decrease in magnetization follows over a range of 30 K.

$Ni_{44}Mn_{45}Sn_{11}$ shows the same decrease of magnetic moment over this temperature range. However its phase transition has shifted and its magnetization decrease follows directly after it.

$Ni_{43}Mn_{46}Sn_9Ge_2$ shows the same pattern but its total magnetic moment is much lower in weaker fields.

The phase transition for $Ni_{43}Mn_{46}Sn_9Si_2$ has shifted to lower temperatures than $Ni_{43}Mn_{46}Sn_{11}$. It also shows a sharp decrease in magnetization after the transition for higher temperatures. Compared to the other samples this one happens between 200 and 250 K.

For weak fields the total magnetization of $Ni_{43}Mn_{46}Sn_9Ge_2$ is much weaker than for the other 3 samples. The other samples reach similar maximum magnetic moments for 0.1 T. In higher fields $Ni_{43}Mn_{46}Sn_{11}$ and $Ni_{44}Mn_{45}Sn_{11}$ show stronger signals than the other two samples.

The important observation for us are the phase transition temperatures. In the section 6.2 we will use those to define temperature ranges for isothermal magnetization measurements. From these, we can calculate the magnetic entropy change and refrigerant capacity.

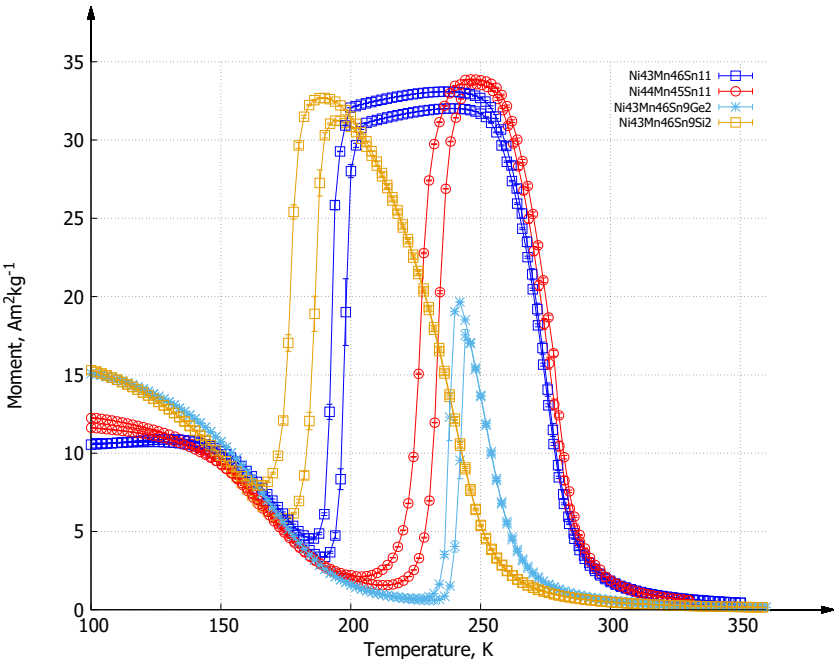

(a) 0.1 T.

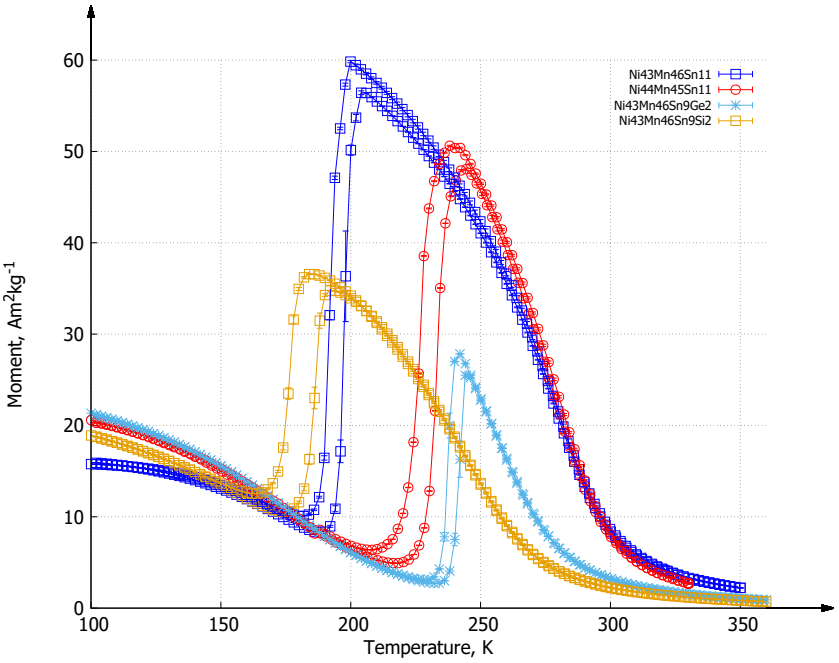

(b) 0.5 T.

Figure 6.7: Temperature cycles of all samples in various magnetic fields.

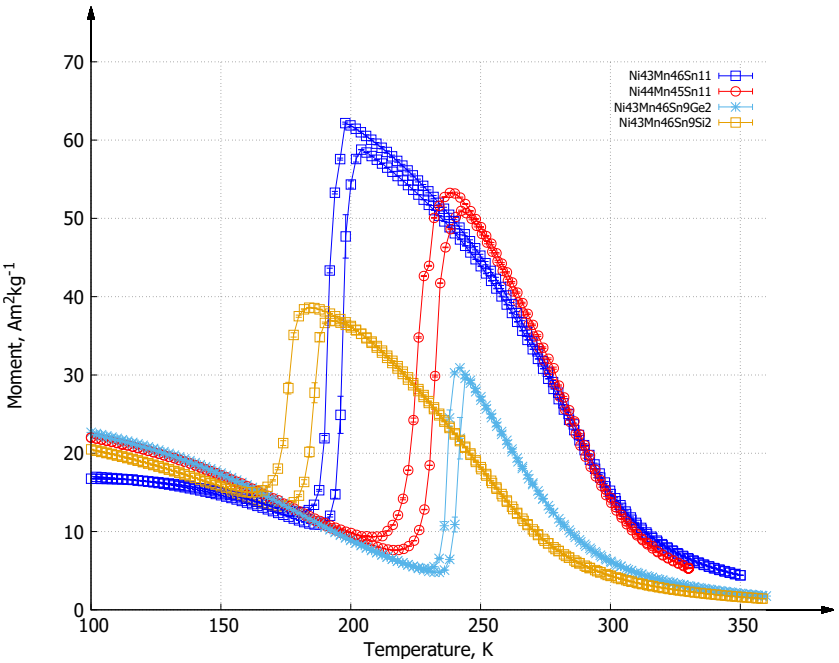

(c) 1 T.

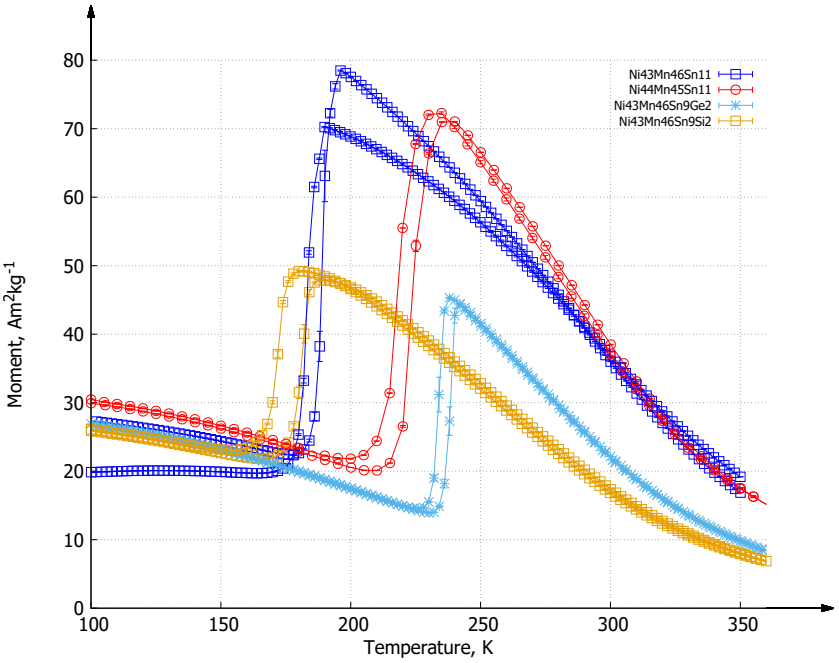

(d) 5 T.

Figure 6.7: Temperature cycles of all samples in various magnetic fields.

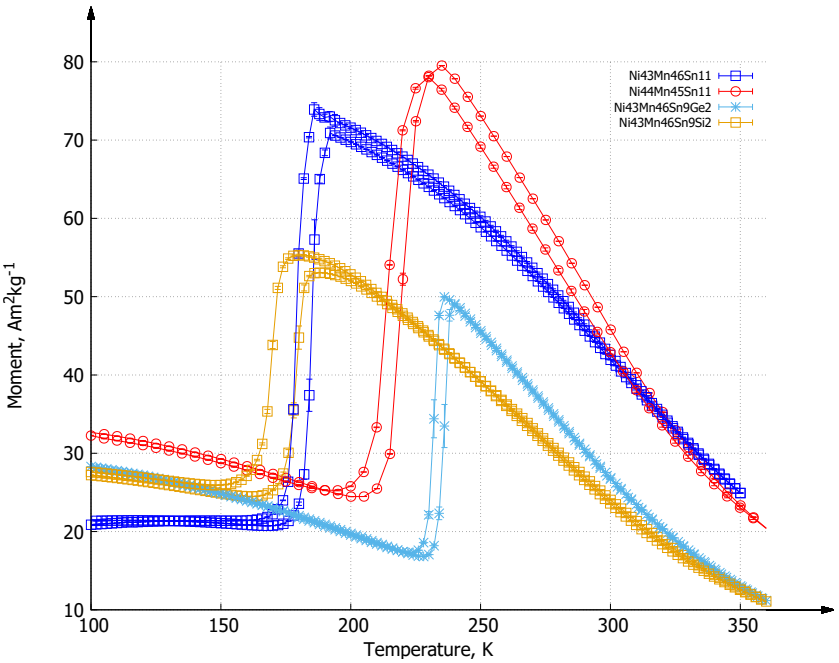

(e) 7 T.

Figure 6.7: Temperature cycles of all samples in various magnetic fields.

6.1.2 Curie Temperature

In section 5.2 we discussed how to find T_c from M-T measurements in constant magnetic fields.

Figure 6.8 shows $1/\chi \sim (T - T_c)^\gamma$ behaviour for $T > T_c$ with $1 < \gamma < 1.5$. The curves are nearly linear for high T, but near T_c the curvature due to γ is clearly visible.

$\mathrm{d}M/\mathrm{d}T$ was calculated for a field of 0.1 T in a heating process. The result is plotted in figure 6.9 and the T_c are listed in table 6.5. The T_c are defined by the 4 minima above 230 K. There is almost no difference for T_c between $Ni_{43}Mn_{46}Sn_{11}$ and $Ni_{44}Mn_{45}Sn_{11}$, which have a 1% difference in Ni and Mn at%.

By reducing the Sn content, which was done for samples $Ni_{43}Mn_{46}Sn_9Ge_2$ and $Ni_{43}Mn_{46}Sn_9Si_2$, T_c decreases by a lot. This is in good agreement with a publication for Ni-Mn-Sn alloys, where big increases in T_c were observed, when the Sn at% got bigger than 10%.[30, fig. 3a]

The publication also lists a graph for T_c in dependence of Sn at%, up to 40 percent. For $Ni_{50}Mn_{50-x}Sn_x$ samples, T_c is $\sim$ 240 K for $x = 10$ and increases to 320 K for $x = 13$. T_c reaches 360 K for $x = 40$.[30, fig. 3a]

The 4 big maxima in figure 5.2 are from the martensitic to austenitic phase transition. Since we used the heating measurement for calculation, these peaks are a bit more on the right than the ΔS_M peaks, which we will see later.

As we can see in figure 6.7, for T_c it doesn't matter if we use a heating or cooling curve, since magnetizations for both are identical in this region.

It can be seen that any linear fit would lead to a $\Theta_c > 0$ from to the Curie-Weiss law. This indicates dominance of ferromagnetic interaction.[10, p. 20, fig. 8]

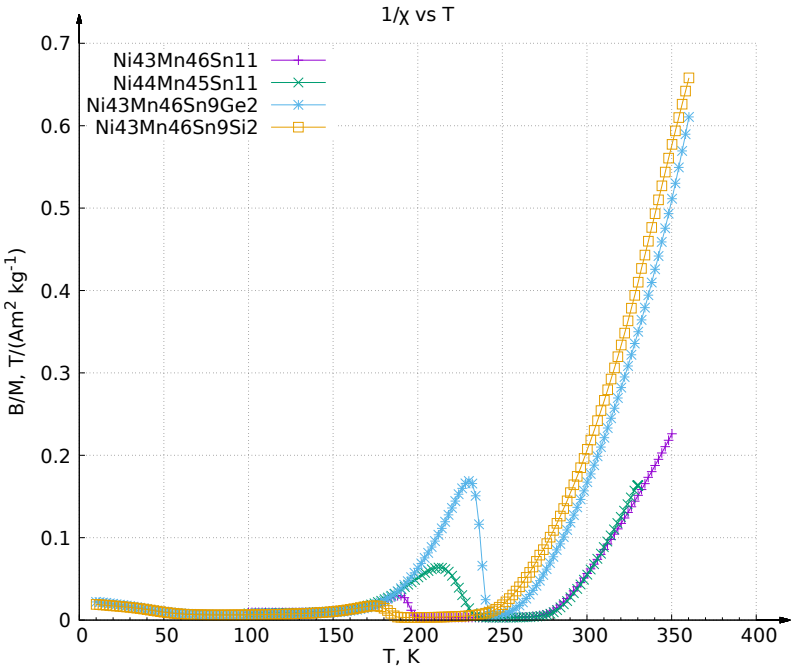

Figure 6.8: $1/\chi$ over temperature for all samples. Field heating curves in 0.1 T.

Table 6.5: T_c for all samples.

Sample	T_c (K)
$Ni_{43}Mn_{46}Sn_{11}$	274
$Ni_{44}Mn_{45}Sn_{11}$	278
$Ni_{43}Mn_{46}Sn_9Ge_2$	251
$Ni_{43}Mn_{46}Sn_9Si_2$	239

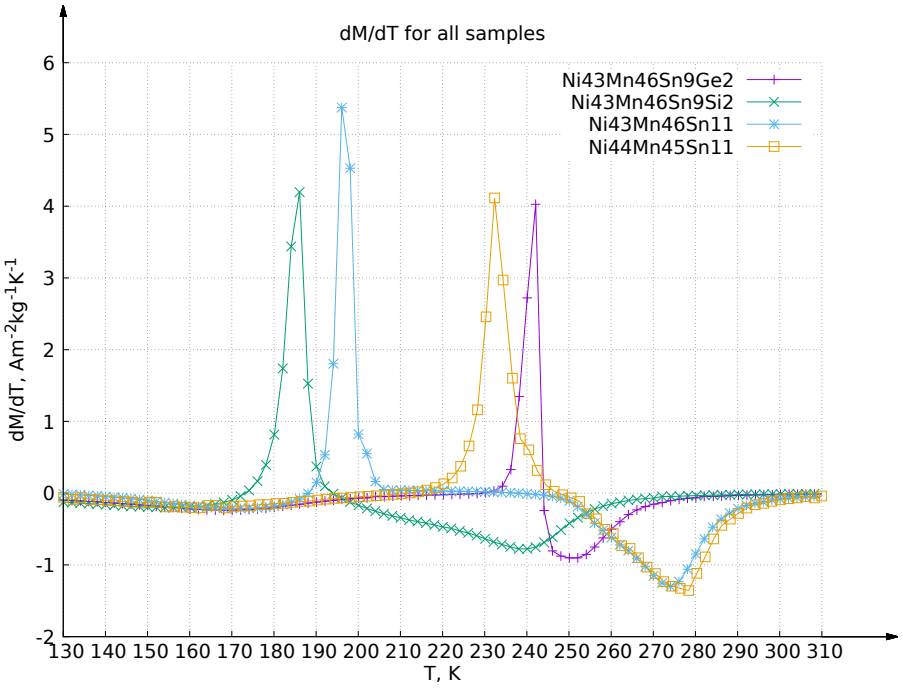

Figure 6.9: $\mathrm{d}M/\mathrm{d}T$-T of all samples for field heating in 0.1 T.

6.2 Isothermal Magnetization

In section 6.1 we performed measurements where we held the magnetic field constant and varied the temperature. In this section we present measurements at constant temperatures, in a magnetic field which is ramped up in multiple steps from 0 to $B_{\mathrm{max}} = 7$ T.

6.2.1 M-B measurements

In section 4.4 we derived an equation for the magnetic entropy change. It was also shown that it is an important parameter for the giant MCE. Equation 4.18 provided an approximation for its calculation. For this we need measurements of the magnetic moment at constant temperatures in increasing magnetic fields. We call this isothermal magnetization measurements. ΔS_{M} then can be interpreted as the difference of area under the plotted magnetization curves.

If a magnetic field is applied, the magnetic moments will begin to align. Thermal fluctuations work against the alignment and the magnetization will be lower for higher temperatures. For the giant inverse MCE the magnetization will increase over their phase transition. This means stronger magnetization for higher temperatures.

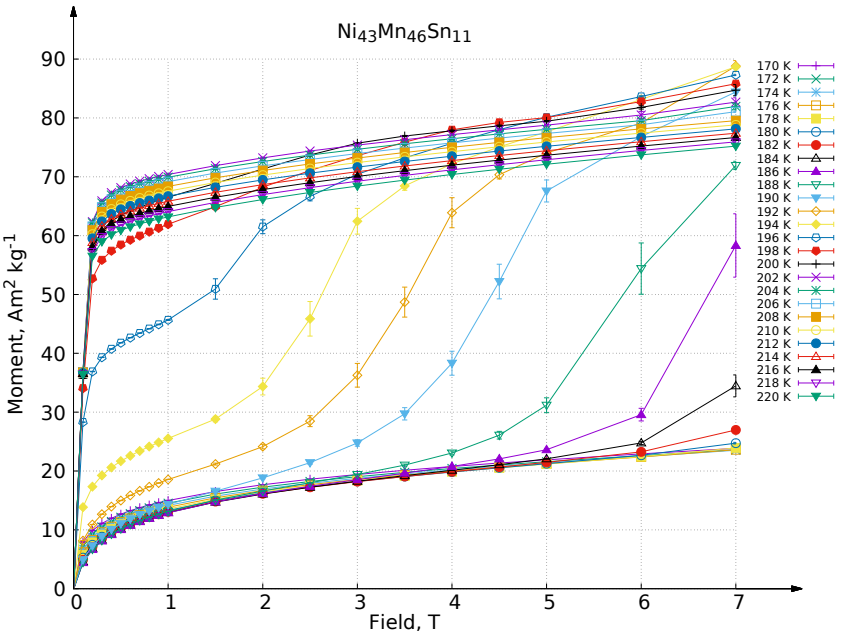

Figure 6.10: $Ni_{43}Mn_{46}Sn_{11}$ measurements during its phase transition. Measured between 170 and 220 K.

As a result a positive ΔS_M is expected during the phase transition and a negative one otherwise.

We look at 2 different temperature ranges for each sample. The first one depends on the sample itself. It covers the range of their phase transition and gives us the giant inverse MCE. For that we identified the start and end temperatures in section 6.1. Measurements begin 10 K below M_{end} and stop 10 K above A_{start} these temperatures. The 2nd measurement is near room temperature between 270 and 350 K. In all cases the temperature increases in steps of 2 K. This increase in temperature is done in zero field. The samples get inserted at low temperatures and then heated up at zero field to the start temperature of the procedure.

The field gets ramped up in many steps up until 7 T. Measurements are done at specific steps for this increasing field. In low fields we measure at intervals of 0.1 T up to 1 T. The magnetization changes a lot at this interval and so we need many points. From 1 to 5 T we measure in steps of 0.5 T. Then we also measure at 6 and 7 T. This gets repeated for all temperatures. The SQUID needs about 2 and a half minute to settle for the next temperature. We then also wait another minute after the temperature has settled.

We first look at $Ni_{43}Mn_{46}Sn_{11}$. Measurements for the giant inverse MCE are done between 170 and 220 K. The isothermal magnetization measurements are shown in

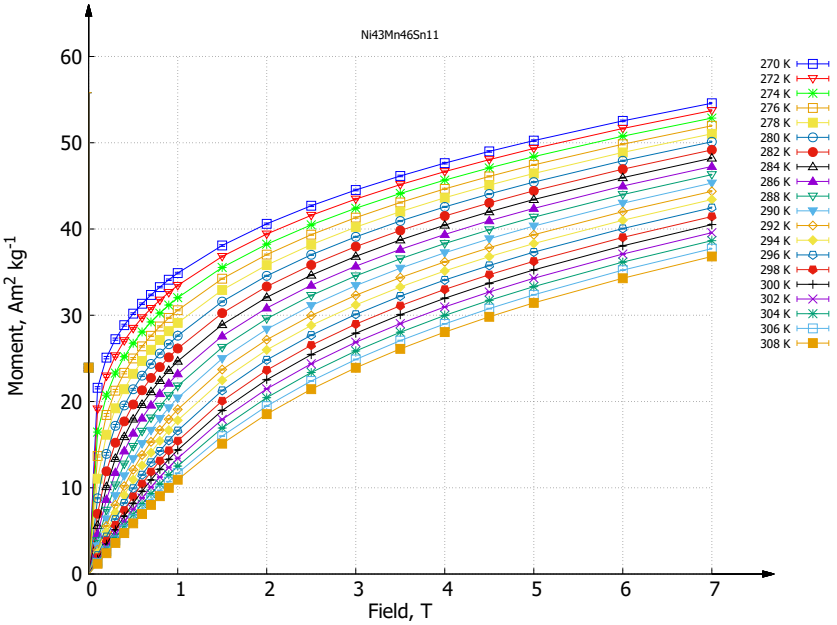

Figure 6.11: $Ni_{43}Mn_{46}Sn_{11}$ measurements between 272 and 308 K.

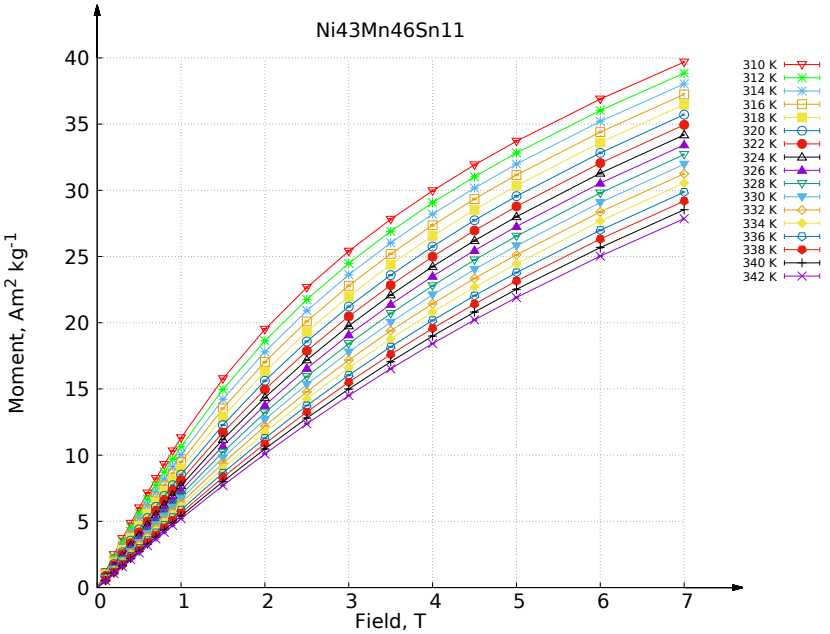

Figure 6.12: $Ni_{43}Mn_{46}Sn_{11}$ measurements between 310 and 342 K.

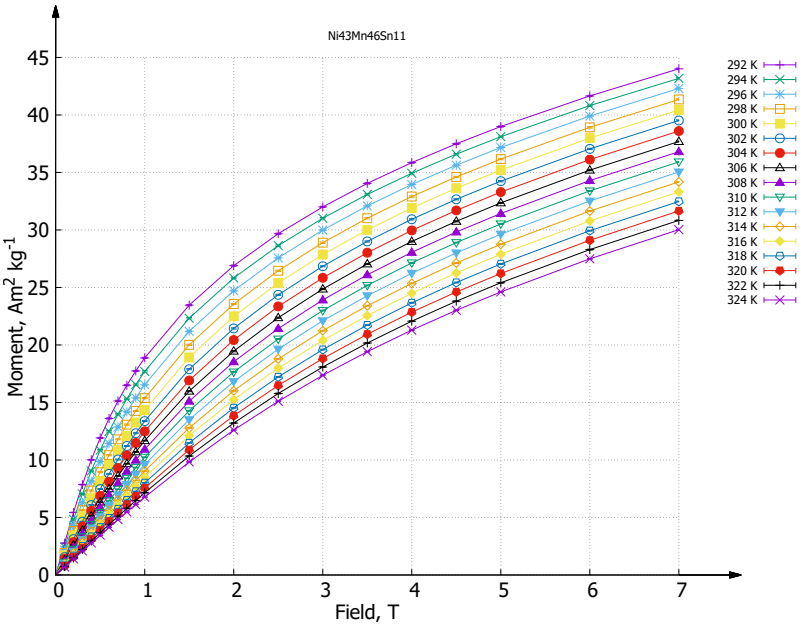

Figure 6.13: $Ni_{43}Mn_{46}Sn_{11}$ measurements between 292 and 324 K.

figure 6.10. At 7 T we see the magnetization increase at 180 K. It continues to increase until 202 K. For the magnetic entropy change this means an expected peak width of 22 K. This results in a magnetic entropy increase in this temperature range. In total we observe a magnetization increase of 60 Am^2kg^{-1} after the transition is over.

The strongest magnetization is seen for 194 K which is still during the phase transition. This is because the transition temperatures shift to lower temperatures for higher fields. The transition is already over for the fully charged 7 T field, but not in the weaker fields.

For the mentioned magnetization increase we compared the measurements before and after the transition. We also see big differences in magnetization for higher fields during the phase transition. At 186 K the magnetic moment increases from 30 to 68 Am^2kg^{-1} between 6 and 7 T. With rising temperatures this behaviour shifts to lower fields.

The measurements near room temperature had to be interrupted at 308 K. As discussed before in section 4.9, individual measurements can be used to calculate the magnetic entropy change. Comparing figure 6.11 and 6.12 shows that the magnetic moment has increased from 36 to 40 Am^2kg^{-1} between 308 and 310 K, after the sample was stored a few days at stable room temperature.

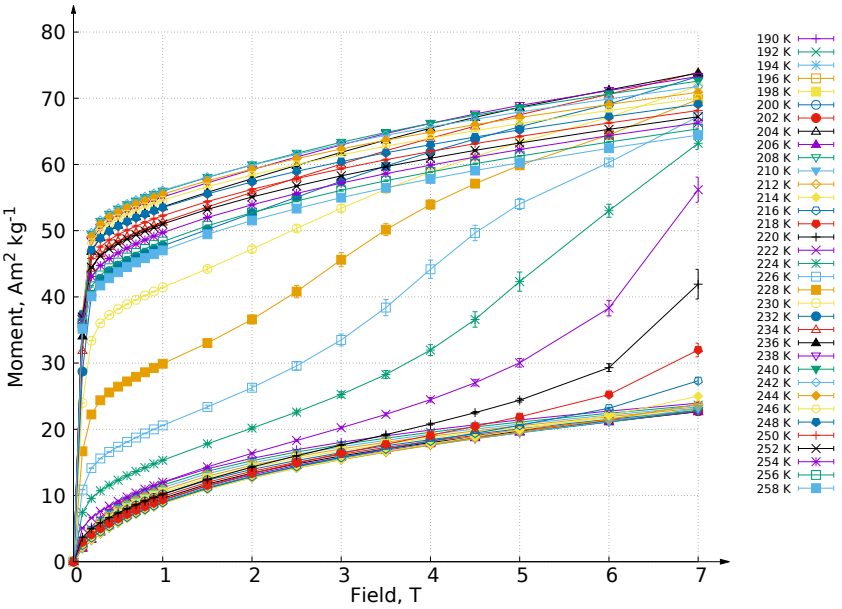

Figure 6.14: $Ni_{44}Mn_{45}Sn_{11}$ measurements between 190 and 258 K.

A third measurement also was performed between 292 and 324 K to ensure a correct result for the magnetic entropy change. The results for this measurement are shown in figure 6.13. In all 3 individual cases, the behaviour of the magnetic moment looks as expected and we have no crossing lines when plotting it. For the 3 sessions, the magnetic entropy has to be calculated individually. The comparison of the entropy for all 3 measurements was shown in figure 4.11 and the results are consistent with each other. We will discuss the results for the magnetic entropy change in section 6.3. Measurements for other samples were not interrupted and finished in one session.

$Ni_{44}Mn_{45}Sn_{11}$ was measured between in ranges from 190 to 258 to cover the phase transition. Figure 6.14 shows the isothermal magnetization in the temperature range of the phase transition. The magnetic moment starts to increase at 212 K until 240 K. An entropy peak width of 28 K is expected. This is a total increase of 50 Am^2kg^{-1}. Compared to the previous sample, only very strong fields of over 6 T show big effects during the phase transition. For 222 K the magnetic moment at 5 T is only 30 Am^2kg^{-1}, while for 7 T it increases to 56 Am^2kg^{-1}.

High temperature measurements of $Ni_{44}Mn_{45}Sn_{11}$ are conducted between 270 and 346 K. Their results are illustrated in figure 6.15. The signal keeps decreasing and the magnetization differences between temperatures are slowly decreasing.

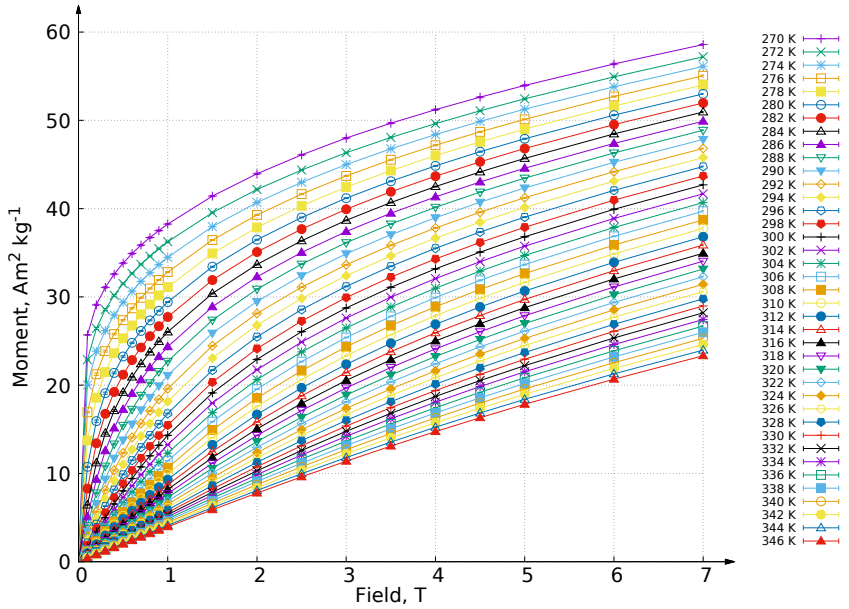

Figure 6.15: $Ni_{44}Mn_{45}Sn_{11}$ measurements between 270 and 346 K.

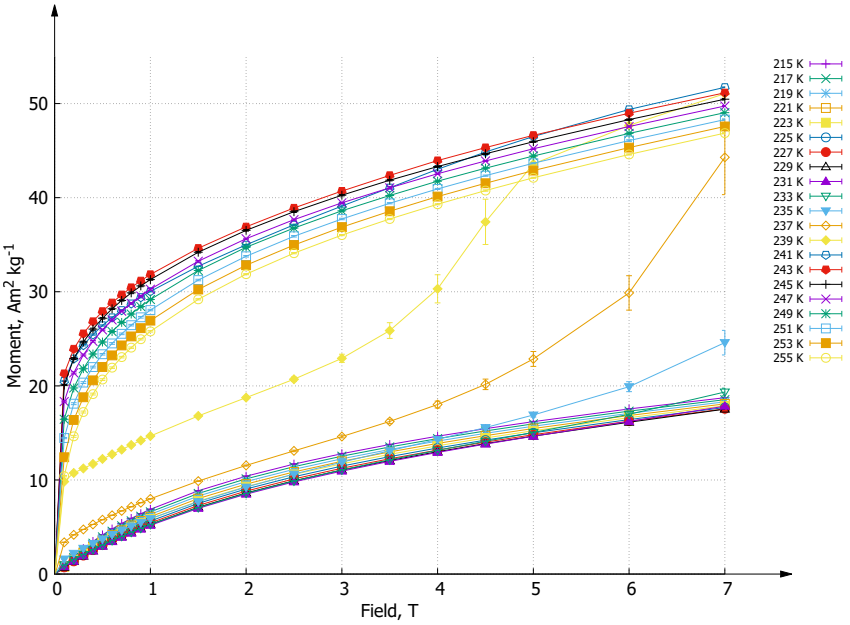

Figure 6.16: $Ni_{43}Mn_{46}Sn_9Ge_2$ measurements between 215 and 255 K.

This means that the magnetic entropy change will slowly approach zero. Except during the phase transition it will never become positive.

The phase transition of $Ni_{43}Mn_{46}Sn_9Ge_2$ was measured between 215 and 255 K (figure 6.16). We see the magnetization starting to increase at 233 K. The transition

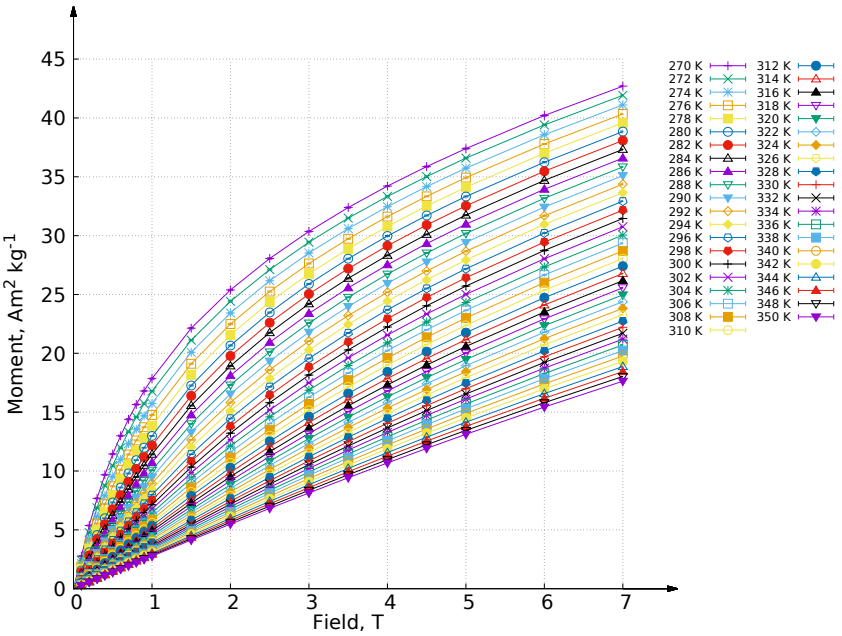

Figure 6.17: $Ni_{43}Mn_{46}Sn_9Ge_2$ measurements between 270 and 350 K.

complete at 243 K. This means an expected entropy peak width of 10 K. That is less than half those of the previous two samples. We also can expect a very tight ΔS_M peak. This is because only four measurements are actually during the phase transition and they show big differences in magnetization. Over the transition the magnetization increases from 18 to 52 Am^2kg^{-1}. The total change of magnetic moment between 233 and 243 K is 34 Am^2kg^{-1}.

High temperature measurements of $Ni_{43}Mn_{46}Sn_9Ge_2$ were implemented between 270 and 350 K and are shown in figure 6.17. The magnetization continues to decrease with rising temperatures and no atypical behaviour is observed. The magnetic moment at 270 K for 7 T is 43 Am^2kg^{-1} and decreases to 17 Am^2kg^{-1} at 350 K. Differences in magnetic moment get smaller for higher temperatures. A negative entropy change that approaches zero is expected.

Phase transition measurements for $Ni_{43}Mn_{46}Sn_9Si_2$ were conducted between 144 and 196 K and are shown in figure 6.18. The transition starts at 172 K and is over at 188 K. An entropy peak width of 16 K is expected. This is wider than for $Ni_{43}Mn_{46}Sn_9Ge_2$ but smaller than the other samples. Over the phase transition the magnetization increases from 25 $Am^2\,kg^{-1}$ at 170 K to 52 $Am^2\,kg^{-1}$ at 188 K. A smaller peak value than for $Ni_{43}Mn_{46}Sn_9Ge_2$ is expected because the plotted magnetization curves are more similar to each other during the phase transition.

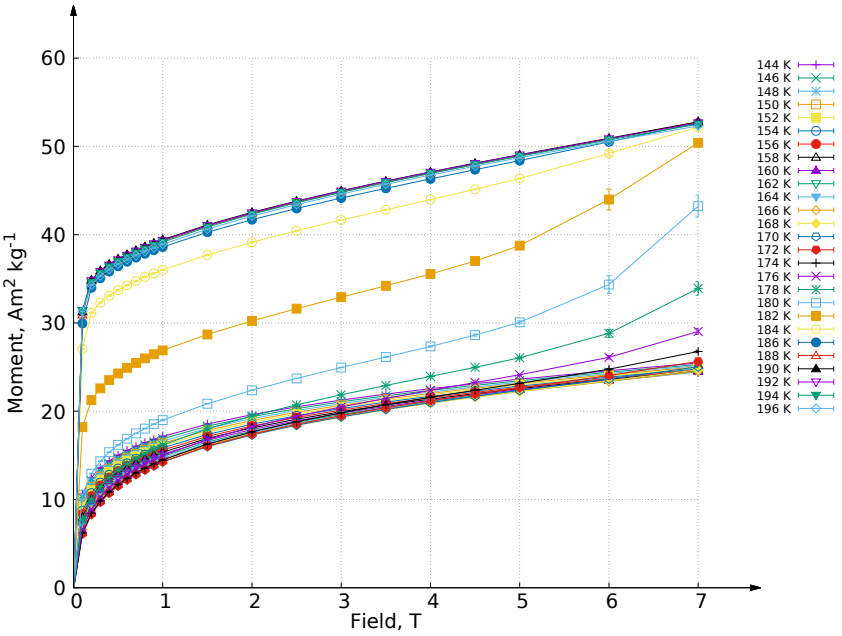

Figure 6.18: $Ni_{43}Mn_{46}Sn_9Si_2$ measurements between 144 and 196 K.

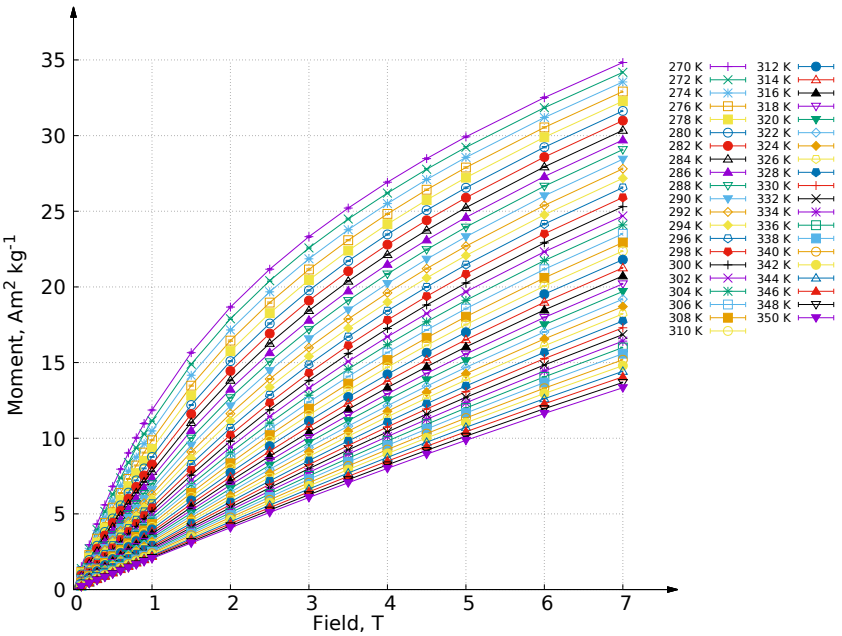

Figure 6.19: $Ni_{43}Mn_{46}Sn_9Si_2$ measurements between 270 and 350 K.

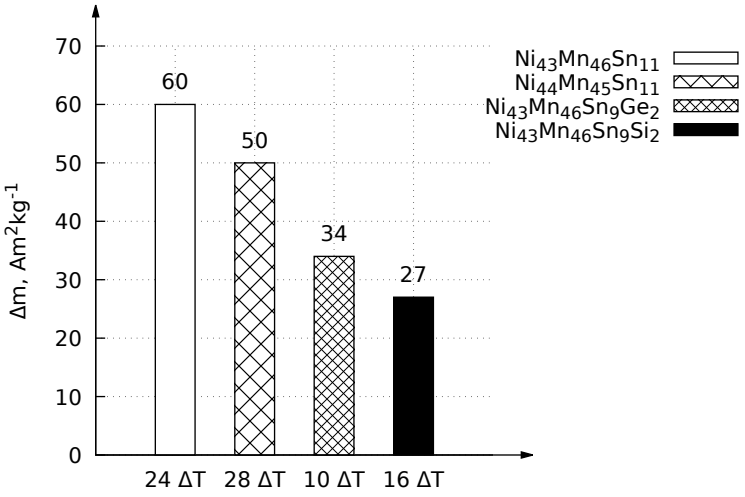

Figure 6.20: Magnetization changes over the phase transition. The ΔT at the bottom denotes the temperature range.

The magnetization after the phase transition remains similar for rising temperatures. This was also the case before the transition. Very small entropy changes outside of the transition are expected.

Figure 6.19 shows measurements for $Ni_{43}Mn_{46}Sn_9Si_2$ between 270 and 350 K. Differences in magnetic moment decrease with rising temperatures. The total decrease over 80 K is 22 $Am^2\,kg^{-1}$. As for the other samples a negative entropy change that approaches zero is expected.

The magnetization changes for all samples during their phase transition can be seen in figure 6.20. It shows that doping with Ge and Si leads to a decrease in transition width and smaller increase in magnetic moment. The transition width of $Ni_{44}Mn_{45}Sn_{11}$ is about 4 K wider than for $Ni_{43}Mn_{46}Sn_{11}$ while the change of magnetization has decreased.

6.2.2 Arrott Plots

Arrott plots of isothermal measurements, as introduced in section 5.3, were done to confirm the magnetic state of the samples.

Plots for $Ni_{43}Mn_{46}Sn_{11}$ (fig. 6.21) and $Ni_{44}Mn_{45}Sn_{11}$ (fig. 6.22) show a change in curvature, near their respective T_c from table 6.5. Those were obtained by different measurements, and the Arrott plots confirm them.

Thus, $Ni_{43}Mn_{46}Sn_{11}$ and $Ni_{44}Mn_{45}Sn_{11}$ undergo a transition from ferromagnetic to paramagnetic at 274 and 278 K respectively.

$Ni_{43}Mn_{46}Sn_9Ge_2$ (fig. 6.23) and $Ni_{43}Mn_{46}Sn_9Si_2$ (fig. 6.24) show only concave curvature. It can be concluded that those 2 samples are already in a paramagnetic state, at these temperatures.

Figure 6.25 shows an Arrott plot near T_c for $Ni_{43}Mn_{46}Sn_9Ge_2$ and shows curvature reversal between 251 and 253 K. This confirms T_c from table 6.5, meaning $Ni_{43}Mn_{46}Sn_9Ge_2$ undergoes the ferro- to paramagnetic transition shortly after its martensitic to austenitic phase transition.

For $Ni_{43}Mn_{46}Sn_9Si_2$ no M-H measurements near T_c were performed.

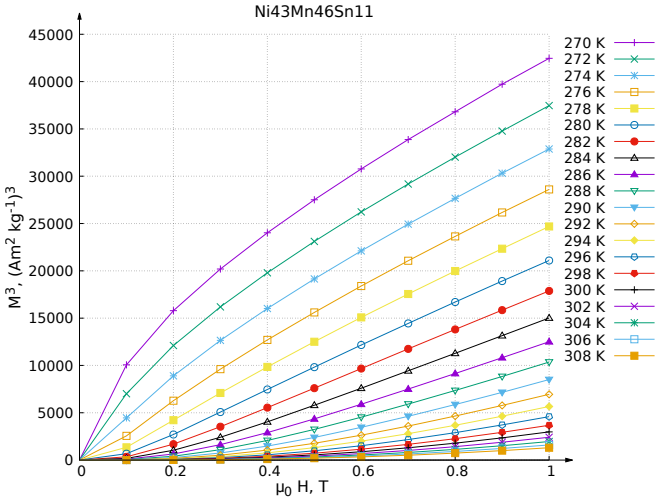

Figure 6.21: Arrot plot of $Ni_{43}Mn_{46}Sn_{11}$. Curvature changes between 274 and 276 K. T_c from table 6.5 was 274 K.

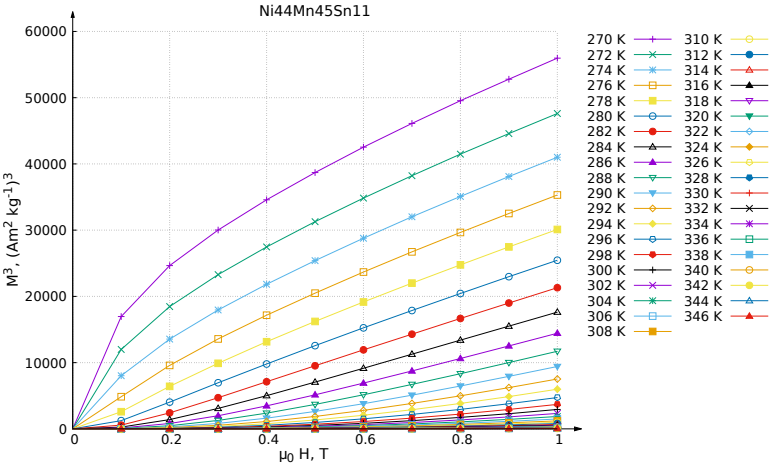

Figure 6.22: Arrot plot of $Ni_{44}Mn_{45}Sn_{11}$. Curvature changes between 276 and 278 K. T_c from table 6.5 was 278 K.

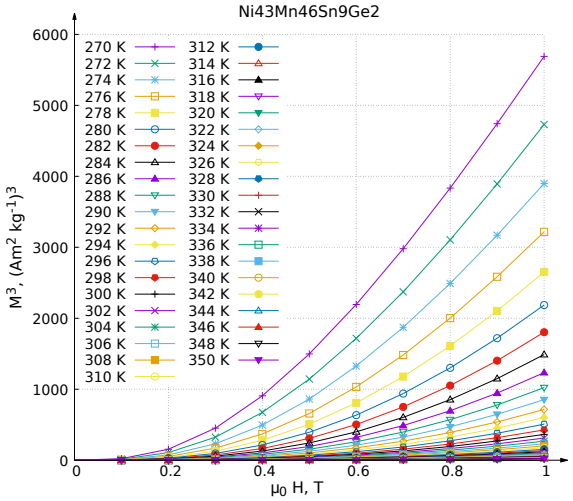

Figure 6.23: Arrott plot of $Ni_{43}Mn_{46}Sn_9Ge_2$. All isotherms show concave curvature. The sample is already above T_c.

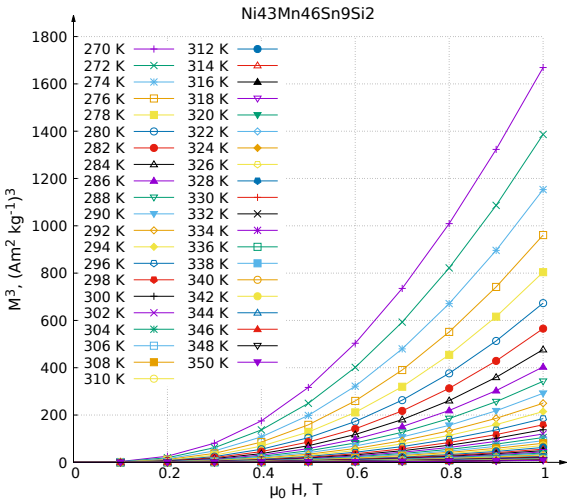

Figure 6.24: Arrott plot of $Ni_{43}Mn_{46}Sn_9Si_2$. All isotherms show concave curvature. The sample is already above T_c.

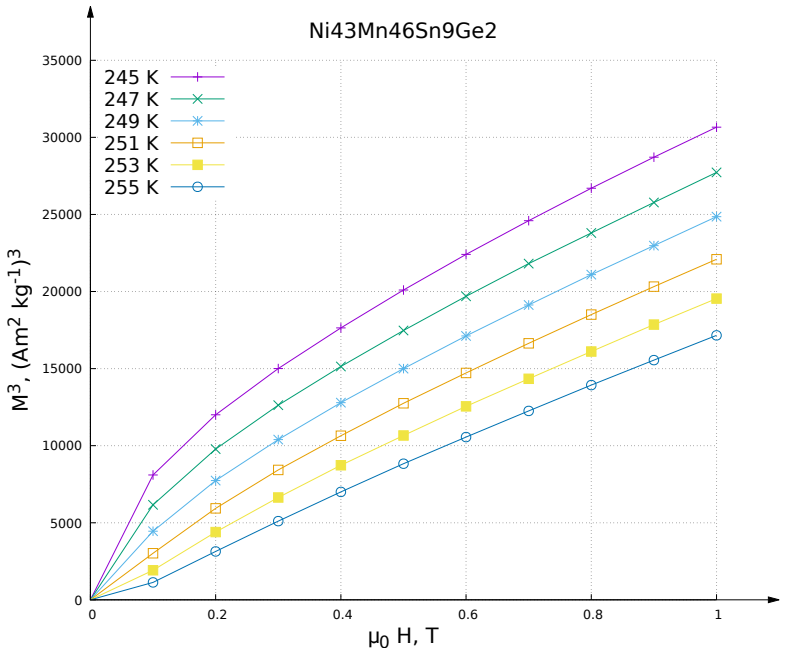

Figure 6.25: Arrott plot of $Ni_{43}Mn_{46}Sn_9Ge_2$ near $T_c = 251$ K. Curvature changes between 251 and 253 K.

6.2.3 Critical exponents

In section 5.4 we discussed how the critical exponent affects M-H measurements. By introducing the critical exponent and plotting M-$\mu_0 H/(T-T_c)^\gamma$, the isothermal measurements should converge in the paramagnetic state. Since $\vec{\mathbf{M}} \approx \chi \vec{\mathbf{H}}_{\text{vac.}}$ is only an approximation for weak magnetic fields, the scaling may fail for strong fields.

Most samples, apart from $Ni_{43}Mn_{46}Sn_9Si_2$, scale well for a critical exponent $\gamma = 1.2$.

For $Ni_{43}Mn_{46}Sn_9Si_2$ this comes close, but it converges better if you increase the exponent up to $\gamma = 1.35$.

In section 5.2 we mentioned that the ferro- to paramagnetic phase transition is usually not as sharp as it would be in theory. Because of this, the curves may not align instantly for T slightly above T_c.

For results, see figures 6.26 - 6.29. Critical exponents listed in table 6.6.

Table 6.6: Critical exponents γ for all samples.

Sample	T_c (K)	γ
$Ni_{43}Mn_{46}Sn_{11}$	274	1.2
$Ni_{44}Mn_{45}Sn_{11}$	278	1.2
$Ni_{43}Mn_{46}Sn_9Ge_2$	251	1.2
$Ni_{43}Mn_{46}Sn_9Si_2$	239	1.35

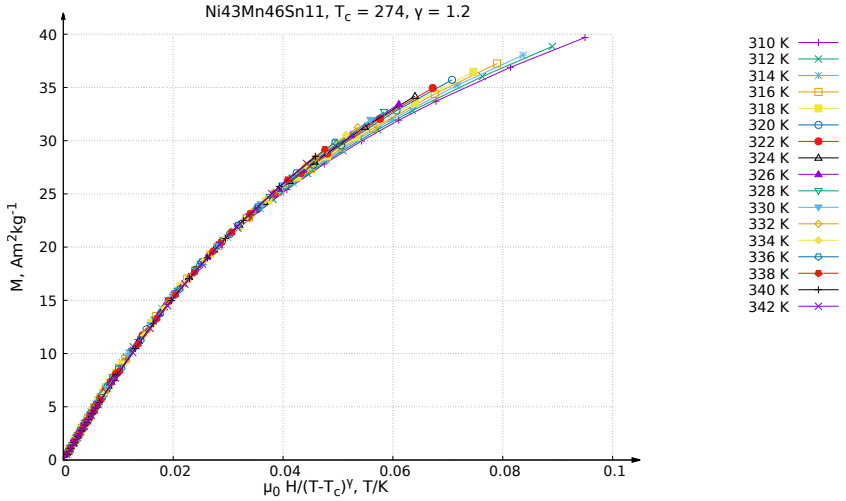

(a) Curves converge for $T > T_c$.

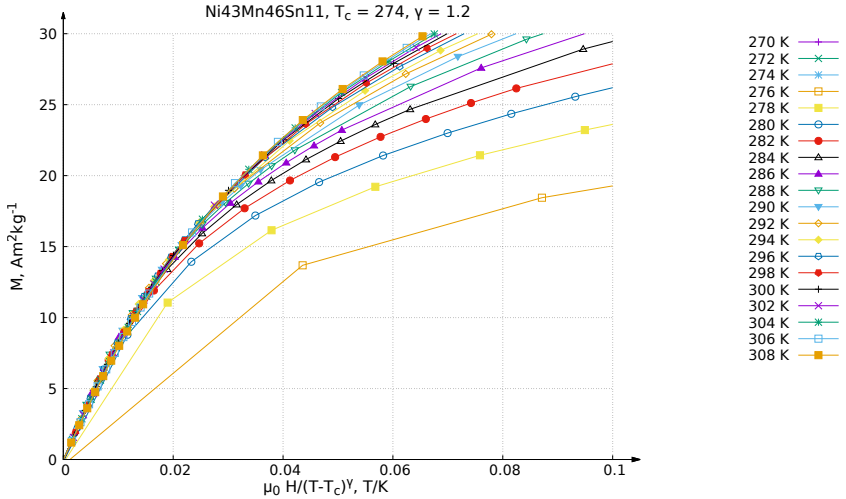

(b) Near $T_c = 274$ K. Curves are converging well above 278 K for weak fields.

Figure 6.26: Scaling of isothermal M-H measurements with critical exponent $\gamma = 1.2$ for $Ni_{43}Mn_{46}Sn_{11}$. Curves begin to converge for $T > T_c$ and weak fields.

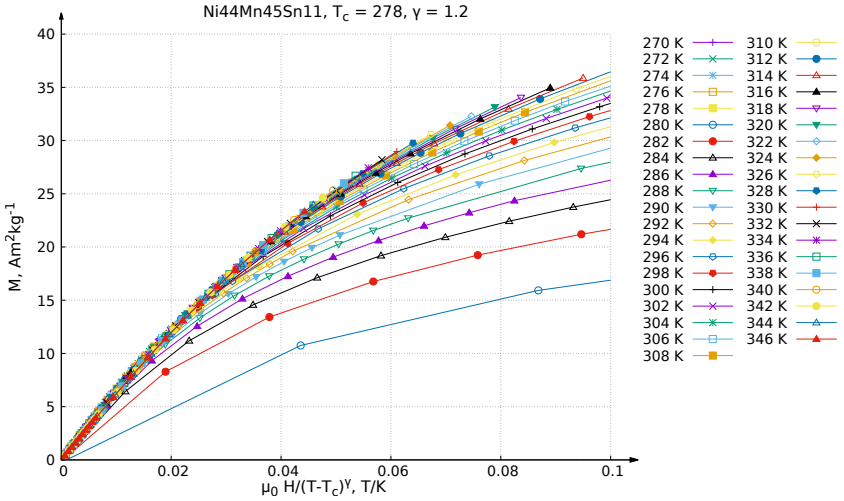

Figure 6.27: Scaling of isothermal M-H measurements with critical exponent $\gamma = 1.2$ for $Ni_{44}Mn_{45}Sn_{11}$. Curves begin to converge for weak fields above 282 K.

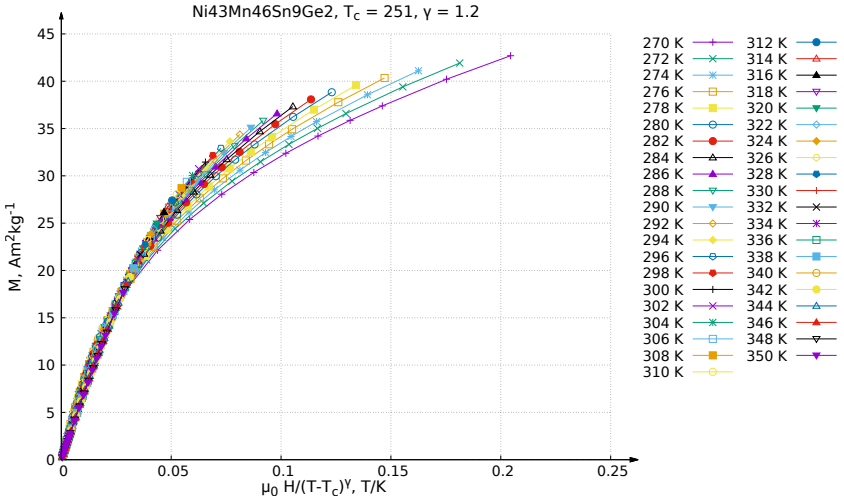

Figure 6.28: Scaling of isothermal M-H measurements with critical exponent $\gamma = 1.2$ for $Ni_{43}Mn_{46}Sn_9Ge_2$.

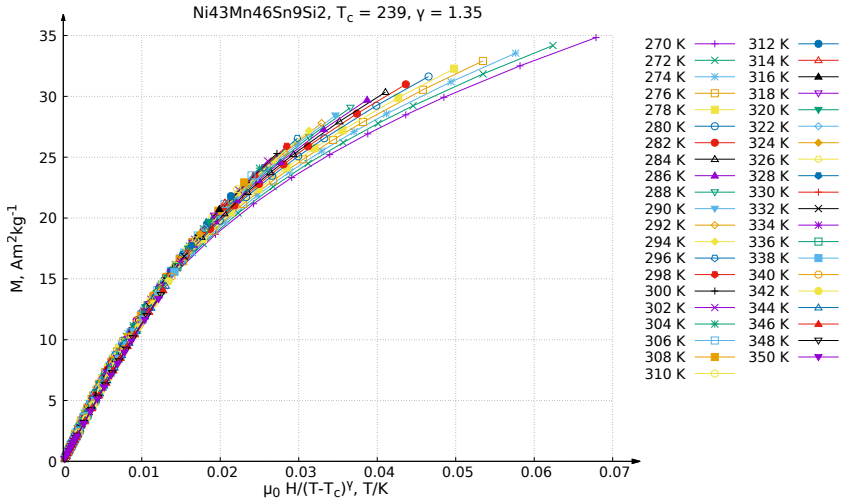

Figure 6.29: Scaling of isothermal M-H measurements with critical exponent $\gamma = 1.35$ for $Ni_{43}Mn_{46}Sn_9Si_2$.

6.3 Magnetic entropy change

Equation 4.18 is used to calculate the magnetic entropy change from the isothermal magnetization measurements. Results for phase transition are shown in figure 6.30a and for high temperatures in figure 6.30b.

The samples without Ge and Si doping show a wider transition range. Replacing 1 % Mn with Ni has decreased the peak value and shifted it to higher temperatures. Replacing 2 % Sn with 2 % Ge shifts it to even higher values but decreases the transition width. Doping with 2 % Si decreases transition width, peak value and transition temperature.

Transition temperatures and peak values are presented in table 6.7. The giant inverse MCEs of $Ni_{43}Mn_{46}Sn_{11}$ and $Ni_{43}Mn_{46}Sn_9Si_2$, as well as $Ni_{44}Mn_{45}Sn_{11}$ and $Ni_{43}Mn_{46}Sn_9Ge_2$ are overlapping at a tiny temperature range. Between those pairs is a gap of 15 K.

For high temperatures ΔS_M is always negative and slowly approaches zero for all samples. $Ni_{43}Mn_{46}Sn_{11}$ and $Ni_{44}Mn_{45}Sn_{11}$ show bigger magnetic entropy changes than the other two samples.

We see that doping with Ge has shifted the giant inverse MCE to higher temperatures. This was expected from the decreasing of the unit cell. For $Ni_{43}Mn_{46}Sn_9Si_2$ however, the peak has shifted to slightly lower temperatures. This was unexpected, because the atomic radius of Si is smaller than of Ge (table 4.3). Currently no explanation of this observation can be given.

In section 4.8 we already discussed the lattice parameters and Vcell for all samples. It turned out that Vcell for the Si doped sample was indeed smaller than for the Ge doped one. This means the size of Vcell alone cannot be the only remaining parameter, when e/a is already held constant. A possible candidate could be the ratio between Vcell in both phases (tab. 4.9) but this currently cannot be proven

Upon consultation with Dr. Marchenkov, a qualitative explanation was suggested, why the phase transition temperatures differ so much between $Ni_{43}Mn_{46}Sn_9Ge_2$ and $Ni_{43}Mn_{46}Sn_9Si_2$. The expected ion radii for Ge^{+2}, Sn^{+2} and Si^{-4} are 73, 93 and 271 pm respectively. Even though we only dope by 2%, we drastically change the chemical pressure. Chemical pressure comes from introducing new elements into the lattice, which change its Vcell. It decreases for Ge (smaller ion radius than Sn) and increases for Si (higher ion radius than Sn) doping.

Table 6.7: Magnetic entropy changes during the phase transition for all Samples.

	Temperature (K)			ΔS_M ($JK^{-1}kg^{-1}$)
Sample	T_{start}	T_{end}	Range	Peak value
$Ni_{43}Mn_{46}Sn_{11}$	180	200	20	45
$Ni_{44}Mn_{45}Sn_{11}$	210	238	28	30
$Ni_{43}Mn_{46}Sn_9Ge_2$	231	241	10	40
$Ni_{43}Mn_{46}Sn_9Si_2$	170	188	18	30

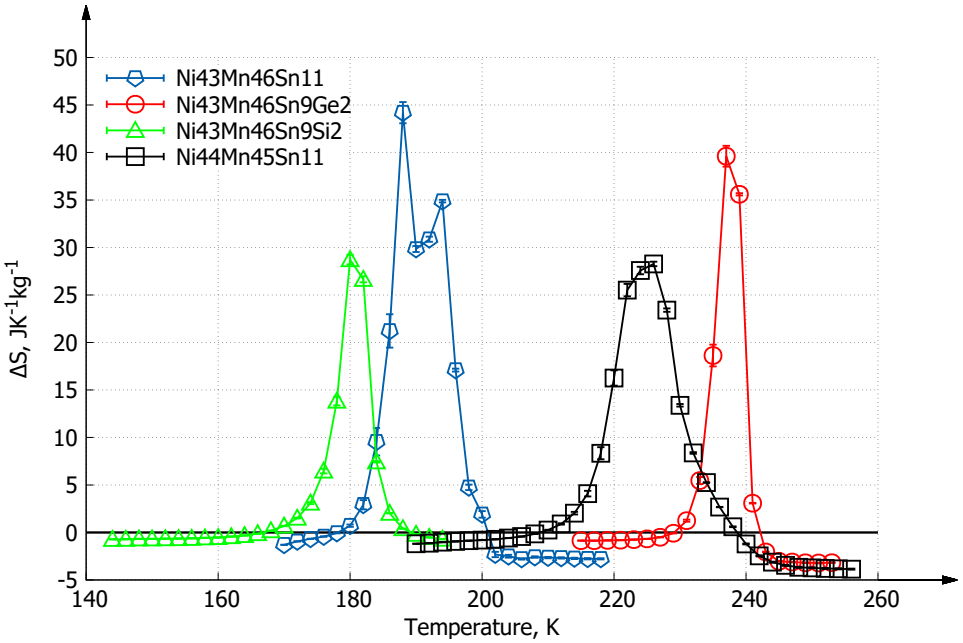

(a) At phase transition.

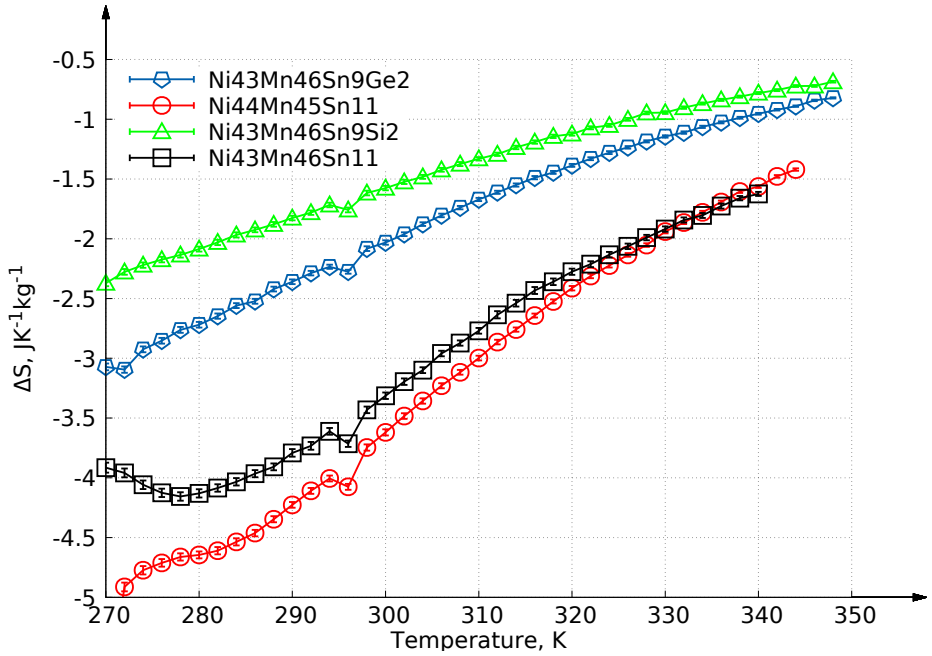

(b) At room temperatures.

Figure 6.30: Comparison of the magnetic entropy changes.

7 Results

Table 7.1: Refrigerant capacity over the phase transition region, the giant inverse magnetocaloric effect. Fields up to 7 T.

Sample	Temperature range (width)	RC	σ_{RC}
	K	J/kg	J/kg
$Ni_{43}Mn_{46}Sn_{11}$	180 - 200 (20)	393.23	3.76
$Ni_{44}Mn_{45}Sn_{11}$	214 - 238 (24)	333.01	1.93
$Ni_{43}Mn_{46}Sn_9Ge_2$	230 - 241 (11)	202.91	2.32
$Ni_{43}Mn_{46}Sn_9Si_2$	172 - 186 (14)	181.44	1.13

The magnetic entropy change from figure 6.30 can now be used to calculate the refrigerant capacity. As mentioned in section 4.6, this is the amount of energy that can be transferred between two temperatures. For the phase transition the magnetic entropy change is positive, resulting in positive refrigerant capacity. The RC of high temperature measurements will be negative.

The integral according to equation 4.32 is done over the peak width for the phase transition. For high temperatures we use the whole range measurement. The entropy change for the giant inverse MCE is an order of magnitude bigger than at high temperatures, but only over a short temperature range.

We don't have measurements for the heat capacity. However a publication[15] shows measurements for $Ni_{43}Mn_{46}Sn_{11}$ in fields of 0 and 5 T between 150 and 250 K. Apart from the phase transition region, it shows a almost linear pattern. For 150 K it's 300 $JK^{-1}kg^{-1}$ and increases to 400 for 250 K. During the phase transition it increases to 1050 $JK^{-1}kg^{-1}$. This ensures an adiabatic temperature decrease during the giant inverse MCE.

Refrigerant capacities over phase transition for all samples are shown in table 7.1 and figure 7.1. The table also lists the temperature range where the RC was eval-

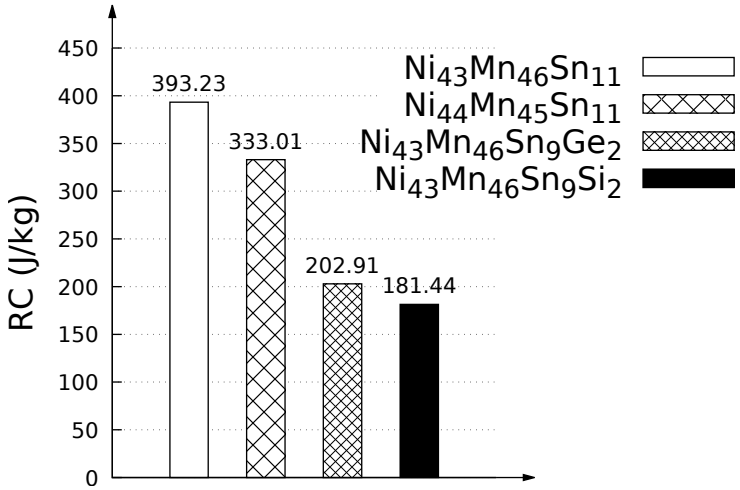

Figure 7.1: Comparison of refrigerant capacities over the phase transition with fields up to 7 T.

uated. We see that $Ni_{43}Mn_{46}Sn_{11}$ has the biggest energy flow over the transition range. $Ni_{44}Mn_{45}Sn_{11}$ slightly increases the transition range but its RC is smaller. Doping has shifted the phase transition temperatures but also decreased phase transition range and refrigerant capacity.

High temperature results are displayed in table 7.2 and figure 7.2. Since there was no phase transition, we evaluated over the whole measurement range. As shown in the brackets in table 7.2 this varies between 70 and 78 K. This is 3 to 4 times as wide as calculations for the phase transition.

$Ni_{44}Mn_{45}Sn_{11}$ shows the biggest RC out of all samples. This was expected after we saw their magnetic entropy changes in figure 6.30b. $Ni_{43}Mn_{46}Sn_{11}$ is similar to it, while the other two show a smaller RC.

In the end we notice that doping with Ge was effective in raising the phase transition temperature to warmer regions. However we lost half of its refrigerant capacity in the process, compared to the one of $Ni_{43}Mn_{46}Sn_{11}$.

Doping with Si shifted the phase transition slightly to lower temperature regions while also losing half of the refrigerant capacity.

Replacing one Mn with a Ni atom shifted the phase transition to higher temperatures and shows only a slight decrease in refrigerant capacity.

Propagation of error proofed to be insignificant, as can be seen in table 7.2 and figure 7.2.

Table 7.2: Refrigerant capacity over high temperature intervals. Covered temperature differences are between 70 and 78 K with fields up to 7 T.

Sample	Temperature range (width)	RC	σ_{RC}
	K	J/kg	J/kg
$Ni_{43}Mn_{46}Sn_{11}$	270 - 340 (70)	-210.39	0.23
$Ni_{44}Mn_{45}Sn_{11}$	270 - 344 (74)	-238.33	0.20
$Ni_{43}Mn_{46}Sn_9Ge_2$	270 - 348 (78)	-140.46	0.14
$Ni_{43}Mn_{46}Sn_9Si_2$	270 - 346 (76)	-108.67	0.14

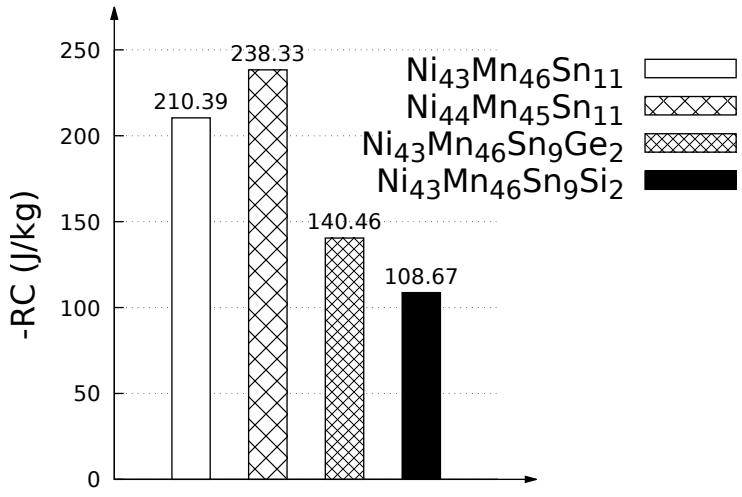

Figure 7.2: Comparison of refrigerant capacities for high temperatures. Temperature intervals of 70 to 78 K with fields up to 7 T.

8 Conclusion

Doping $Ni_{43}Mn_{46}Sn_{11}$ has a significant influence on the giant inverse MCE. Exchanging only 1 or 2 at% of atoms managed to shift the phase transition temperatures on wide temperature ranges.

All samples show a giant inverse MCE, which is strongest for the initial alloy $Ni_{43}Mn_{46}Sn_{11}$. Increasing the Ni amount by only 1%, while decreasing Mn has shifted the phase transition to higher temperatures. This was expected because e/a got increased.

It was expected that a decrease in Vcell would shift the transition to warmer regions, but this turned out to be wrong. Section 4.8 showed that Vcell decreased continuously for doping with Ge and Si, as their atomic radii got smaller. While it clearly worked for $Ni_{43}Mn_{46}Sn_9Ge_2$, for $Ni_{43}Mn_{46}Sn_9Si_2$ the phase transition dropped to lower temperatures than $Ni_{43}Mn_{46}Sn_{11}$. Upon consulting with Dr. Marchenkov it was mentioned that maybe the ratio of Vcell between both phases could play a role, but impossible to say for sure without further analysis of new samples.

However, the big differences in expected ionic radii (sec. 6.3) at least provide an idea why doping by only 2% can cause such a big shift in transition temperatures, due to chemical pressure. If the expected ion radii of Si, Ge and Sn proof to be correct, it could also be a clue why Si and Ge doping is shifting the transition temperatures in different directions. Si would occupy more space in Vcell than Sn, while Ge would occupy less.

An article about NiMnIn alloys has shown that the actual at% can differ from their chemical formula.[20] Dr. Marchenkovs group will take a closer look at the actual e/a in the alloys of this thesis, as well as the actual position of the ions with electron microscopy and how it affects the phase transition temperatures.

Doping $Ni_{43}Mn_{46}Sn_{11}$ has resulted in a decrease of refrigerant capacity over phase transition for all other 3 samples. At high temperatures the Si and Ge doped samples show a smaller entropy change than the other two samples. Compared to the phase transition region however, this ΔS_M is one order of magnitude smaller.

Appreciations

Here I want to devote a few words of special thanks to the people that made this thesis possible.

Dr. Franz Sauerzopf from the lab for low temperature physics of the institute for nuclear physics of vienna (Atominstitut), for supervising and giving the opportunity for this thesis.

All members of the before mentioned lab for instruction and help to work with the Superconducting Quantum Interference Device.

Dr. Vyacheslav Viktorovich Marchenkov and his group in Urals Branch of the Russian Academy of Sciences, for providing the samples from his field of work.

And last but not least to my whole family for their support.

List of Figures

List of Tables

Bibliography

[1] R.L. Wang, J.B. Yan, L.S. Xu, V.V. Marchenkov, S.S. Chen, S.L. Tang, and C.P. Yang. "Effect of Al doping on the martensitic transition and magnetic entropy change in Ni–Mn–Sn alloys". In: *Solid State Communications* (Apr. 27, 2011). URL: www.elsevier.com/locate/ssc.

[2] Wikipedia. *Magnetic refrigeration*. Apr. 20, 2017. URL: https://en.wikipedia.org/wiki/Magnetic_refrigeration.

[3] Quantum Design. *MPMS XL - hardware & software reference manuals*. SQUID manual. 2004.

[4] J. Clarke and A. Braginski. *The SQUID Handbook: Fundamentals and Technology of SQUIDs and SQUID Systems, Volume 1*. WILEY-VCH Verlag GmbH & Co. KGaA Weinheim, 2004.

[5] S. Bühler-Paschen, H. Michor, and M. Reissner. *Festkörperphysik I*. Script of Festkörperphysik I at TU Wien. 2018.

[6] Massachusetts Institute of Technology. *Lecture 11: Basic Josephson Junctions*. Apr. 20, 2017. URL: web.mit.edu/6.763/www/FT03/Lectures/Lecture11.pdf.

[7] Walther–Meißner–Institut. *Josephson Effects in Superconductors*. Technische Universität München. 2017. URL: https://www.wmi.badw.de/teaching/Praktika/files/userguide-16.en.pdf.

[8] R. L. Fagaly. "Superconducting quantum interference device instruments and applications". In: *Review of Scientific Instruments* 77.10 (2006), p. 101101. DOI: 10.1063/1.2354545. eprint: https://doi.org/10.1063/1.2354545. URL: https://doi.org/10.1063/1.2354545.

[9] A. Garachtchenko, A. Matlashov, R. H. Kraus, and R. Cantor. "Baseline distance optimization for SQUID gradiometers". In: *IEEE Transactions on Applied Superconductivity* 9.2 (June 1999), pp. 3676–3679. ISSN: 1051-8223. DOI: 10.1109/77.783826.

[10] Quantum Design. *Fundamentals of magnetism and magnetic measurements*. 2018. URL: https://www.qdusa.com/sitedocs/appNotes/mpms/FundPrimer.pdf.

[11] X. Moya, S. Kar-Narayan, and N. D. Mathur. "Caloric materials near ferroic phase transitions". In: *Nature Materials* 13 (Apr. 2014). Review Article, p. 439. URL: http://dx.doi.org/10.1038/nmat3951.

[12] V. Vodyanoy and Y. Mnyukh. *The physical nature of "giant" magnetocaloric and electrocaloric effects*. June 3, 2013. arXiv: 1012.0967 [cond-mat.mtrl-sci]. URL: https://arxiv.org/abs/1012.0967.

[13] V. Franco. *Determination of the Magnetic Entropy Change from Magnetic Measurements*. Apr. 20, 2017. URL: http://www.lakeshore.com/Documents/MagneticEntropyChangefromMagneticMeasurements.pdf.

[14] T. Krenke, E. Duman, M. Acet, E. F. Wassermann, X. Moya, L. Mañosa, and A. Planes. "Inverse magnetocaloric effect in ferromagnetic Ni-Mn-Sn alloys". In: *Nature Materials* 4 (June 2005), pp. 450–454. DOI: 10.1038/nmat1395. arXiv: cond-mat/0505652.

[15] Y. Zhang, Q. Zheng, W. Xia, J. Zhang, J. Du, and A. Yan. "Enhanced large magnetic entropy change and adiabatic temperature change of Ni43Mn46Sn11 alloys by a rapid solidification method". In: *Scripta Materialia* 104 (2015), pp. 41–44. ISSN: 1359-6462. DOI: https://doi.org/10.1016/j.scriptamat.2015.04.004. URL: http://www.sciencedirect.com/science/article/pii/S1359646215001293.

[16] F. Casanova i Fernàndez. "Magnetocaloric Effect In Gd5(SixGe1-x)4 Alloys". https://www.tdx.cat/bitstream/handle/10803/1789/1.CHAPTER_1.pdf. Universitat de Barcelona. Departament de Física Fonamental, Mar. 9, 2004. Chap. 1. URL: http://www.tdx.cat/handle/10803/1789#.

[17] G. Kahl. *Statistische Physik II*. German. Slides of statistical physics II at TU Wien. 2019. URL: http://smt.tuwien.ac.at/extra/teaching/statphys2/kapitel_II_1.pdf.

[18] V. V. Khovaylo, K. P. Skokov, Y. S. Koshkid'ko, V. V. Koledov, V. G. Shavrov, V. D. Buchelnikov, S. V. Taskaev, H. Miki, T. Takagi, and A. N. Vasiliev. "Adiabatic temperature change at first-order magnetic phase transitions: $Ni_{2.19}Mn_{0.81}Ga$ as a case study". In: *Phys. Rev. B* 78 (6 Aug. 2008), p. 060403. DOI: 10.1103/PhysRevB.78.060403. URL: https://link.aps.org/doi/10.1103/PhysRevB.78.060403.

[19] K. A. GschneidnerJr, V. K. Pecharsky, and A. O. Tsokol. "Recent developments in magnetocaloric materials". In: *Reports on Progress in Physics* 68.6 (2005), p. 1479. URL: http://stacks.iop.org/0034-4885/68/i=6/a=R04.

[20] L. González-Legarreta, D. González-Alonso, W. Rosa, R. Caballero-Flores, J. Suñol, J. González, and B. Hernando. "Magnetostructural phase transition in off-stoichiometric Ni–Mn–In Heusler alloy ribbons with low In content". In: *Journal of Magnetism and Magnetic Materials* 383 (2015). Selected papers from the sixth Moscow International Symposium on Magnetism (MISM-2014), pp. 190–195. ISSN: 0304-8853. DOI: https://doi.org/10.1016/j.jmmm.2014.10.152. URL: http://www.sciencedirect.com/science/article/pii/S0304885314010750.

[21] C. E. Mortimer and U. Müller. *Chemie : das Basiswissen der Chemie. Chemistry (dt.)* German. 9., überarb. Aufl. Stuttgart: Stuttgart : Thieme, 2007.

[22] Wikipedia. *List of space groups*. Jan. 3, 2019. URL: https://en.wikipedia.org/wiki/List_of_space_groups.

[23] Dr. Nikos Pinotsis. *List of space groups*. 2019. URL: https://homepage.univie.ac.at/nikos.pinotsis/spacegroup.html.

[24] M. Leitner. *Index by Space Group*. 2019. URL: https://homepage.univie.ac.at/michael.leitner/lattice/spcgrp/index.html.

[25] K. Mandel. "Synthesis and Characterisation of Superparamagnetic Nanocomposite Particles for Water Purification and Resources Recovery". PhD thesis. Julius-Maximilians-Universität Würzburg - Fraunhofer-Institut für Silicatforschung ISC, 2013. URL: https://opus.bibliothek.uni-wuerzburg.de/opus4-wuerzburg/frontdoor/deliver/index/docId/6765/file/Karl_Mandel_Dissertation.pdf.

[26] I. Bruvera, P. Mendoza Zélis, M. Calatayud, G. Goya, and F. H. Sánchez. "Determination of the blocking temperature of magnetic nanoparticles: The good, the bad and the ugly". In: 118 (Aug. 2015). arXiv: 1508.04413. URL: https://www.researchgate.net/publication/281115016.

[27] R. Mathieu. "Magnetism of manganites, semiconductors and spin glasses". PhD thesis. Department of Materials Science, Uppsala University, 2002. URL: http://www.diva-portal.org/smash/get/diva2:161746/FULLTEXT01.pdf.

[28] R. B. Goldfarb and C. E. Patton. "Superparamagnetism and Spin-Glass Freezing in Nickel-Manganese Alloys". In: *Physical Review B (Condensed Matter and Materials Physics)* (1981). URL: https://www.nist.gov/publications/superparamagnetism-and-spin-glass-freezing-nickel-manganese-alloys.

[29] J. E. Ortmann, J. Y. Liu, J. Hu, M. Zhu, J. Peng, M. Matsuda, X. Ke, and Z. Q. Mao. "Competition Between Antiferromagnetism and Ferromagnetism in Sr2RuO4 Probed by Mn and Co Doping". In: *Scientific Reports* (2013). URL: http://dx.doi.org/10.1038/srep02950.

[30] N. Dan, N. Duc, N. Yen, P. Thanh, L. Bau, N. An, D. Anh, N. Bang, N. Mai, P. Anh, T. Thanh, T. Phan, and S. Yu. "Magnetic properties and magnetocaloric effect in Ni–Mn–Sn alloys". In: *Journal of Magnetism and Magnetic Materials* 374 (2015), pp. 372–375. ISSN: 0304-8853. DOI: https://doi.org/10.1016/j.jmmm.2014.08.061. URL: http://www.sciencedirect.com/science/article/pii/S0304885314007604.

[31] W. Demtröder. *Experimentalphysik 2 - Elektrizität und Optik*. German. 3rd ed. 2004.

[32] K. Fabian, V. P. Shcherbakov, and S. A. McEnroe. "Measuring the Curie temperature". In: *Geochemistry, Geophysics, Geosystems* 14.4 (2013), pp. 947–961. DOI: 10.1029/2012GC004440. eprint: https://agupubs.onlinelibrary.wiley.com/doi/pdf/10.1029/2012GC004440. URL: https://agupubs.onlinelibrary.wiley.com/doi/abs/10.1029/2012GC004440.

[33] F. Bensch. "Der magnetische Phasenübergang und das Einsetzen des Ferromagnetismus bei dünnen Eisenschichten auf Galliumarsenid". T_c uncertainity mentioned on page 77. PhD thesis. Universität Regensburg, 2001. URL: https://core.ac.uk/download/pdf/11539519.pdf.

[34] M. A. Zaidi, J. Dhahri, I. Zeydi, T. Alharbia, and H. Belmabrouka. "Large magnetocaloric effect and critical behavior in $La_{0.7}Ba_{0.2}Ca_{0.1}Mn_{1-x}Al_xO_3$". In: *RSC Advances* (69 2017). Incorrect labels in figur 4. See table 3 and figure 3 for correct values. URL: https://pubs.rsc.org/en/Content/ArticleLanding/2017/RA/C7RA08162F#!divAbstract.

[35] A. Arrott. "Criterion for Ferromagnetism from Observations of Magnetic Isotherms". In: *Phys. Rev.* 108 (6 Dec. 1957), pp. 1394–1396. DOI: 10.1103/PhysRev.108.1394. URL: https://link.aps.org/doi/10.1103/PhysRev.108.1394.

[36] R. Hadimani, Y. Melikhov, J. Evan Snyder, and D. Jiles. "Determination of Curie temperature by Arrott plot technique in Gd5(SixGe1-x)4 for x>0.575". In: *Journal of Magnetism and Magnetic Materials* 320 (Oct. 2008). DOI: 10.1016/j.jmmm.2008.04.035.

[37] G. Kahl. *Statistische Physik II*. German. Slides of statistical physics II at TU Wien. 2019. URL: http://smt.tuwien.ac.at/extra/teaching/statphys2/kapitel_II_3.pdf.

[38] V. Basso. *Basics of the magnetocaloric effect*. Apr. 7, 2013. arXiv: 1702.08347 [cond-mat.mtrl-sci]. URL: https://arxiv.org/abs/1702.08347.

[39] CHEMIE.DE Information Service GmbH. *SQUID*. Apr. 20, 2017. URL: http://www.chemie.de/lexikon/SQUID.html.

[40] H. H. Wills Physics Laboratory. *SQUIDs: A Technical Report - Part 3: SQUIDs*. Apr. 20, 2017. URL: http://rich.phekda.org/squid/technical/part3.html.

[41] K. L. Barbalace. *Enviromental Chemistry*. Oct. 1, 2018. URL: https://environmentalchemistry.com/.

[42] K. Yamaguchi, S. Ishida, and S. Asano. "Valence Electron Concentration and Phase Transformations of Shape Memory Alloys Ni–Mn–Ga–X". In: *Materials Transactions, Vol. 44, No. 1* (2013). URL: https://www.jim.or.jp/journal/e/pdf3/44/01/204.pdf.

[43] E. Bauer, C. Eisenmenger-Sittner, and J. Fidler. *Materialwissenschaften*. Script of Materialwissenschaften at TU Wien. 2010.